

Solar Energy Stored as Hydrogen: Controlling Inexpensive Oxide-based Nanostructures for Efficient Water Splitting

THÈSE N° 5478 (2012)

PRÉSENTÉE LE 28 SEPTEMBRE 2012

À LA FACULTÉ DES SCIENCES DE BASE

LABORATOIRE DE PHOTONIQUE ET INTERFACES

PROGRAMME DOCTORAL EN CHIMIE ET GÉNIE CHIMIQUE

ÉCOLE POLYTECHNIQUE FÉDÉRALE DE LAUSANNE

POUR L'OBTENTION DU GRADE DE DOCTEUR ÈS SCIENCES

PAR

Jérémie Minh-Châu BRILLET

acceptée sur proposition du jury:

Dr M. Drabbels, président du jury
Prof. M. Graetzel, Prof. K. Sivula, directeurs de thèse
Prof. J. Augustynski, rapporteur
Prof. H. Hofmann, rapporteur
Prof. A. Mendes, rapporteur



ÉCOLE POLYTECHNIQUE
FÉDÉRALE DE LAUSANNE

Suisse
2012

*To my family, in particular Appoline, Eve,
Théotime, Anouk and those to come.*

*Their generation will not have the benefit of two
billion years' accumulated energy reserves*

Abstract

The tandem photoelectrochemical (PEC) cell based on oxide semiconductors for water splitting offers a potentially inexpensive route for solar hydrogen generation. At the heart of the device, a nanostructured photoanode for water oxidation is connected in series with one or two dye-sensitized solar cells (DSCs) that provide an extra bias to photogenerated electrons in order to perform water reduction at the platinum cathode.

In Part A of this thesis, after reviewing the different technologies available for solar hydrogen production, I focus on different possible architectures for photoanode / DSC tandem cells enabled by the most recent advances in the field. First, the development of all organic squaraine dyes having a narrow absorption bandwidth extending into the near infrared region and a broad transparent window in the visible region of the spectrum have allowed the design of a new photoanode / DSC / DSC tandem architecture. The "Back DSC" tandem cell, where two DSCs placed side-by-side exploit the photons transmitted by a single photoanode is the conventional architecture. In this thesis, I demonstrate the inverted "Front DSC" architecture, which allows the use of non-transparent lower cost metallic substrate for the photoanode, as well as the "tri-level" tandem cell where a panchromatic "black" dye-based DSC exploits the energy transmitted by the photoanode and the squaraine dye-based DSC. Opto-electronic studies on each of these three architecture are performed and the respective solar-to-hydrogen conversion (STH) efficiencies of 1.16 %STH, 0.76 %STH and 1.36 %STH are assessed. Finally, I leverage recent findings in the field of high voltage DSCs to demonstrate for the first time a tandem cell using only one photovoltaic cell to perform complete water splitting at efficiencies as high as 3.10 % STH. Such a result represents a ten-fold improvement over previous demonstrations with this class of device. This work describes a breakthrough in the inexpensive solar-to-chemical conversion using improved photon management in a dual-absorber tandem cell and undoubtedly constitutes a benchmark for solar fuel production by solution processable oxide-based devices.

In Part B, I focus on the photoanode for the oxygen evolution reaction. Hematite ($\alpha\text{-Fe}_2\text{O}_3$) is a great candidate material for this application due to its

availability, low cost, non-toxicity and appropriate band gap allowing extensive absorption in the visible part of the spectrum. However, it suffers severe drawbacks, among which are poor majority carrier conductivity and a short diffusion length of minority charge carrier with regard to photon penetration depth. This circumstance causes most photogenerated charges to have a low probability of reaching the semiconductor / liquid junction and thus to participate in the water oxidation reaction. This feature implies the use of hematite morphologies having feature size in the range of 10-20 nm. A solution-based colloidal approach offers a simple and easily scalable method to obtain nanostructured hematite. However, this type of nanostructure needs to be exposed to an annealing step at 800 °C to become photoactive. This has been attributed to the diffusion of dopants from the substrate. In addition, this annealing step sinters the 10 nm particles colloid into a feature size approaching 100 nm. Here, I first show the effect of intentionally doping this material on the sintering and photoactivity. I then demonstrate a method that allows for the first time to apply high temperature annealing steps while controlling the feature size of the nanoparticles. Such an approach can be applied to any kind of nanostructure. This latter strategy coupled to further passivation of surface states allowed an improvement of the net photoactivity of this type of photoanode by a factor of two. A reproducible net photocurrent exceeding 4 mA.cm⁻² was obtained. This result represents the highest performance reported for hematite under one sun illumination.

In Part C of this thesis, I present several synthesis methods for titania nanostructures acting as photoanodes in the DSC. In this photovoltaic cell, the electronic loss that is typically discussed is the slow transport induced recombination. Charges recombining before reaching the electrode have a detrimental influence on the photocurrent and photovoltage. Several approaches have been proposed in order to reduce interfacial recombination and improve charge collection in liquid electrolyte and solid state-DSCs (ss-DSCs) including the use of radial collection nanostructures, one-dimensional ZnO and TiO₂ nanorods, and nanowires as photoanodes. Even though these approaches show great promise, they have yet to achieve power conversion efficiencies above 5% in liquid electrolyte DSCs and 1.7% in ss-DSCs. In this part of my thesis, I expose results on the strategies I have pursued during the course of my PhD to improve the dynamics in the liquid and ss-DSC. From one dimensional titania nanotube arrays, I have moved to tri-dimensional fibrous network of crystalline TiO₂ and more complex host-passivation-guest photoelectrodes.

Keywords: Solar energy conversion, hydrogen, water splitting, metal-oxide semiconductor, hematite, Fe₂O₃, titania, TiO₂, photoanode, photoelectrochemical tandem cell, PEC cell, dye-sensitized solar cell, DSC, Graetzel cell, nanotube, nanostructu

Résumé

Les cellules photoélectrochimiques (PEC) reposant sur des semiconducteurs d'oxydes pour le clivage de l'eau représentent une voie potentiellement économiquement viable pour la génération d'hydrogène solaire. Au coeur du dispositif, une photoanode nanostructurée chargée de l'oxydation de l'eau est connectée en série à une ou deux cellules solaires à base de colorant (DSC). Cette dernière procure un potentiel électrique supplémentaire à l'électron qui pourra alors réduire l'eau à la contre électrode de platine.

Dans la partie A de cette thèse, après avoir passé en revue les différentes technologies disponibles pour produire de l'hydrogène solaire, je présente différentes architectures de cellules tandem photoanode / DSC rendues possibles par les récentes avancées du domaine. En premier lieu, le développement de colorants organiques à base de squaraine présentant une bande d'absorption étroite proche de l'infra rouge et une large bande transparente dans le domaine du visible ont permis la conception de nouvelles conformations de cellule tandem photoanode / DSC / DSC. La cellule tandem "DSC à l'arrière" dans laquelle deux DSCs côte à côte exploitent les photons transmis par la photoanode est l'architecture conventionnelle. Dans la présente étude, je démontre la possibilité d'utiliser la structure inverse, "DSC à l'avant", qui permet l'utilisation de substrats métalliques non transparents (et donc moins chers) pour la photoanode, ainsi que la structure "à trois niveaux" dans laquelle une DSC utilisant un colorant panchromatique (noir) exploite l'énergie transmise par une photoanode et une DSC utilisant un colorant squaraine. L'étude opto-électronique de chacun de ces trois dispositifs est réalisée et des efficacités solaire-à-hydrogène de respectivement 1.16 %, 0.76 % et 1.36 % sont déterminées. Pour terminer, je m'appuie sur les récentes trouvailles en matière de DSC à haut voltage pour démontrer de façon inédite une cellule tandem n'utilisant qu'une seule DSC pour totalement cliver l'eau à des efficacités pouvant aller jusqu'à 3.10 %. Ce résultat représente une amélioration d'un facteur 10 par rapport aux dispositifs du même type reportés jusqu'à maintenant. Ce travail est une véritable percée dans le domaine de la conversion d'énergie solaire en liaison chimique et constitue incontestablement une référence pour la production

de carburant solaire n'utilisant que des oxydes aisés à manipuler.

La partie B traite de la photoanode pour la réaction d'évolution de l'oxygène. L'hématite ou $\alpha\text{-Fe}_2\text{O}_3$ est un matériau prometteur du fait de sa disponibilité, de son coût bas, de sa non-toxicité et de sa bande interdite permettant une large absorption de photons dans le domaine du visible. Cependant, il souffre d'un certain nombre d'inconvénients, comme sa mauvaise conductivité de porteurs de charges majoritaires ainsi que sa courte longueur de diffusion des trous par rapport à la profondeur d'absorption des photons. Cette condition a pour effet de donner une faible probabilité aux charges photo-générées dans la masse du matériau d'atteindre l'interface semiconducteur / liquide afin de participer à la réaction d'oxydation de l'eau. L'implication immédiate est la nécessité d'utiliser des morphologies d'hématite ayant une dimensionnalité de l'ordre de la dizaine de nanomètres. L'approche liquide colloïdale offre une méthode aisée pour obtenir de l'hématite nanostructurée. Une mise à l'échelle est facilement envisageable. Cependant, pour ce type de système, une étape de recuit à 800 °C est nécessaire pour obtenir un matériau photo-actif. Cette particularité a été attribuée dans le passé à la diffusion d'atomes dopants provenant du substrat. Par ailleurs, ce recuit a pour effet de fritter les particules d'une taille de 10 nm à une dimension approchant les 100 nm. Dans cette partie, je montre d'abord l'effet d'une incorporation intentionnelle et contrôlée d'atomes dopants sur le frittage et la photo-activité. Ensuite, je démontre une méthode qui permet de garder le contrôle sur la taille des particules durant une étape de recuit à haute température. Cette stratégie, couplée à la passivation des états de surface a permis l'amélioration de la photo-activité nette d'un facteur 2. Un photo-courant de plus de 4 mA.cm⁻² a été obtenu de façon reproductible. Ce résultat représente la plus haute performance reportée pour l'hématite soumise à l'illumination solaire.

Dans la partie C de cette thèse, je présente plusieurs méthodes de synthèse de nanostructures d'oxyde de titane en tant que photoanode pour la DSC. Dans ce type de cellule photovoltaïque, les pertes électroniques généralement discutées concernent les recombinaisons dues au transport de charge lent. Les charges qui recombinent avant d'atteindre l'électrode ont un effet négatif sur le photo-courant et le photo-voltage. De nombreuses approches ont été proposées dans le but de réduire les recombinaisons aux interfaces et améliorer la collection de charges dans les DSC à électrolyte liquide et solide (SS-DSC), comme par exemple l'utilisation de nanostructures à collection radiale, de nano-cordes unidimensionnelles de ZnO et TiO₂ et de nanofils en tant que photoanode. Même si ces approches sont prometteuses, des efficacités de 5 % pour les cellules liquides et 1.7 % pour les cellules solides doivent être dépassées. Dans cette section de ma thèse, je présente des résultats sur les stratégies que j'ai envisagées pendant mon doctorat dans le but d'améliorer la dynamique de charges dans la DSC et ss-DSC. Des réseaux unidimensionnels de nanotubes de dioxyde de titane, j'ai évolué vers un réseau tridimensionnel fibreux de TiO₂ cristallin pour finalement m'intéresser à une structure hybride avancée.

Mots clés: Conversion d'énergie solaire, hydrogène, clivage de l'eau, semiconducteur de oxyde métallique, hématite, Fe₂O₃, dioxyde de titane, TiO₂, photoanode, cellule tandem photoelectrochimique, cellule PEC, cellule solaire à colorant, DSC, cellule Grätzel, nanotube, nanostructure.

List of abbreviations and symbols

α	Absorption coefficient
ALD	Atomic layer deposition
AM 1.5G	Air Mass 1.5 solar simulation
APCVD	Atmospheric pressure chemical vapor deposition
CB / VB	Conduction / valence band
$\Delta\mu_{ex}$	Chemical potential of the excited states
D4	Dual absorber tandem system using four photons per H ₂ molecule produced
DSC / ss-DSC	Liquid / solid state dye sensitized solar cell
E_g	Band gap energy (eV)
FTO	Fluorine doped tin oxide
EIS	Electrochemical impedance spectroscopy
ff	Fill factor
H-P-G	Host-passivation-guest
HOMO/LUMO	Highest occupied / lowest unoccupied molecular orbital
HPC	Hydropropoxy cellulose
HTM	Hole transport material
<i>IPCE</i>	Incident photon to current efficiency
<i>IQE</i>	External quantum efficiency
ITO	Indium doped tin oxide
J_{pl}	Plateau photocurrent
J_{sc}	Short circuit photocurrent
J_{op}	Operating photocurrent
J_{op-TH} / J_{op-IS}	Theoretical / <i>in situ</i> measured operating photocurrent
L_d	Diffusion length
η	Solar to electricity power conversion efficiency
η_{Farad}	Faradic efficiency
η_{ox} / η_{red}	Kinetic overpotentials at the oxidation / reduction reactions
η_{STH}	Solar to hydrogen conversion efficiency
$\eta_{STH,max}$	Theoretical maximum solar to hydrogen conversion efficiency
OER / HER	Oxygen / Hydrogen evolution reaction
ϕ_{conv}	Quantum conversion efficiency
ϕ_{photon}	Incident photon flux
PEC	Photoelectrochemical
PEDOT	Poly(3,4-ethylenedioxythiophene)
PEN	Poly(ethylene 2,6-naphthalate)
PTFE	Polytetrafluoroethylene
PV	Photovoltaic
q	Elementary charge
RHE	Reversible hydrogen electrode
RIE	Reactive ion etching
<i>RPI</i>	Relative percent increase
S1	Single absorber system using two photons per H ₂ molecule produced
SCLJ	Semiconductor - liquid junction

SEM	Scanning electron microscopy
T6	Triple absorber tandem system using six photons per H ₂ molecule produced
TCO	Transparent conductive oxide
TEOS	Tetraethyl orthosilicate
TEM	Transmission electron microscopy
TMA	Tetramethylammonium
TNT	Titania nanotube
U_{oc}	Open circuit potential
U_{op}	Operating potential
UV / IR	Ultraviolet / infrared part of the spectrum
W	Space charge layer width
XPS	X-ray photoelectron spectroscopy
XRD	X-ray diffraction

Contents

ABSTRACT	5
RESUME	7
List of abbreviations and symbols.....	9
CHAPTER 1. PREFACE.....	13

PART A

TANDEM CELLS FOR PHOTOELECTROCHEMICAL WATER SPLITTING 19

CHAPTER 2. TANDEM PHOTOELECTROCHEMICAL CELLS FOR SOLAR WATER SPLITTING..... 25

2.1 <i>Strategies and limitations of multi-absorber systems.....</i>	<i>25</i>
2.2 <i>PV/PV strategies.....</i>	<i>30</i>
2.3 <i>Photoelectrode/PV systems.....</i>	<i>32</i>
2.4 <i>Photoanode/photocathode systems.....</i>	<i>35</i>
2.5 <i>Practical device design considerations.....</i>	<i>37</i>
2.6 <i>Summary and outlook.....</i>	<i>39</i>
2.7 <i>References</i>	<i>39</i>

CHAPTER 3. EXAMINING HEMATITE / DYE-SENSITIZED SOLAR-CELL T6 TANDEM ARCHITECTURES..... 45

3.1 <i>State of the art, Motivations.....</i>	<i>45</i>
3.2 <i>Hematite/2×DSC Tandem architectures</i>	<i>46</i>
3.3 <i>Experimental.....</i>	<i>48</i>
3.4 <i>Anticipating device performances.....</i>	<i>49</i>
3.5 <i>Conclusion</i>	<i>58</i>
3.6 <i>References</i>	<i>59</i>

CHAPTER 4. UNASSISTED WATER SPLITTING USING A LOW COST DUAL- PHOTOSYSTEM TANDEM CELL..... 61

4.1 <i>Devices for water photolysis, a balance between performances and complexity</i>	<i>62</i>
4.2 <i>Photoanode/DSC D4 tandem-cell</i>	<i>62</i>
4.3 <i>Predicting device performances</i>	<i>64</i>
4.4 <i>Measuring device performances.....</i>	<i>68</i>
4.5 <i>Conclusion</i>	<i>71</i>
4.6 <i>References</i>	<i>72</i>

PART B

SOLUTION BASED COLLOIDAL HEMATITE PHOTOANODE FOR WATER OXIDATION..... 75

CHAPTER 5. CONTROLLING PHOTO-ACTIVITY OF SOLUTION-PROCESSED HEMATITE ELECTRODES FOR SOLAR WATER SPLITTING 81

- 5.1 Introduction 82
- 5.2 Results and discussion..... 84
- 5.3 Conclusions 88
- 5.4 References 89

CHAPTER 6. DECOUPLING FEATURE SIZE AND FUNCTIONALITY IN SOLUTION-PROCESSED, POROUS HEMATITE ELECTRODES FOR SOLAR WATER SPLITTING ... 91

- 6.1 Functionality vs. Morphology conundrum..... 92
- 6.2 Decoupling by encapsulation..... 94
- 6.3 Smaller particles give higher photocurrents 96
- 6.4 Attempt in passivating the surface..... 101
- 6.5 Conclusion 103
- 6.6 References 104

PART C

NANOSTRUCTURES FOR THE DYE SENSITIZED SOLAR CELL..... 107

CHAPTER 7. ONE-DIMENSIONAL PHOTOANODES FOR THE DSC..... 113

- 7.1 Application of highly ordered TiO_2 nanotube- arrays in flexible Dye-sensitized Solar Cells..... 114
- 7.2 Solid-state dye-sensitized solar cells using TiO_2 nanotube arrays on FTO glass..... 119
- 7.3 Conclusion 125
- 7.4 References 126

CHAPTER 8. THREE-DIMENSIONAL TITANIA NANOSTRUCTURES FOR FAST CHARGE EXTRACTION..... 129

- 8.1 Improved charge dynamics through a 3D host-passivation-guest electrode. 129
- 8.2 Fast charge extraction through a 3D Fibrous Network of Crystalline TiO_2 Nanowires in a Solid State DSC..... 136
- 8.3 Conclusion 144
- 8.4 References 146

CHAPTER 9. FINAL CONCLUSION, OUTLOOK AND RECOMMENDATIONS 153

- 9.1 Tandem cells for photoelectrochemical water splitting..... 154
- 9.2 Solution based colloidal hematite photoanode for water oxidation..... 155
- 9.3 Nanostructures for the dye sensitized solar cell..... 156
- 9.4 Outlook and recommendations..... 157
- 9.5 Last word..... 159

APPENDIX..... 161

ACKNOWLEDGEMENTS.....183

CURRICULUM VITAE AND LIST OF PUBLICATIONS.....185

Chapter 1. Preface

*“We are like tenant farmers
chopping down the fence around our house for fuel
when we should be using Nature's inexhaustible
sources of energy — sun, wind and tide.*

*I'd put my money on the sun
and solar energy. What a source of power! I hope we
don't have to wait until oil and coal run out before we
tackle that.”*

Thomas Edison, 1931

The way mankind exploits, uses and shares natural resources, energy in particular, is an issue. Nobel laureate Richard Smalley, the father of the « Buckyball », was classifying Energy in the first position of the “Top Ten Problems of Humanity for Next 50 Years” in his last presentations.¹ This simple assessment illustrates the importance of the matter. The unquestionable depletion of carbon based energy sources not only has a dramatic impact on the economy and the environment² but also generates coercion on the diplomatic relations between oil producing countries and other nations, sometimes even leading to military interventions in order to try to secure oil. The situation is predicted to be extremely challenging in the next decades as the demand of energy increases³ due to demographic pressure as well as the rising of gigantically habited Newly Industrialized Countries (NIC) with medium to high Human Development Index (HDI) such as China, India, Brazil and Mexico. Those developing countries account for two thirds in the predicted energy demand of 60% by 2030.⁴

In the past couple years, several events have highlighted the security, economic, and human costs of relying so heavily on fossil and nuclear energy. The three-month long BP oil spill in the Gulf of Mexico caused extensive damage and continues to affect the economy and welfare of people in the region. The “Arab

Spring” of popular unrest has triggered oil-price volatility and added instability to energy markets, while at the same time the global demand for oil is outpacing the capacity for production. And Japan’s Fukushima nuclear catastrophe has led many countries to reconsider the role of nuclear energy in providing low-carbon electricity.⁵ Those events are an incentive for the international community to rethink energy production, distribution and consuming habits.

Energy is not only a problem. It is also foreseen as a lever for achieving the Millennium Development Goals.^{4,6} Addressing the energy needs of the developing world is a complex and multidisciplinary challenge but is necessary to provide services such as health and education and is a central factor for reaching higher HDI. In particular, medium sized decentralized energy production units are identified as key elements since about a third of the world’s population lives far beyond the electricity networks, mostly in rural areas, without access to health care, education, communication and enterprise opportunities that modern energy can facilitate. Demand for energy by this un-served population is growing much faster than the rate of expansion of the conventional grid.⁴

In 1992, UN Secretary General Boutros Boutros-Ghali urged the world to subscribe to the Rio Declaration on Environment and Development, promoting the idea of sustainable development, to which most countries agreed on. An action plan was further decided, voted by 178 governments and is now known as the Agenda 21, and the United Nations Framework Convention on Climate Change (UNFCCC) was signed by 170 countries. The energy challenge therefore needs to be addressed by taking in consideration the “triple bottom line” of sustainability, that is to say accounting for the environmental, social, and economic aspects of the solutions. Prof. David MacKay proposes three routes to bridge the energy gap in the UK: reducing the population, changing peoples lifestyle, and reducing the energy intensity through “efficiency” and “technology”.⁷ The two first propositions are frightening and inefficient on a global scale, respectively. This thesis is about the third. Innovation and technology is at the center of the strategic development of the European Union, for instance, who spends about 10 billion euros each year on research through its famous seventh framework program (FP7) alone.⁸

More than a hundred countries have given themselves renewable energy

policies such as regulatory policies, fiscal incentives and public financing, including middle to low income countries such as Bangladesh and Ethiopia.⁵ The recent Special report on Renewable Energy Sources and Climate Change Mitigation published by the UN Intergovernmental Panel on Climate Change (IPCC) points out the crucial role of policy makers in accelerating the development of renewable technologies. The best illustration of this point is that, despite the recession, total global investment in renewable energy broke a new record in 2010. Investment in renewable power and fuels reached \$211 billion, up 32% from \$160 billion the previous year. Developing country investments in renewable energy companies and utility-scale generation and biofuel projects exceeded those of developed countries, with China attracting more than a third of the global total.⁹

Solar energy is of particular interest. First, the amount of energy radiating on the planet from the sun is enormous (174,000 TW) compared to the world's consumption (15 TW). This means that every single hour, the earth receives enough photons to power its entire population for a full year. Second, solar radiation is distributed fairly uniformly on the surface of the earth, with even higher irradiance in the southern hemisphere. If carefully done by local actors, exploiting this resource could be a development factor for nations that are usually left apart, in particular on the African and South American continents. Finally, the science behind solar energy conversion is fairly well known. Edmond Bequerel discovered the photovoltaic effect in 1839, a first solar cell was made in 1883 by Charles Fritts and in 1905, Albert Einstein pioneered theoretical work on the photoelectric effect (for which he received the Nobel Prize).

Solar energy not only needs to be converted into electricity. It needs to be stored in order to avoid the costly mismatch between the weather dependent time where the energy can be produced and the human activity dependent time where the energy is consumed, especially for off-grid application. In addition, it has been estimated that a conventional power network can only support about 30% of intermittent renewable energy beyond which a large amount of the production has to be dumped.¹⁰ One option is to store the energy directly into chemical bonds to form a so-called "solar fuel". The possibility of seeing the raise of a "clean fuel" economy is greatly supported by the fact that the economical model that we use is adapted for the distribution and trade of liquid or gaseous energy vectors such as oil and natural gas.

Hydrogen is a simple molecule with high energy density. It is the most abundant element in the universe and can be obtained relatively easily by splitting water, the most abundant compound on Earth's surface. Splitting the water contained in an Olympic sized swimming pool would provide enough hydrogen to fuel world's demand for three seconds. Splitting all of the water contained in lake Geneva would give three years worth of fuel.

The potential of solar hydrogen obtained by water splitting is immense but the technological challenge is complex. The technologies developed have to include materials that are made from elements that are abundant in the crust of the earth, fairly spread, non-toxic, benign for the environment and dirt-cheap in order to reach the sustainability standards as well as penetrate a competitive market.

In this thesis, I show the most recent advances toward inexpensive solar energy conversion and storage with a solution compatible with the idea of sustainability.

1. Smalley, R. E. Top Ten Problems of Humanity for Next 50 Years. *Energy & NanoTechnology Conference, Rice University* (2003).
2. *Climate Change 2007 (AR4), IPCC Fourth Assessment Report, Core Writing Team, Pachauri, R.K. and Reisinger, A. (Eds.).* (The Intergovernmental Panel on Climate Change: 2007).
3. *World in Transition – Towards Sustainable Energy Systems, Flagship Report 2003.* (German Advisory Council on Global Change: Earthscan, London, 2003).
4. *Renewable Energy Services for Developing Countries, In support of the Millennium Development Goals: Recommended Practice & Key Lessons.* (International Energy Agency: 2008).
5. *Renewables 2011.* (REN21: 2011).
6. UNhabitat *The Energy Challenge for Achieving the Millennium Development Goals.* (United Nations: 2005).
7. MacKay, D. *Sustainable Energy – Without the Hot Air.* (2008).
8. *The homepage of the European Commission.* at <http://ec.europa.eu/>
9. *Global Trends in Renewable Energy Investment 2001, Analysis of Trends and Issues in the Financing of Renewable Energy.* (United Nations Environment Programme: 2011).
10. Nikolakakis, T. & Fthenakis, V. The optimum mix of electricity from wind-and solar-sources in conventional power systems: Evaluating the case for New York State. *Energy Policy* 39, 6972–6980 (2011).

Part A
Tandem cells for
Photoelectrochemical Water
Splitting

The realization of an energy economy based on solar hydrogen is contingent on identifying a scalable system for solar H₂ production at costs commensurate with the price of H₂ generated from conventional sources (\$2–3 kg⁻¹ for the steam reforming of natural gas)¹. Thus a balance between minimizing system complexity and maximizing energy conversion efficiency and device longevity must be considered for any practical solar H₂ production. The most straightforward approach for solar H₂ production uses artificial photosynthesis through photoelectrochemical (PEC) water splitting. It employs a single semiconductor photoelectrode as a light absorber and charge generator in combination with a metal counter electrode. Here, hydrogen can be produced from water upon the absorption of two photons (under the condition that one electron-hole pair is produced for each photon absorbed) since the water reduction reaction requires two electrons to make one molecule of H₂. This single-absorber, two-photon approach (more simply called S2) appears quite promising at first glance but several losses factors imply the use of more complex photoelectrochemical systems.

Since only 1.23 V are needed for water splitting at standard conditions from a thermodynamic standpoint, one could credulously believe that a semiconductor with a minimum band-gap, E_g , of 1.23 eV (an absorption wavelength cut-off of 1008 nm) could be effective. Based on the standard AM1.5G solar spectrum (1000 W.m⁻²), a

semiconductor with a such a band-gap would operate at maximum overall solar-to-hydrogen conversion efficiency, η_{STH} , of 47.4% assuming a unity quantum conversion efficiency ($\phi_{conv} = 1$) and no other losses.² However significant loss processes are involved and are unavoidable in any energy conversion process.

Firstly, there is an entropic energy loss resulting from the amount of work that must be done to extract the excited states. Next, kinetic overpotentials exist at both electrodes, η_{ox} and η_{red} , resulting from the energies necessary to form the intermediate species involved in the complex water reduction and oxidation reaction mechanisms. The overpotential of the oxidation reaction, η_{ox} , is notoriously large (0.2 – 0.4 eV) for reasonable current densities (ca. 10 mA.cm⁻²) given the four-electron nature of the oxygen evolution reaction (OER) even using the best catalysts.³

These loss processes imply that a semiconductor with E_g much greater than 1.23 eV must be used to realize S2 PEC water splitting. Since a semiconductor can only harvest photons with wavelength (λ) satisfying $E_g < hc/\lambda$, where h is the plank constant and c the speed of light, the requirement to use a material with a larger band-gap implies a lower possible η_{STH} . Indeed, while the ideal (Schottky-Queisser) solar energy conversion limit using one absorber material is 34%, Weber and Dignam² followed by Bolton et al.⁴ analysed the “upper limit” for η_{STH} using S2 water splitting with realistic losses and reported maximum values of 11.6% (using $E_g = 2.2$) and 17% (using $E_g = 2.03$), respectively. The latter report additionally considered photon absorption and collection losses and estimated that 10% should be entirely feasible with an S2 approach. In practice, the realization of a S2 PEC water splitting device with $\eta_{STH} = 10\%$ is clearly a difficult task. A review by Walter *et al.*³ summarizes decades of progress on using either a photocathode or a photoanode for S2 water splitting. While many promising S2 photocathodes exist (e.g. GaP and InP), their cost and stability in aqueous environments remain critical limitations. Semiconductor oxide photoanodes offer unmatched stability for water splitting but, due to the large energy loss processes discussed, above materials with band-gaps greater than 3.0 eV (e.g. SrTiO₃ and KTaO₃) must be employed limiting η_{STH} to less than 2.3%.

It remains possible that a single semiconductor material that possesses the optimum band-gap, conduction and valence band levels, stability and availability will

be identified, and a device exploiting the S2 approach will realize over 10% η_{STH} . However, the failure to do so after decades of work has led researchers to consider alternative approaches. This chapter introduces an approach to PEC water splitting that increases system complexity but also energy conversion efficiency. By employing multiple light absorbers in tandem, PEC systems can both harvest a significant portion of the solar spectrum and provide enough chemical potential of the excited states, $\Delta\mu_{ex}$ to afford water splitting at high η_{STH} . In the next chapters, various approaches using multi-absorber systems will be presented, analysed, and discussed using examples from literature. In addition, since the primary goal of PEC research is to develop a system that balances system complexity, cost, and efficiency, systems using cheap hematite photoanodes together with dye sensitized solar cells will be presented and discussed.

1. National Research Council US Committee on Alternatives, Production, S. F. F. H., Use & National Academy of Engineering The Hydrogen Economy. (2004).
2. Weber, M. & Dignam, M. Efficiency of splitting water with semiconducting photoelectrodes. *J Electrochem Soc* 131, 1258–1265 (1984).
3. Walter, M. G. et al. Solar water splitting cells. *Chem. Rev.* 110, 6446–6473 (2010).
4. Bolton, J. R., Strickler, S. J. & Connolly, J. S. Limiting and realizable efficiencies of solar photolysis of water. *Nature* 316, 495–500 (1985).

Chapter 2. Tandem photoelectrochemical cells for Solar water splitting

2.1 Strategies and limitations of multi-absorber systems

2.1.1 “Brute force” strategies

The most obvious approach to accumulate sufficient chemical potential ($\Delta\mu_{ex}$) for water splitting with semiconductor materials that can also absorb a large fraction of the solar spectrum is to connect multiple photovoltaic (PV) cells in series. For example, a traditional pn-junction silicon PV produces a potential of 0.5 – 0.6 V at its maximum power point under standard conditions. Thus three of these connected electrically in series would create sufficient potential to split water. This “brute force” PV + electrolysis approach is limited by the price and availability of PV devices and electrolysers, which, at the time of this writing makes the price of the H₂ produced around \$10 kg⁻¹.¹ Nevertheless, a fair amount of interest has followed this path and overall η_{STH} 's up to 9.3% have been demonstrated using single crystal silicon PV modules and high-pressure electrolysis.² It has also been suggested that a complete optimization of these systems could deliver H₂ at a price of \$4 kg⁻¹.³ This price may decrease further by employing novel thin-film PV technologies. For example, Dhere

and Jahagirdar have reported the use of two high voltage $\text{CuIn}_{1-x}\text{Ga}_x\text{S}_2$ (GIGS) PV cells side-by-side to generate a η_{STH} up to 8.8%.^{4,5} A major drawback with the brute force approach in general comes from the voltage output of a pn-junction, which is strongly dependent on the illumination intensity. This necessitates complicated switching mechanisms to ensure the optimum number of cells is connected in series during variations in light intensity caused by haze or cloud cover.

2.1.2 The tandem cell concept

Besides using PV cells side-by-side to obtain sufficient voltage for water splitting, cells can be stacked on-top of one another, in tandem, if they can individually harvest different portions of the solar spectrum. The first (top) cell, with band-gap E_{g1} absorbs photons from the sun with a wavelength smaller than $\lambda_l = hc / E_{g1}$. Photons with $\lambda > \lambda_l$ are transmitted through to the next cell with a band-gap $E_{g2} < E_{g1}$, and so on (see Figure 2.1). If the cells are connected electrically in series the total photocurrent density will be limited by the cell producing the least current, but the total voltage will be the addition of all the cells used.

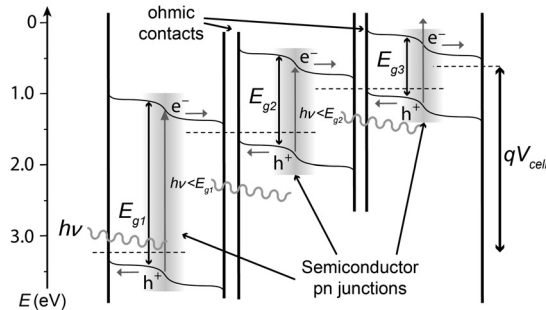


Figure 2.1 : Electron energy scheme of a generic tri-level tandem cell for solar energy conversion. Here three semiconductors (E_{g1-3}) are employed as pn-junctions and connected by transparent ohmic contacts to give a final photopotential of V_{cell} .

This tandem cell strategy not only gives access to a high overall cell voltage, it also significantly enhances the upper limit of solar power conversion (solar-to-electricity) efficiency from 34% in the one absorber case to 42% (2 cells), 49% (3 cells), or 68% (for an infinite number of cells) for unconcentrated sunlight.⁶ Of course using an infinite number of cells is not possible and, in practice, the addition of each layer brings technical difficulties and additional optical and electrical losses that greatly increase the complexity and cost of these devices. Nevertheless, the precise control of materials used and device architecture (typically triple-junction epitaxially grown III-

V semiconductor devices) has pushed the solar-to-electricity power conversion efficiency, η , past 40%,⁷ but the high cost of producing these devices relegates their use to specific niches (e.g. extra-terrestrial application). The use of these types of “PV/PV” tandem cells for PEC water splitting will be discussed in section 2 of this chapter.

2.1.3 *The D4 strategy and its potential*

While very impressive photovoltaic efficiencies have been demonstrated using triple junction cells as mentioned above, the maximum possible η_{PC} does not change significantly from 2 to 3 cells (from 42 to 49%). This brings into question the return on the device complexity added by the third cell. In addition, gaining the $\Delta\mu_{ex}$ necessary for water splitting should be feasible with only two light absorbers. In fact, a two-photosystem solution is precisely what evolved in plant photosynthesis, which uses sunlight to split water and stores the energy in carbohydrate vectors. In a dual-absorber approach where each absorbed photon creates one excited electron-hole pair, four photons (two in each absorber) must be absorbed to create one molecule of H_2 . Following Bolton’s convention,⁸ this is designated a D4 approach. A simple way to accomplish D4 water splitting is to use a separately illuminated photoanode and photocathode in a side-by-side (not tandem) configuration. Weber and Dignam⁹ evaluated the potential η_{STH} of this approach and reported an upper limit of 16.6% with $E_{g1} = E_{g2} = 1.4$ eV—a modest increase over the 11.6% predicted with an S2 approach. However, using an integrated tandem D4 approach where the two absorbers are superimposed, 22% η_{STH} was predicted to be possible with $E_{g1} = 1.8$ eV and $E_{g2} = 1.15$ eV. In real systems, reflection and scattering losses exist, but can be addressed with device engineering. Figure 2.2 (top) shows a contour plot of a reasonable upper limit for η_{STH} as it depends on the chosen semiconductor cut-off wavelengths, λ_1 and λ_2 , prepared by using equations from Bolton’s formalism and the assumptions of a quantum conversion efficiency (Φ_{conv}) and a faradic efficiency (η_{Farad}) both equal to unity with losses $U_{loss} = 1.4$ eV total.

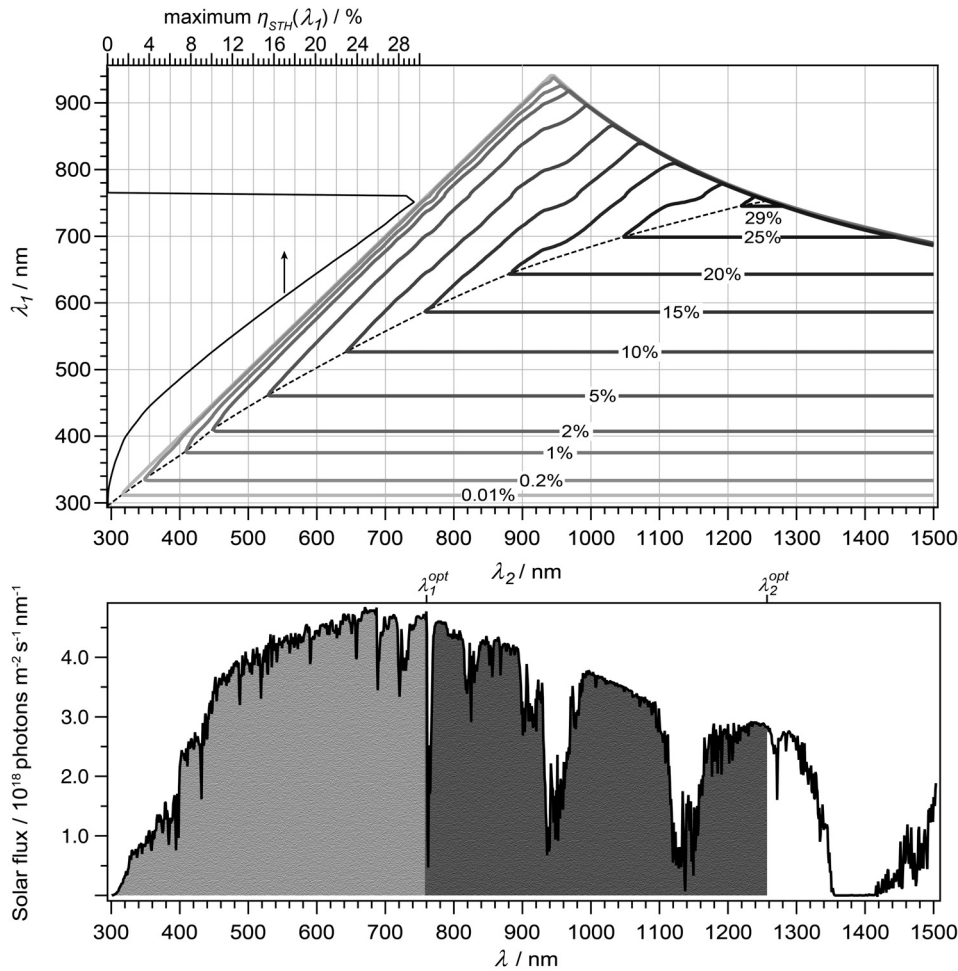


Figure 2.2 : (Top) Contour plot (thick grey lines) showing the maximum reasonable η_{STH} with AM 1.5G incident radiation (1000 W m^{-2}) and an total loss, U_{loss} , set at 1.4 eV as it depends on the chosen semiconductor cut-off wavelengths, λ_1 and λ_2 where ($\lambda_i = hc / E_{gi}$, $i = 1, 2$, with $E_{g1} > E_{g2}$). The maximum η_{STH} as it depends on the choice of the wider band-gap absorber (λ_1) is also shown (thin black line). See text for full explanation. (Bottom) The AM 1.5 G solar photon flux as a function of wavelength. The optimum values of λ_i are indicated and the areas corresponding to the photons harvested by each absorber layer are shaded.

The shapes of the contours (thick grey lines), which represent values of λ_1 and λ_2 that result in the same η_{STH} , are easily rationalized. First, the contours remain to the right side of the 45° line because as this is where the set condition $E_{g1} > E_{g2}$ is satisfied. The upper-right region, where η_{STH} is undefined, represents semiconductor combinations that do not possess sufficient $\Delta\mu_{ex}$ for water splitting in a D4 configuration given U_{loss} . Calculating the upper limit of η_{STH} and optimum λ_1 , λ_2 pairing for an arbitrary system can be simply done with Figure 2.2 by first choosing λ_1 . For example take $\lambda_1 = 477 \text{ nm}$ ($E_{g1} = 2.6 \text{ eV}$), which corresponds to WO_3 , material commonly used as a semiconductor photoelectrode for water splitting.¹⁰ A horizontal line drawn at $\lambda_1 = 477 \text{ nm}$ would intercept first with the solid black maximum- η_{STH}

line. Reading the value on the top scale gives the maximum value of η_{STH} for WO_3 as 6.3%. Continuing back on the imagined horizontal line at $\lambda_1 = 477$ nm further, it intercepts with a dashed black line running against the contour lines. This line represents the values of λ_1 and λ_2 that meet the current matching condition. Reading the value of λ_2 at that point gives $\lambda_2 = 561$ nm and thus the minimum value for $E_{g2} = hc/\lambda_2 = 2.2$ eV. Choosing larger λ_2 (smaller E_{g2}) will not result in a higher η_{STH} as the photocurrent will be limited by the top absorber, λ_1 . For this reason the grey contour lines are all horizontal to the right of the dashed black “current matching line”.

To identify the optimum values for both λ_1 and λ_2 with $U_{loss} = 1.4$ eV the current matching line can be followed for increasing λ_1 and λ_2 (and η_{STH}) until the maximum η_{STH} of 29.9% with $\lambda_1 = 755$ and $\lambda_2 = 1253$ nm. The distribution of the photons harvested by each absorber in this optimum case can be visualized in the bottom of Figure 2.2 where the AM 1.5G solar photon flux is plotted as a function of the wavelength. The optimum values for λ_1 and λ_2 are indicated and shaded areas indicate photons harvested (lighter shading for λ_1). The areas of the two shaded regions in this plot are identical as the optimized circumstances exactly satisfy the current matching condition. By coincidence the cut off for absorber 1, λ_1 , coincides with the sharp dip in the solar spectrum at 762 nm, which is due to the weak spin-forbidden electronic absorption of molecular oxygen.

Overall the model presented in this section gives only reasonable expected maximum values for η_{STH} , which can be of use in describing the basic capability (or limitations) of specific materials or materials combinations. This is certainly of use in determining the interest in developing specific systems. However, the model does not include any additional constraints on selecting the materials with respect to the conduction and valence band energy levels, or work function factors that add to the difficulty of finding ideal and complementary materials for a water splitting tandem cell.

2.1.4 D4 device architectures

An important practical consideration for tandem cell construction beyond band-gap selection is the types of junctions used. Many groups have investigated tandem cells where one or both of the absorbers are in direct contact with the aqueous

electrolyte. In addition, alternative photoelectrochemical devices, like dye sensitised solar cells (DSCs) can also be employed as one of absorbers in a tandem scheme. Thus many D4 configurations are possible. Figure 2.3 shows, from an energy perspective, two classic examples in addition to the PV/PV combination previously mentioned.

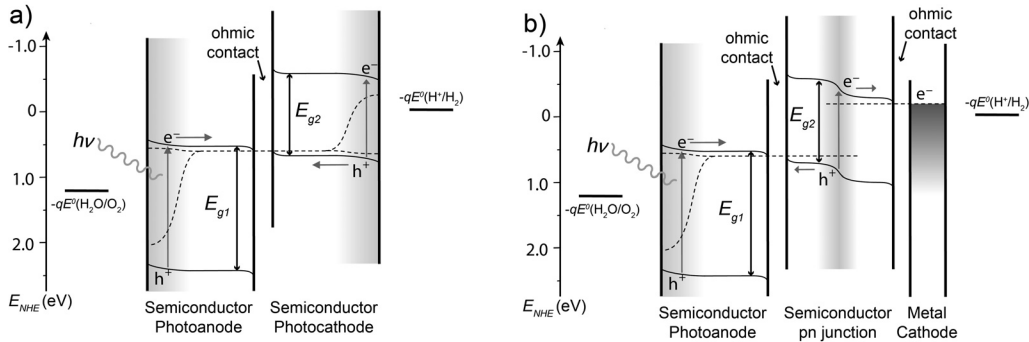


Figure 2.3 : Electron energy schemes of two possible D4 tandem water splitting device configurations: a) shows an n-type photoanode connected to p-type photocathode and b) shows an n-type photoanode with a pn-junction.

The p-type photocathode/n-type photoanode device (Figure 2.3a) is the simplest in terms of junctions with only one interconnect between the two semiconductors together with two semiconductor / liquid junctions (SCLJs). Here materials must be chosen such that when the device is in contact with the electrolyte $CB_2 < -qE_0(\text{H}^+/\text{H}_2) < CB_1 < VB_2 < -qE^0(\text{H}_2\text{O}/\text{O}_2) < VB_1$ where VB_i and CB_i represent the valence band and conduction band energy levels of semiconductor i , respectively. A similar situation is necessary for a photoelectrode/PV configuration (Figure 2.3b) with the added complication of aligning an additional n-type energy level and the work function of the metal electrode used to perform the reduction reaction (typically necessary as the semiconductors employed for PV cells are not stable when performing the water splitting reaction).

Despite the constraints on both the material's band-gap and energy levels, various material combinations have been demonstrated in D4 configurations. Specific examples can be categorized as photocathode/photoanode, photoelectrode/PV, or PV/PV. In the next sections specific examples of these configurations are explored.

2.2 PV/PV strategies

Devices employing two or more pn-junctions in tandem have attained the highest reported η_{STH} .^{11,12} Champion devices use the well-known band-gap engineering of III-V semiconductor systems to optimize light harvesting and $\Delta\mu_{ex}$. In

particular, Licht et al. have employed an AlGaAs/Si (pn-pn) structure using Pt-black and RuO₂ as reduction and oxidation catalysts, respectively, and obtained solar-to-hydrogen conversion efficiencies as high as 18.3% under simulated AM0 sunlight (135 mW.cm⁻²).^{13,14} Turner and co-workers have investigated monolithic GaAs/GaInP₂ (pn-p, pn-pn, or pn-pn-p) systems and attained η_{STH} up to 12.5%.¹⁵⁻¹⁷ While the conversion efficiencies reported with these systems are quite impressive, major concerns exist about the price (due to the requirements of high material purity and costly fabrication methods) and stability of these devices when they are used in contact with aqueous electrolyte.¹⁸

One other system of particular interest is based on amorphous silicon (a-Si). Bockris and co-workers first showed that a triple stack of n-type/intrinsic/p-type (nip) a-Si (not a D4 system, but rather a T6 system as 6 photons need to be absorbed by three absorbers for one H₂) on a Ti substrate could give up to $\eta_{STH} = 7.5\%$ under AM1 (100 mW.cm⁻²) illumination when islands of Pt and RuO₂ were used as a reduction and oxidation catalysts, and the device was directly submerged into aqueous electrolyte.¹⁹ Since the band-gap of the a-Si was the same for each nip-junction, the layer thicknesses were optimized so each layer produced the same photocurrent (i.e. the top two layers were thin enough to transmit some photons with energy $h\nu > E_g$). This concept was later extended to increase the efficiency for electricity production by mixing some Ge in with the Si to modify the E_g of the bottom two layers.²⁰ Using these devices for water splitting, an η_{STH} of 7.8% under AM1.5 (100 mW.cm⁻²) illumination was achieved in 1 M KOH with CoMo (reduction) and NiFe_yO_x (oxidation) catalysts.²¹ The stability of these devices was improved to greater than 31 days while maintaining 5–6% η_{STH} using a fluorine-doped SnO₂ protection layer on the cathode.²² More recent efforts with these devices have also shown that operation at near neutral pH is possible with $\eta_{STH} = 4.7\%$.²³ While these a-Si based devices are presumably less expensive than III-V semiconductor based tandem cells, their fabrication still requires relatively expensive vacuum processing. Despite this, at the time of this writing, the mass production of triple junction a-Si device modules for photovoltaic energy conversion is beginning by several companies. It is yet unclear what the price per kg H₂ would be if these cells would be used for water splitting. Furthermore, the open-circuit voltages produced by such triple junction a-Si cells are around 2.4 V—much higher than is needed for water electrolysis. The optimization of

this class of devices specifically for solar water splitting has yet to be accomplished.

2.3 Photoelectrode/PV systems

The most widely recognized Photoelectrode/PV device is a monolithic, epitaxially grown III-V semiconductor system developed by Turner and co-workers with a GaAs pn-junction coupled to a GaInP₂ photocathode.¹⁷ While the performance of this system was impressive at $\eta_{STH} = 12.5\%$, the GaInP₂ photocathode quickly corrodes when in contact with the aqueous electrolyte.²³ In general, this is a major drawback of using direct semiconductor-liquid junctions. However, with certain semiconductors the photoelectrode/PV system has many advantages.

2.3.1 *Advantages and operation of a photoanode/PV tandem cell:*

Identifying semiconductor materials that form stable junctions with water under illumination has been a major challenge in the field of PEC water splitting. Transition metal oxide semiconductors have, however, excelled in this aspect with the prototype being TiO₂.^{24,25} Unfortunately, a conundrum exists for transition metal oxides with respect to their band-edge energy levels and band-gap. Thus, for a transition metal oxide to have a small enough E_g for adequate solar light harvesting, its CB potential must be well below the water reduction potential. This excludes them from being used in a S2 water splitting scheme but essentially makes them ideal for use as photoanodes in a D4 tandem cell. Moreover, the difficulty in identifying a stable p-type cathode makes a photoanode/PV tandem device a good compromise with device complexity and stability.

Since there are several examples of this type of tandem cell, it is useful to illustrate general device function. Chapters 3 and 4 of this thesis propose a model to anticipate operating currents (J_{op}) and, accordingly, the η_{STH} by looking at spectral optical and electrical response of the discrete elements of the device. In the following sections, different photoelectrode / PV approaches and state of the art devices are reviewed.

2.3.2 *Photoanode/PV examples*

The possibility of a photoanode/PV tandem device to employ a stable

transition metal oxide photoanode and a complimentary PV device has attracted many research groups to investigate various promising systems. For example, a TiO₂ photoanode in tandem with a thin film PV device based on Cu(In,Ga)Se₂/CdS produced hydrogen at a rate of 0.052 $\mu\text{L}\cdot\text{s}^{-1}\cdot\text{cm}^{-2}$ during unassisted solar water splitting (corresponding to an external quantum efficiency of 1.02%).²⁶ While less interest has been paid towards using the prototypical TiO₂ as a photoanode due to its large band-gap ($E_g = 3.2$ eV, $\max \eta_{STH} = 2\%$) this work demonstrated the importance of using optimized protective layers (Nb_{0.03}Ti_{0.97}O_{1.84} in this case) to eliminate corrosion of the PV cell in the aqueous conditions.

Further research efforts have focused on using more promising transition metal oxides like WO₃, and Fe₂O₃. According to Figure 2.2, WO₃ ($E_g = 2.6$ eV) can potentially convert up to 6.3% of the AM1.5G sunlight into hydrogen. Hematite (α -Fe₂O₃) is a more promising transition metal oxide with a band gap of 2.1 eV. This corresponds to a maximum η_{STH} of 15.4% according to Figure 2.2, if a second absorber with $\lambda_2 > 774$ nm ($E_{g2} < 1.6$ eV) is used. Besides its relatively small band-gap, α -Fe₂O₃ is the most stable form of iron oxide and both iron and oxygen are ubiquitous atoms in the earth's upper crust, making hematite an outstanding candidate for solar energy conversion on a scale commensurate with the global energy demand. Furthermore, both WO₃ and Fe₂O₃ photoanodes can be prepared by inexpensive solution-based techniques.²⁷

Miller and co-workers have investigated combining tungsten²⁸ or iron²⁹ oxide photoanodes in tandem with a-Si:Ge PV. As a drawback, the large overpotential for water oxidation (η_{ox}) and the relatively low U_{oc} of a a-Si device requires a double junction PV in tandem to provide sufficient potential to drive the overall water splitting reaction (similar to the PV only T6 tandem case where 3 pn-junctions were needed with a-Si). Despite this, 3% η_{STH} was obtained with the WO₃/a-Si:Ge/a-Si:Ge device.²⁸ A similar device for iron oxide with only one PV (Fe₂O₃/a-Si:Ge) did not split water without an external bias, but it was shown that a 0.65 V bias “savings” was earned under AM1.5G illumination.²⁹ This result could reasonably be improved with the recent advances in α -Fe₂O₃ photoanode performance³⁰ as will be discussed later in Chapters 5 and 6.

2.3.3 *The photoanode/DSC tandem cell*

From a practical perspective, the attractive aspects of using a widely available, highly stable and inexpensively produced photoanode are diminished when using a tandem component that requires relatively expensive processing techniques (e.g. the chemical vapour deposition of a-Si). Thus more recently, investigations have focused on using next-generation photovoltaics that can also be fabricated with inexpensive, solution processed methods. The dye-sensitized solar cell (DSC) is the prototype example³¹ of this class of photovoltaic device and thus has attracted significant attention for use in solar water splitting tandem cells with a stable photoanodes.³²

The photoanode/DSC combination was first suggested by Augustynski and Grätzel³³ with WO_3 as the photoanode suggesting that device would be capable of 4.5% η_{STH} given the performance of the two devices.³⁴ In practice, tandem devices with WO_3 have been constructed by Park and Bard³⁵ and Arakawa et al.³⁶ giving η_{STH} 's up to 2.8% at AM1.5G (100 mW cm^{-2}) using Pt as the cathode. Similar to the a-Si based devices, two DSCs connected in series to the photoanode were necessary to afford overall water splitting. This was accomplished by positioning these two DSCs side-by-side behind the WO_3 photoanode.

This photoanode/2×DSC architecture does not fundamentally provide a limitation to the possible solar-to-hydrogen conversion efficiency for WO_3 or even the more promising Fe_2O_3 , as less than one third of the available solar photons have wavelength shorter than 600 nm and pan-chromatic dyes with high quantum efficiency extending past 900 nm are being developed.³⁷ However it does present a challenge to device construction as the two DSCs need to be constructed each with half of the active area of the photoanode in order to normalize the total area of the device.

Recently, the development of new dyes for the DSC has initiated work to explore alternative device architectures for optimizing light harvesting in these water splitting tandem cells. This is the subject of Chapter 3 of this thesis.

While device engineering should improve the operating current density using the current materials by reducing reflection, scattering and resistive losses, new dyes capable of high quantum efficiencies in the far-red and infrared part of the spectra

and DSCs with higher U_{oc} 's are needed for these systems. In addition, the improvement of the photocurrent and especially the onset potential of the hematite photoanode as well as the development of high voltage DSCs are needed to fully realize the potential of a true D4 hematite/DSC water splitting tandem cell. Chapter 4 of this thesis is the first demonstration of such a tandem cell.

2.4 Photoanode/photocathode systems

As mentioned above, the most straightforward and simple way to construct a D4 tandem water splitting cell is to use an n-type semiconductor photoanode and a p-type semiconductor cathode. However, this approach is the least developed of the water splitting systems found in the literature. The reason for this is clearly due to a lack of suitable photocathode materials for water reduction. Many materials, for example GaInP₂,³⁸ Si,^{39,40} SiC,⁴¹ WS₂,⁴² Cu(In,Ga)Se₂,⁴³ Cu₂O,⁴⁴ CuYO₂,⁴⁵ CaFe₂O₄,⁴⁶ and even p-type (Mg²⁺ doped) Fe₂O₃⁴⁷ have been investigated as water reducing p-type electrodes, but the magnitude of the photocurrent or the stability in aqueous solutions have remained limiting factors. Despite this a few efforts have been made to demonstrate D4 photoanode/photocathode tandem cells.

Early work by Nozik⁴⁸ established the general theory for combining photoanodes and photocathodes into tandem cells and introduced the n-TiO₂/p-GaP system. Ohmic contact between single crystals of n-TiO₂ and p-GaP ($E_g = 2.26$ eV) gave a tandem cell that was found to evolve both hydrogen and oxygen without an applied potential. A high internal resistance limited the conversion efficiency of the cell for H₂ evolution, which was calculated to be 0.25% at zero bias (based on a total electrode area of 1.9 cm² and 85 mW.cm⁻² of net incident simulated sunlight). An oxide layer forming on the surface of the p-GaP was the likely cause of the device instability.⁴⁹

Very little research attention was given to constructing photoanode/photocathode tandem devices for many years after this seminal demonstration. More recently, following the advances in oxide photoanode performance, additional demonstrations of photoanode/photocathode tandem devices have appeared. For example, while also known to be unstable in aqueous systems,¹⁸ GaInP₂ ($E_g = 1.83$ eV) photocathodes have been combined with either WO₃³⁸ or Fe₂O₃⁵⁰ photoanodes by Wang and Turner. Under intense white light

illumination ($>200 \text{ mW cm}^{-2}$) the $\text{WO}_3/\text{GaInP}_2$ combination produced a detectable photocurrent that rose linearly with light intensity to reach $J_{op} = 20 \text{ }\mu\text{A.cm}^{-2}$ at 1000 mW.cm^{-2} . For the case of $\text{Fe}_2\text{O}_3/\text{GaInP}_2$, negligible photocurrent was observed even at 10 sun illumination due to the mismatch of the conduction band minimum of the spray-pyrolyzed Fe_2O_3 thin film and the valence band maximum in the GaInP_2 . Employing surface dipoles to raise the conduction band⁵¹ of Fe_2O_3 may be useful for this combination of materials, which is clearly not ideal. Moreover the limited availability of indium in the earth's crust prevents the application of this material on a global scale.

A more novel p-type material made from abundant elements, CaFe_2O_4 ($E_g = 1.9 \text{ eV}$), has been paired with n- TiO_2 (in a side-by-side configuration) to give a device operating at $J_{op} = 110 \text{ }\mu\text{A.cm}^{-2}$ in 0.1 M NaOH with the light from a 500 W Xe lamp.⁵² However, the Faradaic efficiency for water splitting was found to be only 12% and Fe and Ca were detected in the electrolyte after the device test.

Nanostructuring techniques have also been employed to enhance the performance of inexpensive electrode materials for photoanode/photocathode tandem cells. Grimes and co-workers used an anodization technique to oxide Cu-Ti films and obtain p-type nanotubular (1000nm length, 65 nm pore diameter, 35 nm wall thickness) Cu-Ti-O films.⁵³ These films (on transparent F: SnO_2 substrates) were placed in tandem with nanotubular TiO_2 to give a working tandem device. A $J_{op} = 0.25 \text{ mA.cm}^{-2}$ (η_{STH} around 0.30%) under standard illumination conditions and a reasonable stability in the minutes time scale were observed (photocurrent was negligible after 5 hours). It should be noted that the TiO_2 was exposed to 1 M KOH while the Cu-Ti-O was exposed to $0.1 \text{ M Na}_2\text{HPO}_4$ and the electrolyte compartments were connected by a salt bridge. The dissimilar pH values leads to a favourable chemical bias of about 0.4 V in this case. Exposing the Cu-Ti-O to the KOH caused the rapid decay of photocurrent as the CuO was reduced to copper. Recent efforts to stabilize p-type photocathodes using overlayers deposited via atomic layer deposition may improve the performance of this and many other photocathode materials.⁵⁴

2.5 Practical device design considerations

Regardless of the nature of the combination of devices chosen to make a tandem cell for solar water splitting, consideration must be taken for how the device will be illuminated and how the evolved gases will be collected. This latter point is especially important given that the stoichiometric combination of H_2 and O_2 produced during water splitting is highly explosive when mixed. Thus effective gas separation is necessary. Fortunately, the intrinsic configuration of a water splitting tandem cell—one side for water oxidation and one side for water reduction—facilitates the separate collection of gases. A simple device has been described which uses a 2 electrolyte compartments with identical compositions separated by a glass frit or membrane for ionic equilibration and to prevent reverse water splitting reaction from occurring.⁵⁵ An idealized variation of this device is shown in Figure 2.4a. Here, gravity is the driving force for separating the bubbles of gas forming on the electrodes surface and the remaining electrolyte. However, this force is maximized when the photoelectrodes are vertical, which requires the illumination direction to be perpendicular to gravity. Without using mirrors, this illumination condition is only satisfied at sunrise or sunset. Thus additional device considerations are necessary. For example the device could simply be placed with the photoanode facing in the direction of the Earth's equator and at an angle optimized to maximize insolation while still providing sufficient buoyancy force. At large latitudes (north or south) this would allow for near optimal illumination during the whole day and while also permitting the gravity collection of the gases. Since, near the equator the illumination direction is parallel to gravity, the cells should be oriented flat with respect to the earth's surface to maximize insolation. This may lead to bubble accumulation at the surface of the bottom cell which would reduce the performance of the tandem cell by lowering the surface area of the electrode exposed to the electrolyte.

Relying on gravity to separate the evolved gases from the electrolyte requires the bubbles to reach a certain size before buoyancy forces become larger than surface forces in order to detach from the photoelectrode surface, and while the surface is covered by a bubble the area occupied is no longer active for water splitting. Thus to overcome any potential losses in the large scale implementation of the tandem cell, a trough-type flow design has been proposed (Figure 2.4b). Here two glass frits (or membranes) are used to prevent mixing of the two electrolyte compartments and the

electrolyte is pumped through the two compartments.⁵⁶ The flowing electrolyte adds an extra force to shear the bubbles off the surface, which are then carried along with the electrolyte to separating tanks where the gases are collected at ambient pressure. This type of system would allow the tandem cell to be at any angle enabling the optimum insolation at any latitude or by using solar tracking without any concern of bubbles masking the active area of either electrode.

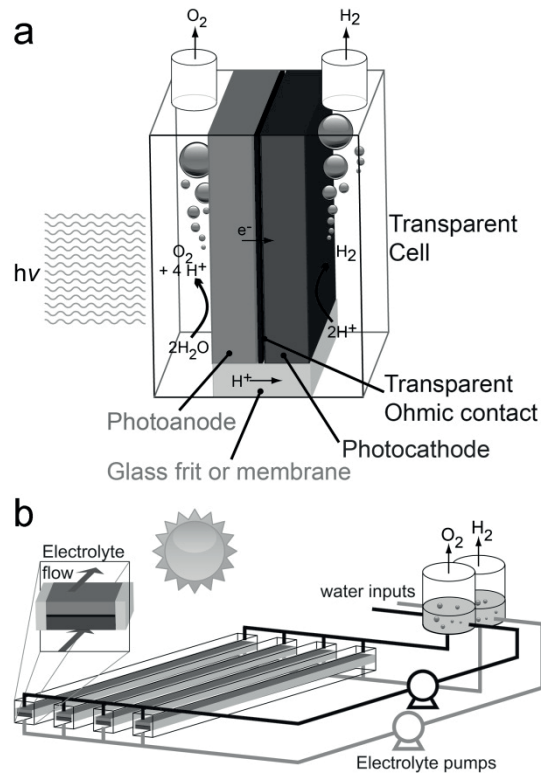


Figure 2.4 : (Top) A simple schematic of a photoanode/photocathode tandem cell with gas collection. (Bottom) Conceptual design of a large-scale reactor with integrated tandem cells and flowing electrolyte to facilitate gas collection.

In addition to these relatively simple methods of tandem cell device implementation, many other systems have been proposed for different operation scales, and even with concentrated sunlight.^{56,57} A common issue addressed in tandem cell device design is implementing separate functional layers for catalysis or protection. These, of course, would increase the cost of the system, but are currently necessary, as a total overall tandem device system that offers high performance together with stability has not yet been identified. The potential cost of producing the tandem device and its longevity are indeed equally important to its overall solar-to-hydrogen efficiency. It has been estimated that a device lifetime of 10 years, a cost of

US\$100.m⁻², and a $\eta_{STH} = 10\%$ are necessary to produce hydrogen by PEC means at a cost comparable to that of steam reforming of methanol (H₂ at a price of about \$5.kg⁻¹).⁵⁸ Thus reducing device complexity and employing inexpensive fabrication methods while employing stable materials are the main issues for the practical implementation of the solar water splitting tandem cell.

2.6 Summary and outlook

In this chapter the motivation and theoretical framework for the PEC water splitting tandem cell were examined. While a single perfect material (in an S2 scheme) could reasonably convert 10 % of the incident solar irradiation to chemical energy stored in hydrogen, that single perfect material has not been found. An integrated tandem approach (D4 scheme) could reasonably convert over 20 % of the sun's energy (even with large assumed losses) and is more flexible regarding material choice. Many different systems have been investigated using various combinations of photovoltaic cells and photoelectrodes. In order to be economically competitive with simple “brute force” strategies or the production of H₂ from fossil fuels, a practical water splitting tandem cell must optimize cost, longevity and performance. Due to the lack of stable photocathode materials, a promising approach to meet the cost and performance targets is to use a stable photoanode material in tandem with an inexpensive PV cell like the dye-sensitized solar cell. Promising photoanode materials are stable transition metal oxides exemplified by hematite (α -Fe₂O₃), which shows vast potential given its band-gap energy levels, abundance, and stability. However, much more research is needed on reducing the overpotential for the oxygen evolution reactions (by passivating surface traps and adding catalysts)^{59,60} and increasing the photocurrent (by nanostructuring)⁶¹⁻⁶³ of this and other encouraging materials. Increasing the open circuit voltage of the employed PV cell is also needed in the photoanode/DSC system. As will be seen in chapter 4, the molecular nature of the DSC allows the tuning of the dye and the redox couple to enable high voltage DSCs which could be used in a true D4 system.⁶⁴

2.7 References

1. National Research Council US Committee on Alternatives, Production, S. F. F. H., Use & National Academy of Engineering The Hydrogen Economy. (2004).
2. Kelly, N., Gibson, T. & Ouwkerk, D. A solar-powered, high-efficiency hydrogen fueling system using high-pressure electrolysis of water: Design and initial results.

- International Journal of Hydrogen Energy 33, 2747–2764 (2008).
3. Gibson, T. & Kelly, N. Optimization of solar powered hydrogen production using photovoltaic electrolysis devices. *International Journal of Hydrogen Energy* 33, 5931–5940 (2008).
 4. Dhere, N. & Jahagirdar, A. H. Photoelectrochemical water splitting for hydrogen production using combination of CIGS2 solar cell and RuO₂ photocatalyst. *Thin Solid Films* 480-481, 462–465 (2005).
 5. Jahagirdar, A. H. & Dhere, N. G. Photoelectrochemical water splitting using CuIn_{1-x}Ga_xS₂/CdS thin-film solar cells for hydrogen generation. *Sol Energ Mat Sol C* 91, 1488–1491 (2007).
 6. Vos, A. D. Detailed balance limit of the efficiency of tandem solar cells. *J Phys D Appl Phys* 13, 839–846 (2000).
 7. Cotal, H. et al. III–V multijunction solar cells for concentrating photovoltaics. *Energy & Environmental Science* 2, 174 (2009).
 8. Bolton, J. R., Strickler, S. J. & Connolly, J. S. Limiting and realizable efficiencies of solar photolysis of water. *Nature* 316, 495–500 (1985).
 9. Weber, M. & Dignam, M. Efficiency of splitting water with semiconducting photoelectrodes. *J Electrochem Soc* 131, 1258–1265 (1984).
 10. Santato, C., Ulmann, M. & Augustynski, J. Photoelectrochemical Properties of Nanostructured Tungsten Trioxide Films. *J. Phys. Chem. B* 105, 936–940 (2001).
 11. Licht, S. Multiple Band Gap Semiconductor/Electrolyte Solar Energy Conversion. *J. Phys. Chem. B* 105, 6281–6294 (2001).
 12. Khaselev, O., Bansal, A. & Turner, J. High-efficiency integrated multijunction photovoltaic/electrolysis systems for hydrogen production. *International Journal of Hydrogen Energy* 26, 127–132 (2001).
 13. Licht, S. et al. Efficient Solar Water Splitting, Exemplified by RuO₂-Catalyzed AlGaAs/Si Photoelectrolysis. *J. Phys. Chem. B* 104, 8920–8924 (2000).
 14. Licht, S. et al. Over 18% solar energy conversion to generation of hydrogen fuel; theory and experiment for efficient solar water splitting. *International Journal of Hydrogen Energy* 26, 653–659 (2001).
 15. Gao, X., Kocha, S. & Frank, A. Photoelectrochemical decomposition of water using modified monolithic tandem cells. *International Journal of Hydrogen Energy* 24, 319–325 (1999).
 16. Kocha, S., Montgomery, D., Peterson, M. & Turner, J. Photoelectrochemical decomposition of water utilizing monolithic tandem cells. *Sol Energ Mater* 52, 389–397 (1998).
 17. Khaselev, O. & Turner, J. A monolithic photovoltaic-photoelectrochemical device for hydrogen production via water splitting. *Science* 280, 425–427 (1998).
 18. Khaselev, O. & Turner, J. A. Electrochemical Stability of p - GaInP₂ in Aqueous Electrolytes Toward Photoelectrochemical Water Splitting. *J Electrochem Soc* 145, 3335–3339 (1998).
 19. Lin, G. H., Kapur, M., Kainthla, R. & Bockris, J. One step method to produce hydrogen by a triple stack amorphous silicon solar cell. *Appl Phys Lett* 55, 386–387 (1989).

20. Deng, X., Liao, X., Han, S., Povolny, H. & Agarwal, P. Amorphous silicon and silicon germanium materials for high-efficiency triple-junction solar cells. *Sol Energ Mat Sol C* 62, 89–95 (2000).
21. Rocheleau, R. & Miller, E. High-Efficiency Photoelectrochemical Hydrogen Production Using Multijunction Amorphous Silicon Photoelectrodes - Energy & Fuels (ACS Publications). *Energy & fuels* 12, 3–10 (1998).
22. Kelly, N. & Gibson, T. Design and characterization of a robust photoelectrochemical device to generate hydrogen using solar water splitting. *International Journal of Hydrogen Energy* 1658–1673 (2006).
23. Reece, S. Y. et al. Wireless solar water splitting using silicon-based semiconductors and earth-abundant catalysts. *Science* 334, 645–648 (2011).
24. Fujishima, A. & Honda, K. Electrochemical photolysis of water at a semiconductor electrode. *Nature* 238, 37–38 (1972).
25. Fujishima, A., Zhang, B. & Tryk, D. TiO₂ photocatalysis and related surface phenomena. *Surface Science Reports* 63, 515–582 (2008).
26. Neumann, B., Bogdanoff, P. & Tributsch, H. TiO₂-Protected Photoelectrochemical Tandem Cu(In,Ga)Se₂ Thin Film Membrane for Light-Induced Water Splitting and Hydrogen Evolution. *The Journal of Physical Chemistry C* 113, 20980–20989 (2009).
27. Alexander, B. D., Kulesza, P. J., Rutkowska, I., Solarska, R. & Augustynski, J. Metal oxide photoanodes for solar hydrogen production. *J Mater Chem* 18, 2298 (2008).
28. Stavrides, A., Kunrath, A., Hu, J., Treglio, R. & Feldman, A. Use of amorphous silicon tandem junction solar cells for hydrogen production in a photoelectrochemical cell. 6340, 63400K–1–8 (Proceedings of SPIE: 2006).
29. Miller, E. A hybrid multijunction photoelectrode for hydrogen production fabricated with amorphous silicon/germanium and iron oxide thin films. *International Journal of Hydrogen Energy* 29, 907–914 (2004).
30. Sivula, K., Le Formal, F. & Graetzel, M. Solar water splitting: progress using hematite (α -Fe₂O₃) photoelectrodes. *ChemSusChem* 4, 432–449 (2011).
31. O'Regan, B. C. & Graetzel, M. A low-cost, high-efficiency solar cell based on dye-sensitized colloidal TiO₂ films. *Nature* 353, 737–740 (1991).
32. Graetzel, M. Photoelectrochemical cells. *Nature* 414, 338–344 (2001).
33. Augustyński, J. & Calzaferri, G. Photoelectrochemical hydrogen production: State of the art with special reference to IEA's hydrogen programme. 3, 2379–2387 (Hydrogen Energy Progress XI, Proceedings of the World Hydrogen Energy Conference, 11th, Stuttgart, June 23-28, 1996: 1996).
34. Graetzel, M. The artificial leaf, bio-mimetic photocatalysis. *CaTTech* 3, 4–17 (1999).
35. Park, J. H. & Bard, A. Photoelectrochemical Tandem Cell with Bipolar Dye-Sensitized Electrodes for Vectorial Electron Transfer for Water Splitting. 9, E5–E8 (Electrochemical and solid-state letters: 2006).
36. Arakawa, H. et al. Solar hydrogen production by tandem cell system composed of metal oxide semiconductor film photoelectrode and dye-sensitized solar cell. *Solar Hydrogen and Nanotechnology II* 6650, 665003 (2007).
37. Nazeeruddin, M. K., Pechy, P. & Renouard, T. Engineering of efficient panchromatic sensitizers for nanocrystalline TiO₂-based solar cells. *J Am Chem Soc* 123, 1613–1624 (2001).

38. Wang, H., Deutsch, T. & Turner, J. Direct Water Splitting under Visible Light with Nanostructured Hematite and WO_3 Photoanodes and a GaInP_2 Photocathode. 155, F91–F96 (Journal of the Electrochemical Society: 2008).
39. Dominey, R. N., Lewis, N. S., Bruce, J. A., Bookbinder, D. C. & Wrighton, M. S. Improvement of photoelectrochemical hydrogen generation by surface modification of p-type silicon semiconductor photocathodes. *J Am Chem Soc* 104, 467–482 (1982).
40. Hou, Y. et al. Bioinspired molecular co-catalysts bonded to a silicon photocathode for solar hydrogen evolution. *Nat Mater* 10, 434–438 (2011).
41. van Dorp, D. H., Hijnen, N., Di Vece, M. & Kelly, J. J. SiC: A Photocathode for Water Splitting and Hydrogen Storage. *Angew. Chem. Int. Ed.* 48, 6085–6088 (2009).
42. Baglio, J. A. et al. Electrochemical characterization of p-type semiconducting tungsten disulfide photocathodes: efficient photoreduction processes at semiconductor/liquid electrolyte interfaces. *J Am Chem Soc* 105, 2246–2256 (1983).
43. Yokoyama, D. et al. Photoelectrochemical water splitting using a $\text{Cu}(\text{In,Ga})\text{Se}_2$ thin film. *Electrochemistry Communications* 12, 851–853 (2010).
44. Siripala, W., Ivanovskaya, A., Jaramillo, T. F., Baeck, S.-H. & McFarland, E. W. A $\text{Cu}_2\text{O}/\text{TiO}_2$ heterojunction thin film cathode for photoelectrocatalysis. *Sol Energ Mat Sol C* 77, 229–237 (2003).
45. Trari, M., Bouguelia, A. & Bessekhoud, Y. p-Type CuYO_2 as hydrogen photocathode. *Sol Energ Mat Sol C* 90, 190–202 (2006).
46. Matsumoto, Y., Omae, M., Sugiyama, K. & Sato, E. New photocathode materials for hydrogen evolution: calcium iron oxide (CaFe_2O_4) and strontium iron oxide ($\text{Sr}_7\text{Fe}_{10}\text{O}_{22}$). *J. Phys. Chem.* 91, 577–581 (1987).
47. Leygraf, C., Hendewerk, M. & Somorjai, G. A. The preparation and selected properties of Mg-doped p-type iron oxide as a photocathode for the photoelectrolysis of water using visible light. *J Solid State Chem* 48, 357–367 (1983).
48. Nozik, A. J. p-n photoelectrolysis cells. *Appl Phys Lett* 29, 150 (1976).
49. Ginley, D. & Chamberlain, M. Interfacial Chemistry at p - GaP Photoelectrodes. *J Electrochem Soc* 129, 2141 (1982).
50. Wang, H. & Turner, J. A. Characterization of Hematite Thin Films for Photoelectrochemical Water Splitting in a Dual Photoelectrode Device. *J Electrochem Soc* 157, F173 (2010).
51. Hu, Y.-S., Kleiman-Shwarsstein, A., Stucky, G. D. & McFarland, E. W. Improved photoelectrochemical performance of Ti-doped $\alpha\text{-Fe}_2\text{O}_3$ thin films by surface modification with fluoride. *Chem. Commun.* 2652–2654 (2009).doi:10.1039/b901135h
52. Ida, S. et al. Preparation of p-Type CaFe_2O_4 Photocathodes for Producing Hydrogen from Water. *J Am Chem Soc* 132, 17343–17345 (2010).
53. Mor, G. K. et al. P-type Cu--Ti--O nanotube arrays and their use in self-biased heterojunction photoelectrochemical diodes for hydrogen generation. *Nano Lett* 8, 1906–1911 (2008).
54. Paracchino, A., Laporte, V., Sivula, K., Graetzel, M. & Thimsen, E. Highly active oxide photocathode for photoelectrochemical water reduction. *Nat Mater* 10, 456–461 (2011).

55. Augustyński, J. & Graetzel, M. Tandem cell for water cleavage by visible light. Patent WO/2001/002,624 (2001).
56. Miller, E. Design considerations for a hybrid amorphous silicon/photoelectrochemical multijunction cell for hydrogen production. *International Journal of Hydrogen Energy* 28, 615–623 (2003).
57. Minggu, L. J., Wan Daud, W. R. & Kassim, M. B. An overview of photocells and photoreactors for photoelectrochemical water splitting. *International Journal of Hydrogen Energy* 35, 5233–5244 (2010).
58. James, B., Baum, G. & Perez, J. Technoeconomic Analysis of Photoelectrochemical (PEC) Hydrogen Production. US Department of Energy, Office of Fuel Cell Technologies, DOE Office of Energy Efficiency and Renewable Energy (2009).
59. Le Formal, F. et al. Passivating surface states on water splitting hematite photoanodes with alumina overlayers. *Chem. Sci.* 2, 737–743 (2011).
60. Zhong, D. K., Cornuz, M., Sivula, K., Graetzel, M. & Gamelin, D. R. Photo-assisted electrodeposition of cobalt–phosphate (Co–Pi) catalyst on hematite photoanodes for solar water oxidation. *Energy & Environmental Science* 4, 1759–1764 (2011).
61. Sivula, K., Le Formal, F. & Graetzel, M. WO₃-Fe₂O₃ Photoanodes for Water Splitting: A Host Scaffold, Guest Absorber Approach. *Chem Mater* 21, 2862–2867 (2009).
62. Brillet, J., Graetzel, M. & Sivula, K. Decoupling feature size and functionality in solution-processed, porous hematite electrodes for solar water splitting. *Nano Lett* 10, 4155–4160 (2010).
63. Sivula, K. et al. Photoelectrochemical Water Splitting with Mesoporous Hematite Prepared by a Solution-Based Colloidal Approach. *J Am Chem Soc* 132, 7436–7444 (2010).
64. Yella, A. et al. Porphyrin-Sensitized Solar Cells with Cobalt (II/III)-Based Redox Electrolyte Exceed 12 Percent Efficiency. *Science* 334, 629–634 (2011).

Chapter 3. Examining hematite / dye-sensitized solar-cell T6 tandem architectures

This chapter is adapted from a peer reviewed publication by Jeremie Brillet, Maurin Cornuz, Florian Le Formal, Jun-Ho Yum, Michael Graetzel, and Kevin Sivula published in 2010 in the Journal of Material Research, Vol. 25, No. 1, p.17-24.

Given the limitations of the materials available for photoelectrochemical water splitting, a multiphoton (tandem) approach is required to convert solar energy into hydrogen efficiently and durably. Here we investigate a promising system consisting of a hematite photoanode in combination with dye-sensitized solar cells with newly developed organic dyes, such as the squaraine dye, which permit new configurations of this tandem system.

3.1 State of the art, Motivations

Since the seminal demonstration of photoelectrochemical (PEC) water splitting with TiO_2 ,^{1,2} scientists and engineers have relentlessly searched for a PEC water splitting material combining efficient solar light harvesting, high quantum efficiency, practical durability, and low cost. However, no single semiconducting material has yet been found to meet all of these requirements. While systems delivering high efficiency have been demonstrated using III-V semiconductor materials with optimized band

gaps and energy levels straddling the hydrogen and oxygen redox potentials, their cost and stability are a major disadvantage.³ Oxide semiconductors such as WO_3 and Fe_2O_3 , which have reasonable band gap energies (E_g) and high stability in aqueous electrolytes, have also been thoroughly investigated as photoanodes for water splitting.^{4,5} The doping and morphology of these materials have been engineered to improve their performance, but the conduction band edge energies in these semiconducting oxides are intrinsically too low to evolve hydrogen, and an external bias must be applied to split water.⁶ To address this shortcoming, systems using more than one semiconductor have been proposed.⁷ In addition, since oxide semiconductors such as WO_3 and Fe_2O_3 do not absorb all of the incoming solar irradiation ($E_g = 2.6$ and 2.0 eV, respectively), if they are deposited on a transparent conducting substrate, a portion of the solar irradiation ($h\nu < E_g$) will not be absorbed. Transmitted photons can then be converted by another photosystem to provide the necessary potential to complete the water-splitting reaction and accomplish unassisted solar hydrogen production from water. This second photosystem is most practically a photovoltaic (PV) device as photocathode materials typically suffer from stability issues. In addition, for two-photon configurations, the upper efficiency limit for a separately illuminated photocathode-photoanode PEC is approximately 10%, while for a tandem PEC system it is more than 18%.⁷

3.2 Hematite/ $2\times$ DSC Tandem architectures

Any reasonable tandem cell system must be potentially constructed with inexpensive materials and processes to be a realistic solution to our global energy demand. Our group has previously focused research efforts on hematite ($\alpha\text{-Fe}_2\text{O}_3$) as the photoanode material. In addition to its chemical stability in aqueous environments and matchless abundance, its band gap of 2.0 eV makes hematite an ideal photoanode material capable of converting up to 16% of the incident solar energy into hydrogen in a tandem cell system.⁸ In addition, our recent efforts to tune the material properties of hematite prepared by a simple atmospheric pressure chemical vapor deposition (APCVD) method has resulted in highly nanostructured photoanodes that deliver unmatched photocurrents under standard solar conditions.⁹ Prepared on $\text{F:SnO}_2/\text{glass}$ substrates, these hematite photoanodes transmit solar photons with wavelengths longer than 600 nm to a tandem PV cell. A promising candidate for this photovoltaic device is the dye-sensitized solar cell (DSC) as these

devices can be produced for one third to one-fifth the cost of a conventional silicon solar cell¹⁰ and the absorption range can be tuned by selecting the appropriate dye.

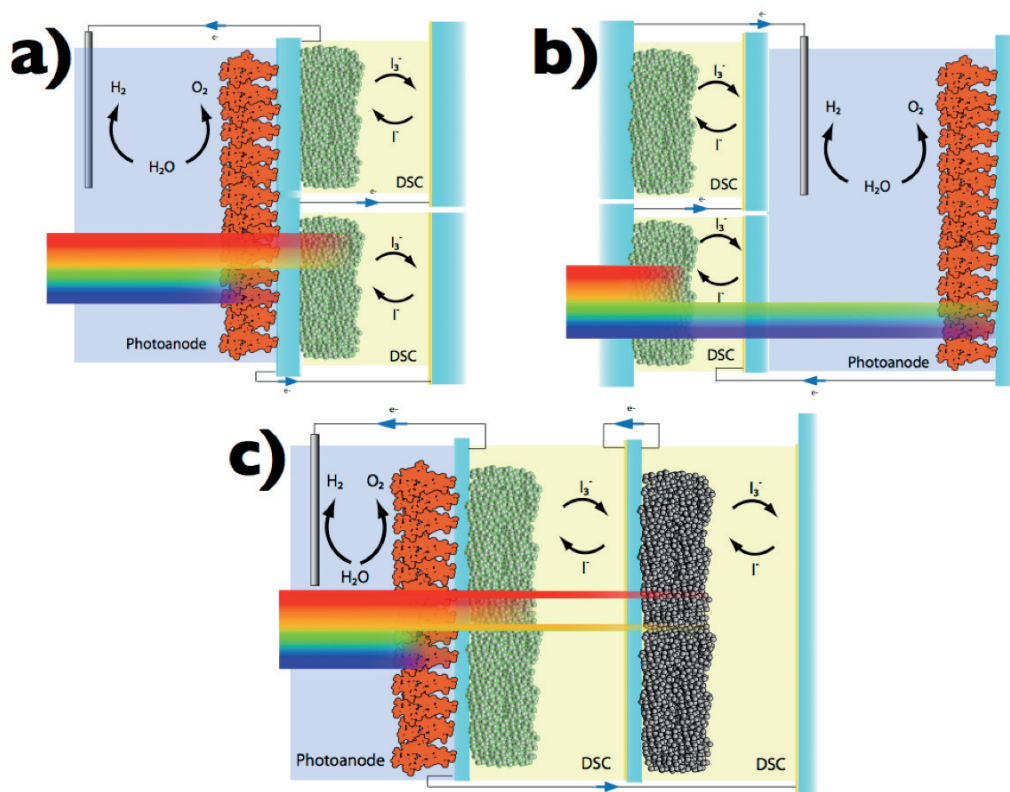


Figure 3.1 : Layout of three architectures for a tandem cell using a hematite photoanode and two dye-sensitized solar cells in series. (a) “Back DSC” configuration. (b) “Front DSC” configuration. (c) “Trilevel” configuration.

Ideally in this hematite/DSC water-splitting tandem cell, only one photovoltaic system would provide the necessary potential to complete the water-splitting reaction.¹¹ However, because of the large overpotential needed for water oxidation and other loss processes, two solar cells are needed to provide enough voltage to the current state-of-the-art Fe_2O_3 .⁹ This triple-junction photo-rectifier architecture does not fundamentally provide a limitation to the possible solar-to-hydrogen conversion efficiency, as less than one-third of the available solar photons have wave length shorter than 600 nm and panchromatic dyes with high quantum efficiency extending past 900 nm are being developed.¹² However it does present a challenge to device construction that has been addressed by placing two series-connected DSCs abreast and tandem with the photoanode as shown in Figure 3.1a.¹³ In this way the two DSCs would be constructed each with half of the active area of the photoanode to normalize the total area of the device.

Recently, the development of new dyes for the DSC opens up new possibilities

for optimizing light harvesting in these water-splitting tandem cells. All-organic dyes, such as the squaraine dye, have a narrow absorption bandwidth extending into the far red region of the visible spectrum and have demonstrated solar power conversion efficiencies up to 4.5% under AM 1.5.¹⁴ In addition to considerably reducing costs when compared with a ruthenium-based dye, two new distinct tandemcell configurations become available when using this type of dye. First we can propose a trilevel tandem device shown in Figure 3.1c. A Fe_2O_3 /DSC-squaraine dye/DSC-panchromatic dye configuration would eliminate the need to construct two DSCs side-by-side. A second possibility with the squaraine dye is to arrange two-abreast DSCs in front of a hematite photoanode as in Figure 3.1b. This “front DSC” configuration is particularly attractive in view of light harvesting as hematite has a high index of refraction that increases reflection. In addition, the front DSC approach would eliminate the need to deposit the photoanode on a transparent conducting glass and an inexpensive metal foil support could instead be used. To determine how these two new hematite/DSC tandem concepts “stack up,” here we present their investigation compared with the so-called standard “back DSC” system achieved by scrutinizing the wavelength-dependent performance after having evaluated the expected STH conversion efficiencies based on the performance of the actual devices made in our labs.

3.3 Experimental

Silicon-doped hematite photoanodes were made by atmospheric pressure chemical vapor deposition (APCVD) from $\text{Fe}(\text{CO})_5$ (Aldrich 99.999%) and tetraethoxylane (TEOS; Aldrich 99.999%) on F:SnO₂-coated glass (TEC15, Hartford Glass) at 420°C as previously reported in the literature.⁹ Their current–voltage response under global AM 1.5 simulated solar irradiation (1000 W.m⁻²) and in the dark were measured together with their incident photon conversion efficiencies (IPCEs) at different potentials in a two-electrode system (with a platinum wire cathode) to account for all overpotentials and resistances. The electrolyte was 1 M NaOH (Fluka, pro analysis in Milli-Q water, 25°C, pH = 13.6) deoxygenated by bubbling nitrogen.

A detailed methodology of fabricating and characterizing the dye-sensitized solar cell is well described in the literature. The dyes were selected to allow a broad

transparency window in the visible spectrum for the first cell and maximizing the absorption range for the second cell. A squaraine dye coded as SQ1¹⁴ and the black dye (N749)¹² were chosen based on their complementary properties over their absorption spectra. The electrolyte A6141¹⁵ was selected for its electrochemical properties allowing a high current density with low concentration and therefore high light transmission. Transparent TiO₂ layers were used (20 nm particles) to avoid light scattering. The thickness of the semiconducting layer in the squaraine-sensitized cell was carefully optimized to balance in each case between an improvement of the transmission properties and the needed photocurrent matching between the series plugged photosystems. The best result is presented in this study. The thickness of the black dye-sensitized cell was selected to match the current of the squaraine cell when the two devices are superimposed. The current–voltage responses of these devices were measured under the simulated AM 1.5G (1000 W.m⁻²). The appropriate device (hematite photoanode or/and SQ1 DSC) was used as an incident light filter according to the considered architecture. The incident photon-to-current efficiencies (IPCE) were measured under standard (short-circuit) conditions. The transmittance of each tandem cell component was measured by a Hewlett-Packard 8452A diode array ultraviolet-visible (UV-Vis) spectrophotometer.

3.4 Anticipating device performances

As suggested by Weber and Dignam⁷ the operating water-splitting current density, J_{op} , in a tandem cell is estimated by measuring the current–voltage (J-V) curves, separately, of the hematite photoanode and the two DSCs in series with the actual light incident to that separate part given its position in the particular tandem configuration, and then overlapping the J-V plots of the DSCs in series and the photoanode. Figure 3.2 illustrates the concept of finding J_{op} in the ideal case. The operating potential U_{op} is defined as the potential that should be measured at a common node between the PV and the PEC cell. Next we calculate the overall direct solar-to-hydrogen efficiency based on the amount of hydrogen produced, which is given by:

$$V = \frac{J_{op} \cdot V_m}{n \cdot F} \quad (\text{equation 3.1})$$

where V is the volume of hydrogen produced (L.s⁻¹.cm⁻²), J_{op} the operating

current density ($\text{A}\cdot\text{cm}^{-2}$) at the J-V curves intersection point, V_m is the molar volume of the gas at STP, F the Faraday constant ($96,485 \text{ C}\cdot\text{mol}^{-1}$) and n the number of electrons involved (two in this case). Here we assume all of the electrons counted in the external circuit would be involved in the water oxidation and reduction reactions; that is, no competing electrochemical reactions are occurring. This is reasonable given the stability of the hematite/base electrolyte system.

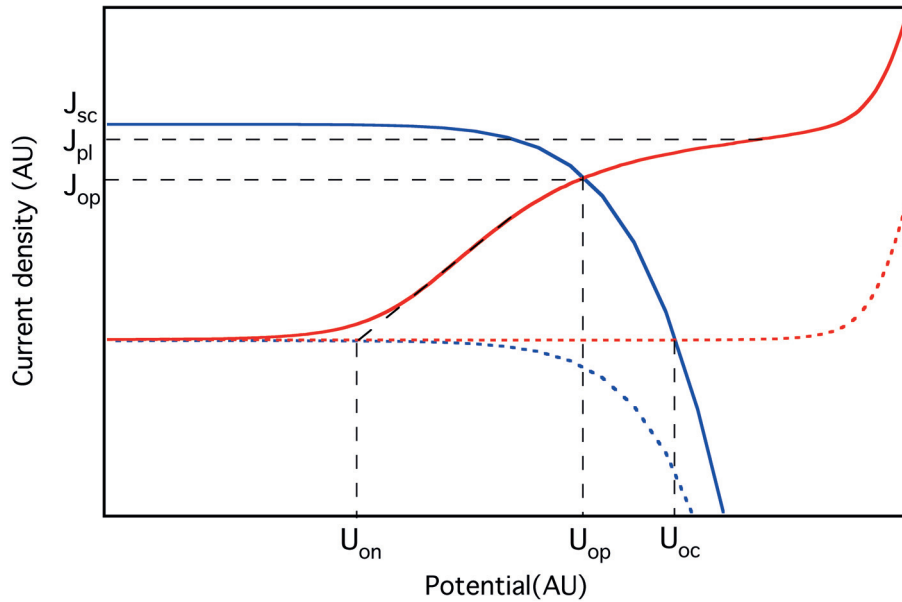


Figure 3. 2 : Current-voltage curves for a dye-sensitized solar cell (blue) on top of a hematite photoanode (red) for ideal case in the dark (broken lines) and in under illumination (solid lines). Relevant parameters of the curves are indicated and described in the text.

While the aforementioned approach gives the expected hydrogen production rate by each tandem cell, it gives little information as to the limitations of each system. To fully understand the optical limitations of each system it is judicious to look at the photon-to-current conversion efficiency of each component separately as a function of incident wave length $IPCE(\lambda)$ over the solar spectrum. Then the total current density delivered by each component can be calculated using:

$$J_V = q \cdot \int_0^{\infty} IPCE(\lambda) \cdot \Phi_{photon}(\lambda) d\lambda \quad (\text{equation 3.2})$$

where J-V is the current density at the considered potential, q is the elementary charge, and $\Phi_{photon}(\lambda)$ the incident photon flux as a function of the wave length. The last term, $\Phi_{photon}(\lambda)$, is easily calculated for each component by multiplying the measured transmittance of any filtering components (in front of the component in

question) by the global AM 1.5 solar spectral irradiation.¹⁶ The IPCE of the hematite photoanode was evaluated at the voltage of the J-V curve intersection point potential (U_{op}). The IPCE of PV and PEC devices is strongly dependent on the potential at which the photoelectrochemical cell is operating. The IPCE of the DSCs at U_{op} were therefore estimated by measuring the photocell IPCE under short-circuit conditions. We then supposed the linearity of the DSCs over illumination power along with the uniform scaling of the IPCE(λ) at different potentials¹⁷ and renormalized the

Table 3. 1 : Summary of the performance parameters for each tandem cell architecture. First the measured device properties photovoltaic short circuit current density, J_{sc} and open circuit voltage V_{oc} as well as the plateau photocurrent J_{pl} of the photoanode are given. The operating potential U_{op} , operating current J_{op} , corresponding dihydrogen evolution capacity $V(H_2)$, direct solar to hydrogen conversion efficiency % STH for each tandem architecture follow.

Architecture	J_{sc} (mA.cm⁻²)	U_{oc} (mV)	J_{pl} (mA.cm⁻²)	U_{op} (mV)	J_{op} (mA.cm⁻²)	$V(H_2 \text{ at STP})$ (mL.cm⁻².h⁻¹)	% STH
Back DSC	0.85	1420	2.67	1240	0.8	0.33	1.16
3 levels	1.59	1350	2.67	1270	0.94	0.39	1.36
Front DSC	1.06	1440	0.75	1360	0.52	0.21	0.76

IPCE to match the calculated currents, $J-V$, with the current predicted by the overlapping of the J-V curves, J_{op} , to account for the difference of the operating potential and the short-circuit measurement conditions. Finally, the IPCEs and transmittances were compared in each case to fully understand the limitations of the studied architecture and propose routes for optimization. Figures 3.3 to 3.5 summarize the principle characteristics of each configuration. Additionally, the photoanode and photovoltaic $J-V$ parameters along with the operating potential U_{op} , operating current density J_{op} , corresponding dihydrogen evolution capacity $V(H_2)$, and direct solar-to-hydrogen conversion efficiency %STH (calculated based on the upper heating value of 286 kJ.mol⁻¹ or 1.45 eV.electron⁻¹ for dihydrogen) for each tandem architecture are summarized in Table 3.1.

For the standard “back-DSC” configuration we observed an operating current density close to the short-circuit current density of the DSC (J_{op} , $J_{sc} = 0.80$, 0.85 mA.cm⁻²) but far from the plateau current of the photoanode (2.67 mA.cm⁻²). This is partly because of our choice to use the squaraine dye for this configuration to better compare with the other systems presented. While this dye, which absorbs light between 600 and 800 nm, is nominally compatible with the band gap of hematite (600

nm, see Figure 3.3, top) in practice we observe that less than 50% of the solar irradiation is transmitted through the photoanode to the DSCs at the IPCE max of 650 nm as shown in the bottom panel of Figure 3.3. This unexpected result is caused by light scattering and reflection from the photoanode and reduces the short-circuit current of the DSC by 20% over what is observed under direct solar illumination (see front DSC J_{sc}). To investigate improving the light harvesting in DSCs in this case, we determined the operating potential and current using the panchromatic black dye in the DSCs instead of the squaraine dye. In this case we found that, because of the light reflection and scattering as well as a decreasing IPCE of the black dye cells in the wavelength range of 650 to 800 nm, the J_{sc} of the solar cells only improved to 1.03 mA.cm⁻². In addition, because of the lower U_{oc} offered by the black dye cells (1.32 V) the operating potential and current both were reduced (to 1.22 V and 0.61 mA.cm⁻², respectively) actually lowering the hydrogen production expected in this configuration. As neither the squaraine DSCs nor the black dye DSCs were able to produce a short-circuit current with magnitude close to the plateau current of the photoanode in this case, we can conclude that even using dyes with tuned absorptions in the orange to far red part of the spectra, the light lost by reflection and scattering from the photoanode severely limits the performance of the standard “back DSC” architecture. However the “front DSC” configuration displayed in Figure 3.1(c) can potentially eliminate these lost photons.

When considering this “front DSC” architecture, we attempted to select parameters of cell construction to have the maximum transparency possible. We used thin TiO₂ layers made with only 20 nm particles to reduce scattering and make transparent films, a low concentration volatile electrolyte, and a dye leaving a wide transparent window in the hematite absorption region. Even with these factors, we were still able to construct squaraine dye cells with an impressive IPCE maximum of more than 70% at short-circuit conditions (not shown). Here we observe the photon-to-current conversion of the dye between 550 and 700 nm. The IPCE plot also shows a contribution from the TiO₂ at wavelengths below 400 nm. Since the hematite photoanode has low quantum efficiency between 550 and its band gap of 600 nm, and

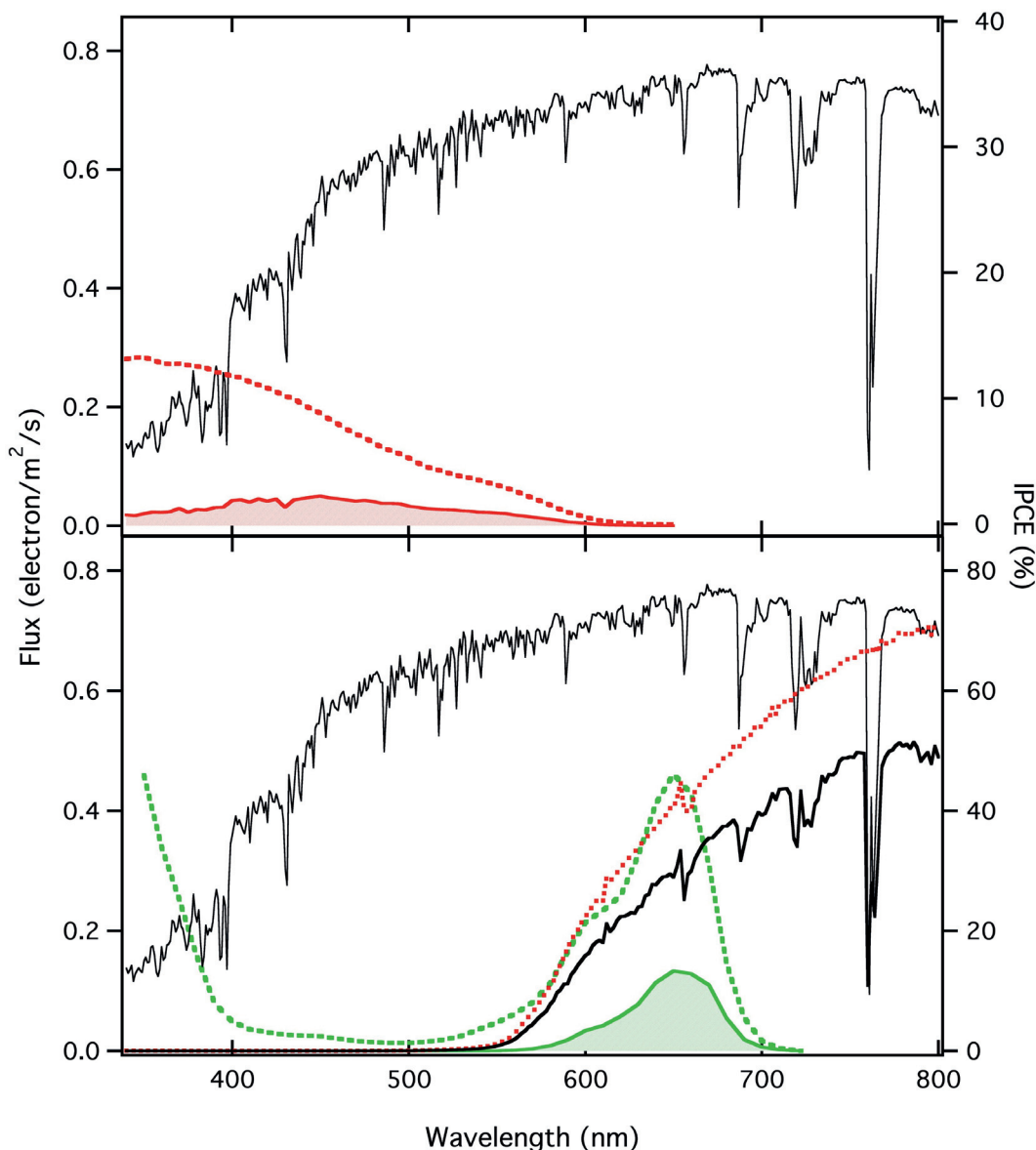


Figure 3.3 : Optical and electronic characteristics of the “back DSC” tandem cell. Top panel: Solid line shows incident solar flux. The IPCE of the hematite (red dashed line) is convoluted with the solar flux to give the electron flux in the photoanode (red shaded area). Bottom panel: The solar flux is convoluted with the transmittance of the hematite (dotted line) to give the incident irradiance on the DSC (solid bold line). The irradiance is convoluted with the IPCE of the DSC (green dashed line) to give the electron flux in the photovoltaic device (shaded area).

few solar photons are available at wavelengths below 400 nm, the squaraine dye cell seems ideally suited for the front DSC architecture. Despite this, the optical transmittance of the top component is still a limiting factor in the hydrogen production. The transmittance, presented in the bottom panel of Figure 3.4, clearly shows a strong absorption of light in the region where the iron oxide has high efficiency (400–550 nm). In addition, the short wavelength photon flux (300–400 nm) is completely absorbed by the DSC before hitting the hematite. These photons would

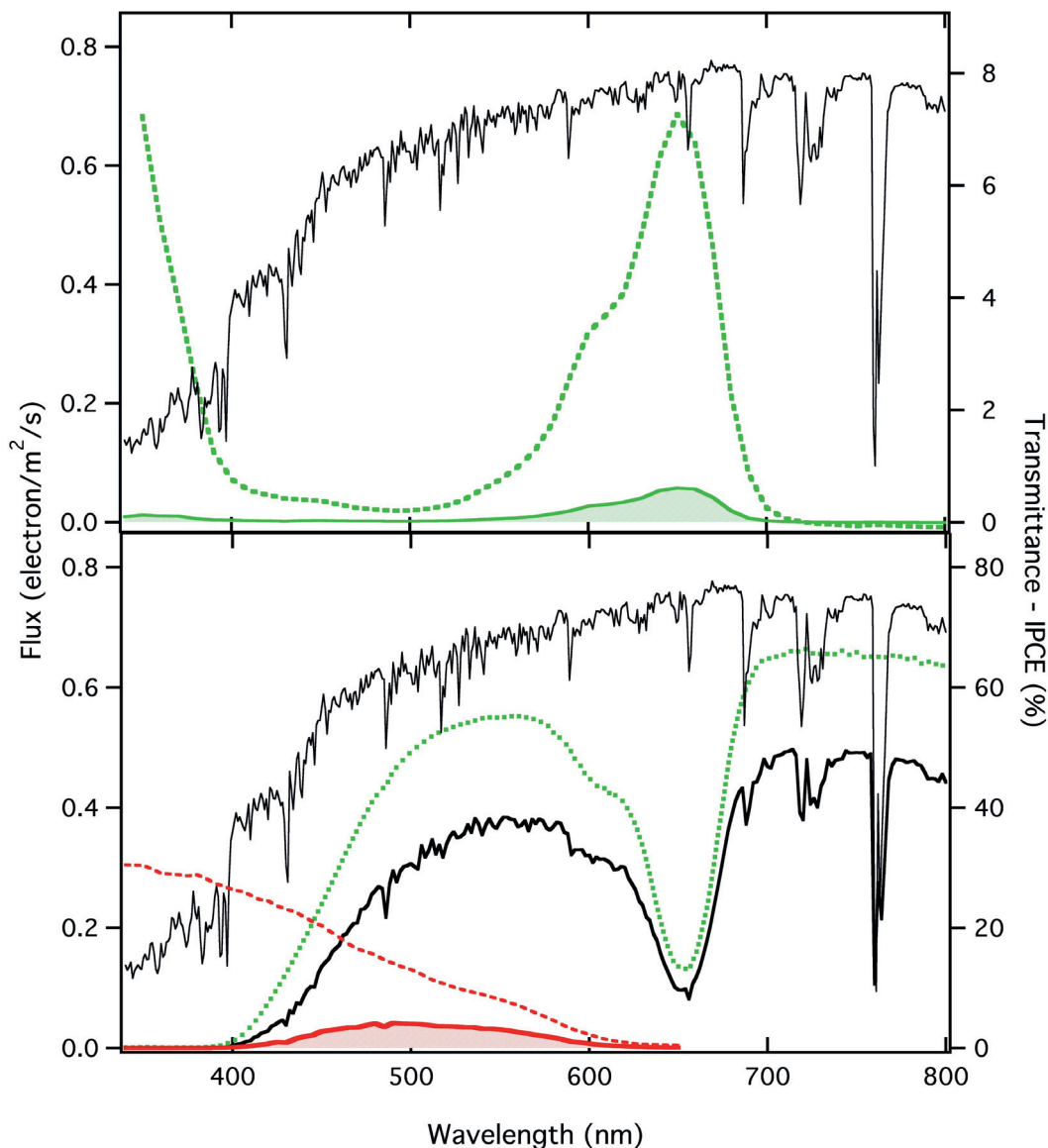


Figure 3. 4 : Optical and electronic characteristics of the “front DSC” tandem cell. Top panel: Solid line shows the incident solar flux. The IPCE of the DSC (dashed green line) is convoluted with the solar flux to give the electron flux in the DSC (shaded green area). Bottom panel: The solar flux is convoluted with the transmittance of the DSC (green dotted line) to give the incident irradiance on the hematite (solid bold black line). The irradiance is convoluted with the IPCE of the photoanode (dashed red line) to give the electron flux in hematite (shaded red area).

be converted to current very efficiently by the photoanode. The poor transmission of the squaraine DSCs is the result of both the absorption of the TiO_2 and the tri-iodine/iodide redox couple—the latter having a high extinction coefficient and undesirable absorption that peaks at 362 nm. Both of these factors cause a significant attenuation of the incident radiation to the hematite, reducing its plateau photocurrent to $0.75 \text{ mA}\cdot\text{cm}^{-2}$, and despite a higher short-circuit current and open-

circuit voltage offered by the DSCs in this case (1.06 mA.cm⁻², and 1440 mV) the operating current of the tandem cell is lower than the “back DSC” case by 35% resulting in a STH of only 0.76%. These results offer a wide avenue for improvement, which, on the dye cell side, could begin with an optimization of the choice and concentration of the redox mediator in the electrolyte to increase the transmission in the 400 to 550 nm range. Alternately, the volume of electrolyte needed could be reduced by including a porous SiO₂ layer (spheres) between the electrodes of the DSC as a spacer.¹⁸ We are actively pursuing these routes to improve the transparency as well as tuning the dye absorption to further optimize this promising configuration which, in addition to eliminating the use of a transparent substrate for the photoanode, reduces the problems of reflection and scattering by the hematite photoanode. The two above configurations both use two DSCs arranged side by side to provide enough potential to drive the hematite photoanode. Not only does this potentially complicate the device construction, by requiring a small space between the cells that reduces the active area, but to scale the devices with the same active area the current density passing through each DSC must be twice that of the hematite. Even if the light harvesting was optimized, this would be a limitation for the above architectures, given the quantum efficiencies of the dyes used, if the photoanode performed more efficiently. A trilevel tandem shown Figure 3. 1b would eliminate the current density mismatch, and each component in this inline formation would experience the same current flux under operation. As considering the “trilevel” configuration, we chose the Black dye (N749) for the bottom component given its ability to absorb and convert light in the far-red region. This DSC was optimized to absorb and convert the most light possible and to give the highest voltage, as transmission is not an issue. We also note that the SQ1 dye is well suited for application in the middle cell, and it can absorb and convert photons between that of the hematite and of the black dye. The transparent components we already optimized for the “front DSC” configuration

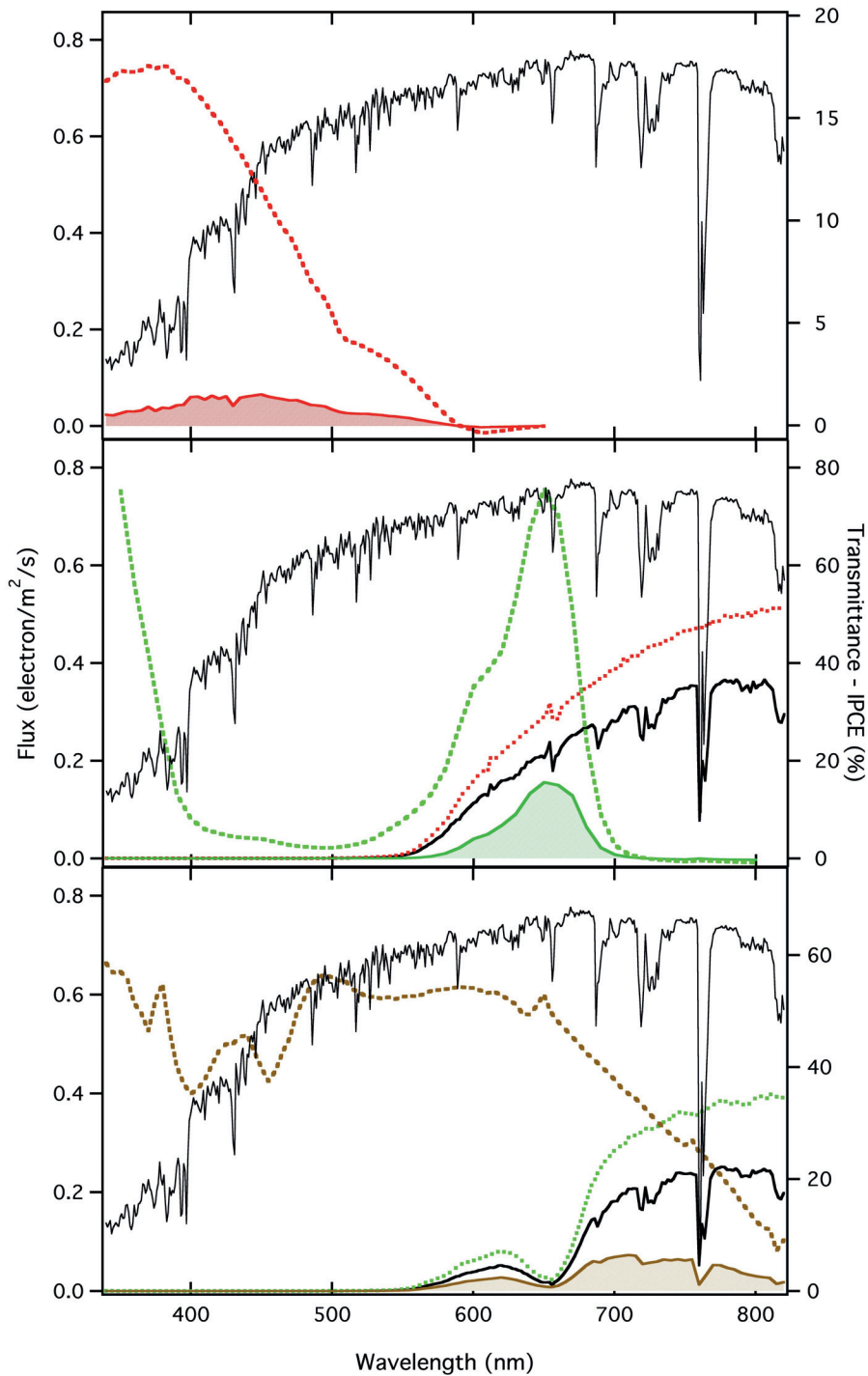


Figure 3.5 : Optical and electronic characteristics of the “trilevel” tandem cell. Top panel: Solid line shows the incident solar flux. The IPCE of the hematite (dashed red line) is convoluted with the solar flux to give the electron flux in the photoanode (shaded red area). Middle panel: The solar flux is convoluted with the transmittance of the hematite (dotted red line) to give the incident irradiance on the squaraine DSC (solid bold black line). The irradiance is convoluted with the IPCE of the squaraine DSC (dashed green line) to give the electron flux in the intermediate photovoltaic device (shaded green area). Bottom panel: The solar flux is convoluted with the transmittance of the squaraine dye plus hematite (dotted green line) to give the incident irradiance on the black DSC (solid bold black line). The irradiance is convoluted with the IPCE of the black DSC (dashed brown line) to give the electron flux in the bottom photovoltaic device (shaded brown area).

were used here, and they do indeed have absorption spectrum narrow enough to permit light conversion by the bottom cell. Looking at the complete outline of the trilevel system's light harvesting, shown in Figure. 3.5, we note that the top and middle cell have similarly shaped quantum efficiencies and transmission to the front DSC case, except with a different magnitude IPCE and integrated photon flux given the different operating point. In addition, the previous discussions of the light transmission of both the photoanode and the squaraine DSC are appropriate to describe the amount of photons reaching back cell only about one third of the available solar photons in the target region of 700 to 800 nm reach the back cell. Despite this, our analysis of this system yields the highest performance, with an operating current density, J_{op} , of 0.94 mA.cm^{-2} , and an expected STH of 1.36%. This surprising outcome is the result of the increased current density permitted by the trilevel tandem over the other configurations as discussed previously. Indeed, the short-circuit current density of the solar cells in series (and tandem in this case) is the highest at 1.59 mA.cm^{-2} . Incidentally, we also observe a small contribution to the photocurrent by solar photons not absorbed by the squaraine cell between 550 and 650 nm. Even though this system performs the best, we can consider routes for its improvement - two approaches can be considered. An increase in the IPCE of the black dye above 650 nm will raise the current in the system. This can be done for instance with the use of photonic crystals that would produce slow photons and enhance the light capture in this wavelength region.¹⁹ To further enhance the performance of the trilevel system with hematite focus must be placed on the dyes. The optimal set of band gaps for light harvesting in a trilevel tandem cell are 2.3 eV (540 nm), 1.4 eV (890 nm), and 0.8 eV (1550nm).²⁰ While the optimal band gap requirements for this hematite water splitting is convoluted with the necessity to have sufficient voltage drive the photoanodes, it is clear that the development of a far infrared dye pushing the absorption and conversion past 1000 nm is necessary. This could then replace the black dye in the bottom cell and a more broadly absorbing and high-voltage dye, like N719,²¹ could be used for the middle cell.

In general, our analysis has shown that light scattering, reflection, and unwanted component absorption are major limitations to the hematite/DSC water-splitting tandem cell system. However, since the components of our system are all constructed with similar conductive glass components, the construction of monolithic

tandem cells without concern for dissimilarity in thermal expansion is possible and would no-doubt improve the light harvesting.²² This, and the continued development of dyes with tuned absorption, especially in the infrared region are necessary to improve the light harvesting. In addition, a photoanode delivering a higher plateau current is necessary for the further development of this system. An increase in the IPCE of the hematite photoanode, especially in the near band gap region, would improve the “front DSC” case remarkably. We are currently working toward optimizing the light-harvesting and quantum efficiency of the hematite photoanodes in our laboratories. In addition to the aforementioned limitations, it is important to note that, in all three tandem cell configurations considered, the operating current density was small compared with the plateau current offered by the photoanode. While this discrepancy could be interpreted to be a result of an insufficient voltage provided by the photovoltaic devices, it is more realistically a result of the high overpotential needed for the oxygen evolution at the photoanode. Under flat band conditions the valence band holes in our hematite have an energy approximately 1 V below the O₂/H₂O redox couple in 1 M NaOH, and only 0.3 V should be needed to raise the electrons to reduce water.²³ However, we do not observe a photocurrent onset until 1 V in our two electrode hematite/Pt electrolysis cell. Since about 0.1 V can be attributed to resistive losses and the overpotential at the Pt cathode (based on three electrode measurements)⁹ we can ascribe a 0.6 V overpotential for the oxygen evolution reaction at the photoanode. This significant energy loss is the most important parameter needing optimization for these water-splitting cells. We have previously investigated reducing the photocurrent onset using an iridium oxide²⁴ or CoII catalyst,⁹ and other groups have also recently reported similar techniques.^{25,26} Further understanding of the water oxidation kinetics in this system are needed to further reduce the onset potential, ideally to a value requiring only one PV cell to drive the water splitting.

3.5 Conclusion

Through our analysis of the three possible tandem cell configurations employing hematite photoanodes and DSCs with dyes tuned to improve light harvesting for each configuration, I found that given the current state-of-the-art devices, a trilevel tandem architecture (hematite/squaraine dye/black dye), produces the highest operating current density and thus the highest expected solar-to-hydrogen

efficiency (1.36 %STH compared with 1.16 %STH which is the standard back DSC case). This is far below the expected 3.3 %STH that should be possible with the nanostructured hematite photoanodes used. Reduced light harvesting caused by scattering and reflection are limiting the efficiencies presented here, and while device engineering should improve the operating current density using the current materials, new dyes capable of high quantum efficiencies in the far-red and infrared part of the spectra are needed. In addition, the improvement of the photocurrent and especially the onset potential of the hematite photoanode are needed to fully realize the potential of the hematite water-splitting tandem cell.

3.6 References

1. Fujishima, A. & Honda, K. Electrochemical photolysis of water at a semiconductor electrode. *Nature* 238, 37–38 (1972).
2. Boddy, P. Oxygen Evolution on Semiconducting TiO₂. *J Electrochem Soc* (1968).
3. Khaselev, O. & Turner, J. A monolithic photovoltaic-photoelectrochemical device for hydrogen production via water splitting. *Science* 280, 425–427 (1998).
4. Alexander, B. D., Kulesza, P. J., Rutkowska, I., Solarska, R. & Augustynski, J. Metal oxide photoanodes for solar hydrogen production. *J Mater Chem* 18, 2298 (2008).
5. van de Krol, R., Liang, Y. & Schoonman, J. Solar hydrogen production with nanostructured metal oxides. *J Mater Chem* 18, 2311 (2008).
6. Graetzel, M. Photoelectrochemical cells. *Nature* 414, 338–344 (2001).
7. Weber, M. & Dignam, M. Efficiency of splitting water with semiconducting photoelectrodes. *J Electrochem Soc* 131, 1258–1265 (1984).
8. Murphy, A. et al. Efficiency of solar water splitting using semiconductor electrodes. *International Journal of Hydrogen Energy* 31, 1999–2017 (2006).
9. Kay, A., Cesar, I. & Graetzel, M. New Benchmark for Water Photo-oxidation by Nanostructured α -Fe₂O₃ Films. *J Am Chem Soc* 128, 15714–15721 (2006).
10. Augustyński, J. & Calzaferri, G. Photoelectrochemical hydrogen production: State of the art with special reference to IEA's hydrogen programme. 3, 2379–2387 (Hydrogen Energy Progress XI, Proceedings of the World Hydrogen Energy Conference, 11th, Stuttgart, June 23-28, 1996: 1996).
11. Duret, A. & Graetzel, M. Visible Light-Induced Water Oxidation on Mesoscopic α -Fe₂O₃ Films Made by ultrasonic spray pyrolysis. *J Phys Chem B* (2005).
12. Nazeeruddin, M. K., Pechy, P. & Renouard, T. Engineering of efficient panchromatic sensitizers for nanocrystalline TiO₂-based solar cells. *J Am Chem Soc* 123, 1613–1624 (2001).
13. Arakawa, H. et al. Solar hydrogen production by tandem cell system composed of metal oxide semiconductor film photoelectrode and dye-sensitized solar cell. *Solar Hydrogen and Nanotechnology II* 6650, 665003 (2007).
14. Yum, J.-H. et al. Efficient far red sensitization of nanocrystalline TiO₂ films by an

- unsymmetrical squaraine dye. *J Am Chem Soc* 129, 10320–10321 (2007).
15. Bessho, T. et al. New paradigm in molecular engineering of sensitizers for solar cell applications. *J Am Chem Soc* 131, 5930–5934 (2009).
 16. Standard tables for reference solar spectral irradiances: Direct normal and hemispherical on 37_ tilted surface. G 173-03. *Annual Book of ASTM Standards* (2003).
 17. Peter, L. M. Dye-sensitized nanocrystalline solar cells. *Phys. Chem. Chem. Phys.* 9, 2630–2642 (2007).
 18. Ito, S. et al. Bifacial dye-sensitized solar cells based on an ionic liquid electrolyte. *Nat Photon* 2, 693–698 (2008).
 19. Mihi, A., Calvo, M. E., Anta, J. A. & Miguez, H. Spectral Response of Opal-Based Dye-Sensitized Solar Cells. *J Phys Chem C* 112, 13–17 (2008).
 20. Vos, A. D. Detailed balance limit of the efficiency of tandem solar cells. *J Phys D Appl Phys* 13, 839–846 (2000).
 21. Nazeeruddin, M. K., Humphry-Baker, R., Liska, P. & Graetzel, M. Investigation of Sensitizer Adsorption and the Influence of Protons on Current and Voltage of a Dye-Sensitized Nanocrystalline TiO₂ Solar Cell. *J. Phys. Chem. B* 107, 8981–8987 (2003).
 22. Dürr, M., Bamedi, A., Yasuda, A. & Nelles, G. Tandem dye-sensitized solar cell for improved power conversion efficiencies. *Appl Phys Lett* 84, 3397–3399 (2004).
 23. Cesar, I., Sivula, K., Kay, A., Zboril, R. & Graetzel, M. Influence of Feature Size, Film Thickness, and Silicon Doping on the Performance of Nanostructured Hematite Photoanodes for Solar Water Splitting. *J Phys Chem C* 113, 772–782 (2009).
 24. Tilley, S. D., Cornuz, M., Sivula, K. & Graetzel, M. Light-induced water splitting with hematite: improved nanostructure and iridium oxide catalysis. *Angew. Chem. Int. Ed.* 49, 6405–6408 (2010).
 25. Hu, Y.-S., Kleiman-Shwarsstein, A., Stucky, G. D. & Mcfarland, E. W. Improved photoelectrochemical performance of Ti-doped α -Fe₂O₃ thin films by surface modification with fluoride. *Chem. Commun.* 2652–2654 (2009).
 26. Zhong, D. K. & Gamelin, D. R. Photoelectrochemical Water Oxidation by Cobalt Catalyst (“Co–Pi”)/ α -Fe₂O₃ Composite Photoanodes: Oxygen Evolution and Resolution of a Kinetic Bottleneck. *J Am Chem Soc* 132, 4202–4207 (2010).

Chapter 4. Unassisted water splitting using a low cost dual-photosystem tandem cell

This chapter is adapted from a manuscript accepted in Nature Photonics by Jeremie Brillet, Jun-ho Yum, Maurin Cornuz, Takashi Hisatomi, Renata Solarska, Jan Augustynski, Michael Graetzel and Kevin Sivula

Given the challenges and limitations of photoelectrochemical water splitting devices using a single absorber, a tandem cell approach using two or more absorbers to both harness a significant fraction of the solar spectrum and generate enough free energy for water splitting is necessary. To reduce the complexity and cost of a device it is desirable to employ only two absorbers in a D4 (Dual absorber, 4 photons for each H₂) approach and also use inexpensive and stable materials. Here we demonstrate unassisted D4 water photoelectrolysis using a nanostructured semiconductor oxide photoanode and a dye sensitized solar cell (DSC). We leverage recent advances in both of these fields to assemble devices with a measured solar-to-hydrogen (STH) efficiency, of 3.10 %STH with a WO₃ / DSC tandem cell and 1.17 %STH using a Fe₂O₃ / DSC device. A near unity faradic efficiency is confirmed by measuring the gases evolved from a device assembly. Furthermore, complete optical analysis of the devices is further performed to understand the limitations of the current constructions, and the Fe₂O₃ / DSC device was found to offer a larger room for improvement.

4.1 Devices for water photolysis, a balance between performances and complexity

As seen in chapter 2 and 3, this obstacle of marginal solar photon collection by a large band-gap semiconductor can be addressed by using multiple semiconductors superimposed in tandem to generate sufficient free energy and optimize the fraction of solar energy collected. A dual-absorber (D4) PEC approach (generating one molecule of H₂ from 4 solar photons) can be accomplished with a tandem arrangement of a photoanode / photocathode or a photoelectrode / photovoltaic design.¹ These approaches have been estimated by Weber et al. to be reasonably capable of converting up to 18% of the power in the terrestrial solar spectrum into chemical energy stored in hydrogen.² We have seen in chapter 2 that, III-V semiconducting materials have been shown to perform as high as $\eta_{STH} = 12.4\%$ in a D4 tandem configuration under concentrated solar illumination³ but the prohibitive cost and complexity of their fabrication (using organometallic vapour-phase epitaxy)⁴ have prevented commercial application. Moreover, the stability of these D4 tandem devices in harsh conditions remains inadequate. Lower-cost strategies using triple junction amorphous silicon have been investigated as early as 1989 demonstrating a record efficiency of $\eta_{STH} = 7.8\%$ when using CoMo and NiFe_yO_x catalysts for the hydrogen evolution reaction (HER) and oxygen evolution reaction (OER) respectively⁵ and reasonable stability when shielding the device with ITO/FTO protecting layers.⁶ This T6 (three absorbers, six photons for one H₂) approach has stimulated the scientific community until now,⁷ but once again, the cost and complexity of fabrication raises the question to the feasibility of hydrogen production at reasonable costs.

Indeed a trade-off exists between the device performance and the complexity of its fabrication method. These factors must be balanced to allow the economic production of solar hydrogen.⁸ Based on the performance and cost of the above systems, it is clear that a less expensive solution is still needed.

4.2 Photoanode/DSC D4 tandem-cell

Solution processed mesoscopic-oxide semiconductor based devices offer potentially drastically lower cost and high stability. The abundance of key metal-oxide semiconductors and their robustness in aqueous environments have notoriously promoted this class of materials to among the most promising for solar water splitting.

In addition, these materials offer access to extremely simple and low cost deposition techniques such as screen-printing and doctor blading. Promising materials such as tungsten oxide (WO_3 , $E_g = 2.6$ eV) and iron oxide (hematite, Fe_2O_3 , $E_g = 2.0$ eV) have reasonable band gaps for solar energy conversion but cannot perform unassisted S_2 water splitting due to the position of the conduction band more positive than the water reduction potential. This makes them ideal for a tandem cell approach. Water cleavage by visible light is possible using a photoelectrochemical tandem cell composed of a such a metal-oxide semiconductor photoanode for oxygen evolution and a dye sensitized mesoporous photovoltaic film (i.e. a dye sensitized solar cell, DSC) to promote the photogenerated electron to an energy level suitable for hydrogen evolution.⁹ Due to the large overpotential needed for oxygen evolution, the relatively low voltage output of the DSC, and other loss mechanisms, a photoanode/DSC device has only been successfully demonstrated when two DSCs connected in series are used as was shown in the last chapter.^{10,11} The late onset potential of the photocurrent given by the nanostructured hematite photoanode as well as the low open circuit potential (V_{oc}) of the DSC were identified as being the main limiting factors in this type of devices.

Recently, the design of a new cobalt complex redox shuttle using tridentate ligands having a redox potential further to the conduction band of TiO_2 than the conventional iodine/tri-iodide redox shuttle in combination with a cyclopentadithiophene-bridged donor-acceptor dye (coded Y123) has enabled DSCs do display open circuit voltages (V_{oc}) over 1000 mV.¹² In parallel, research aiming at understanding the injection processes at the semiconductor/water interface^{13,14} and the development of oxygen evolution catalysts and trap-passivating over-layers¹⁵⁻²⁰ have allowed a great enhancement in the onset potential of the photocurrent of nanostructured oxide photoanodes. These innovations allow now the realization of a one photoanode / one single DSC tandem device.²¹

We report here reasonable solar-to-hydrogen conversion efficiencies with a D4 device employing a nanostructured metal-oxide semiconductor photoanode / DSC tandem system. The tandem cells consist of an oxygen-evolving photoanode—nanostructured Fe_2O_3 or WO_3 —electrically connected in series with the cathode of a DSC, while the photoanode of the DSC is connected to a hydrogen-evolving platinum electrode. Both devices are stacked in such a manner that the light is incident on the

photoanode before the underlying photovoltaic cell as shown in Figure 4.1.

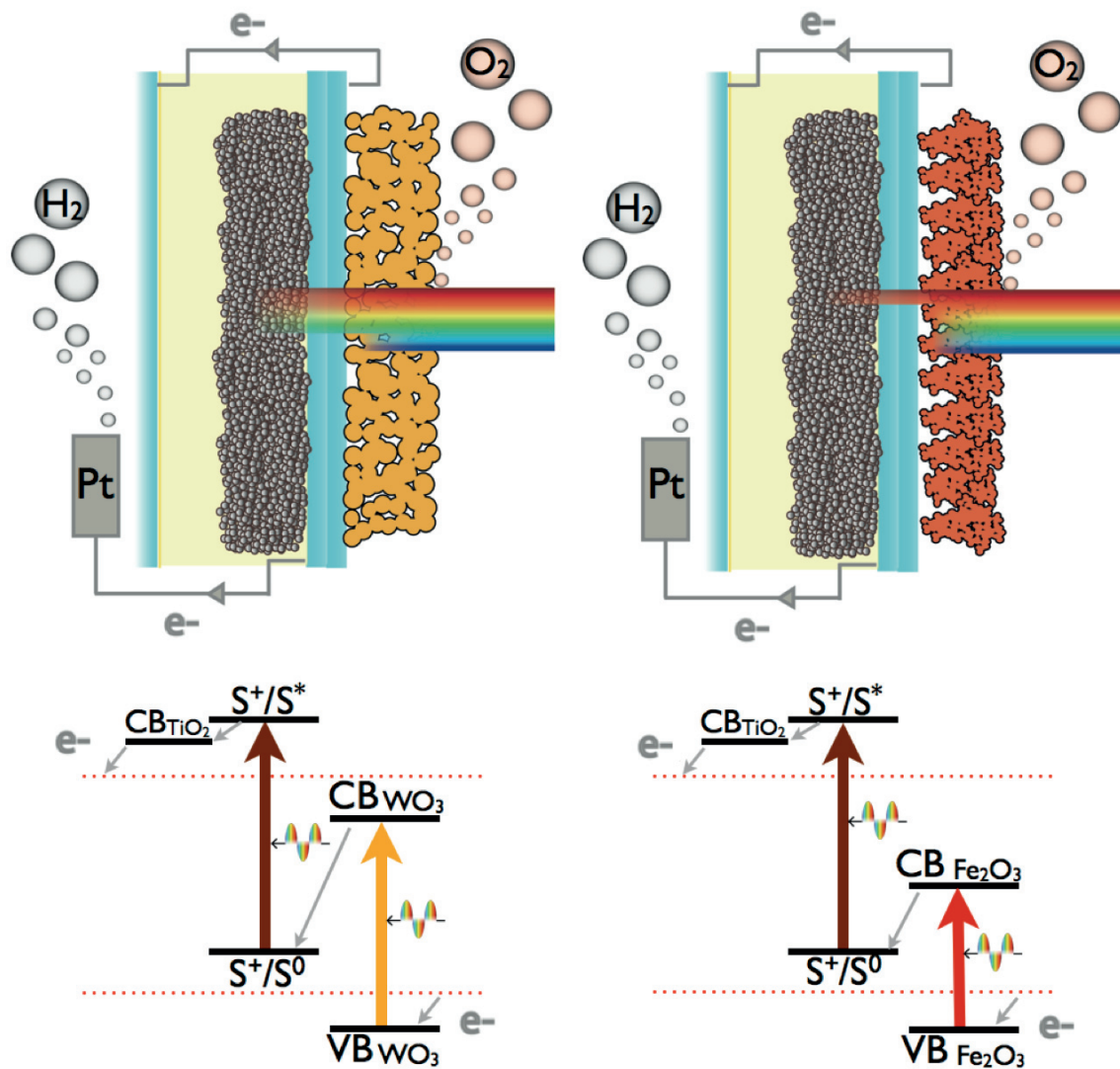


Figure 4.1 : General scheme (top) and energy diagram (bottom) of a WO₃ (left) and Fe₂O₃ (right) Photoanode / Dye-Sensitized-Solar-Cell D4 tandem cell.

4.3 Predicting device performances

As a first step in assembling the tandem devices, and in order to give insight into the electro-optical limitations and routes for improvement, the current-voltage characteristics as well as the spectral responses of the completed devices, were anticipated based on measured incident photon-to-current efficiencies (*IPCEs*), transmittances of the separate device elements and the photon flux incident to each semiconductor part.

$$J_{sc} = q \cdot \int_0^{\infty} IPCE(\lambda) \cdot \Phi_{photon}(\lambda) d\lambda \quad (\text{equation 4.1})$$

An upper-bound prediction of the current density generated (i.e. the short circuit current density, J_{sc}) by each light-absorbing element, can be calculated by integrating its electron flux obtained by multiplying the photon flux incident to the semiconductor (Φ_{photon}) by its measured *IPCE*, according to equation 4.1 where q is the elementary charge. This calculation is trivial for the oxygen evolving photoanode, as Φ_{photon} can be taken directly as the standard AM 1.5 G (1000 W.m⁻²) solar spectrum. However, for the underlying DSC, Φ_{photon} needs to be calculated by accounting for the photons absorbed or reflected by the oxygen evolving photoanode. Figure 4.2.a and 4.2.b summarize the measured *IPCEs*, transmittance of the metal oxide photoanodes as well as the photon and electron fluxes in each device composing the Fe₂O₃/DSC and the WO₃/DSC, respectively.

In both the case of the WO₃/DSC and the Fe₂O₃/DSC photoelectrochemical tandem cell, the optical transmittances and spectral responses fit well with the known band gaps of hematite and tungsten trioxide (i.e. 2.1 and 2.6 eV), respectively. The immediate comparison of Figure 4.2a and 4.2b shows the limitation of the tungsten oxide in terms of spectral response. Its large band-gap only allows absorption from the UV to the blue photons, while hematite's band-gap extends to up to the yellow wavelengths (600 nm). However, the maximum external quantum efficiency of the Fe₂O₃ photoanode is less than in the well-optimized WO₃.

Since the photoanode and DSC are connected in series the current flowing through the tandem cell must be the same for each device during operation. As such, the maximum efficiency obtainable from a tandem cell can be determined to a first approximation by the smaller of the two photocurrent densities generated by their respective parts. Based on the spectral responses of the photoanodes and the DSC, it is clear that despite the less than ideal absorption overlap of the Y123 dye and the photoanode, each absorber should be able to produce current in a reasonable quantity. The predicted values are 2.23 mA.cm⁻² / 5.22 mA.cm⁻² for the WO₃/DSC tandem cell and 1.34 mA.cm⁻² / 2.53 mA.cm⁻² for the Fe₂O₃/DSC tandem cell. This first assessment allows us to discard any major optical limitations to the operation of a tandem device and predicts the upper-bound photocurrent density of 2.23 and 1.34 mA.cm⁻² for the WO₃/DSC and the Fe₂O₃/DSC tandem cells respectively.

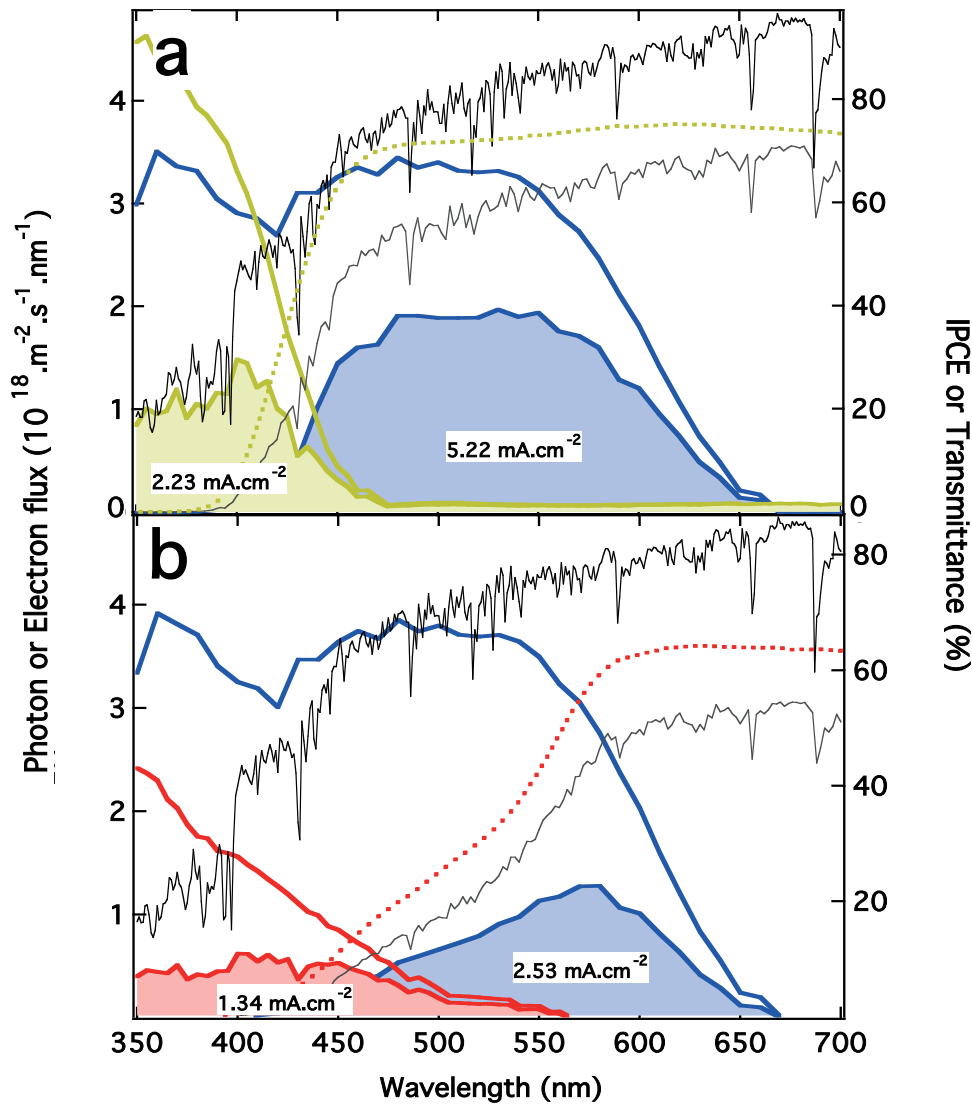


Figure 4.2: Spectral response study of the a) WO₃ (yellow) / DSC (blue) and b) Fe₂O₃ (red) / DSC (blue) tandem cells. The transmittance of the photoanode (dashed line) convoluted to the photon flux on the photoanode (black line) allows the calculation of the photon flux on the DSC (grey line). Colored areas represent the electron density calculated from the IPCE (filled line) convoluted to the photon flux on each device.

A better prediction of the actual operating photocurrent density (J_{op}) of a full tandem cell consists in determining the crossing point between the J - V curve of the DSC and that of the photoanode. A first approximation of this can be obtained by plotting together two curves: 1) the J - V curve of the photoanode measured under simulated solar illumination in a three electrode format with respect to the reversible hydrogen electrode and 2) the two electrode J - V curve of the DSC measured under 10%, 50% or 100% simulated solar illumination and then normalized so that the short circuit current density matches the value predicted in Figure 4.2. To assess the

accuracy of this approximation we next determined the operating photocurrent by measuring the J - V curves of each device separately while in the tandem configuration. The theoretical operating points, J_{op-TH} , and those measured *in situ*, J_{op-IS} , are displayed on Figure 4.3a and 4.3b.

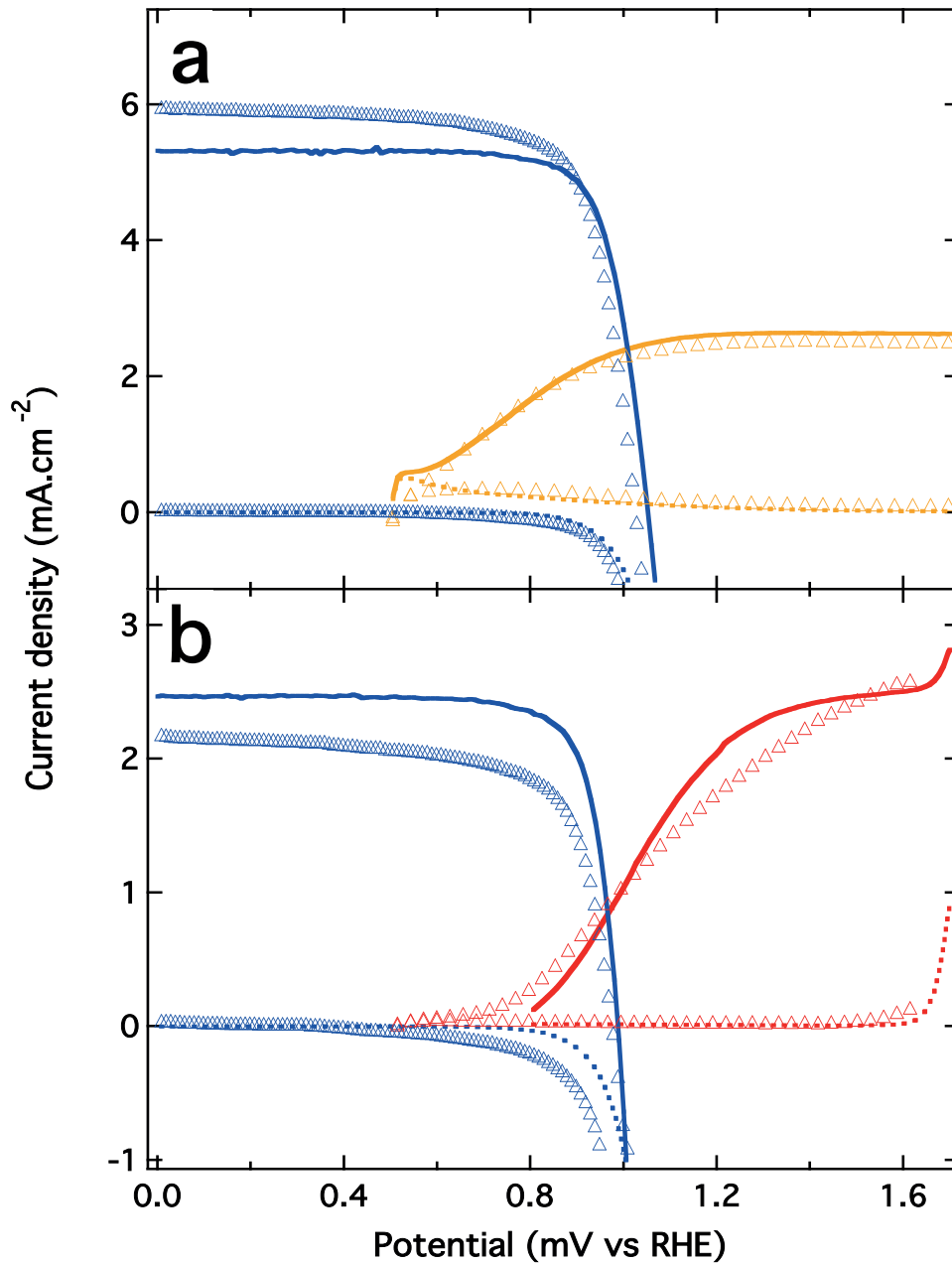


Figure 4.3 : J - V curves of a) WO_3 (yellow) / DSC (blue) and b) Fe_2O_3 (red) / DSC (blue) tandem cells under AM 1.5 G irradiation. The filled lines refer to the linear voltage sweep expected from calculation and the triangles refer to *in situ* measurements.

4.4 Measuring device performances

The predicted J - V curves fit the *in situ* measurements within 10% in both the Fe_2O_3 / DSC and the WO_3 / DSC calculations. The small discrepancy observed can be attributed to the optical losses in the measurement chamber and a mismatch between the light source and the standard solar spectrum, as further explained in Appendix B of this thesis. Nevertheless, the close agreement between the operating photocurrent density obtained from the electro-optical study and the one obtained from *in-situ* measurements validates our simplest device assessment method. Finally, to most accurately assess the performance of the tandem cells, the effective operating current density, J_{op-eff} , was measured during device operation under simulated one sun illumination by simply connecting a conventional multi-meter in series between the DSC and the photoanode. The value of J_{op-eff} confirmed J_{op-TH} within 10% of error. Table 4.1 summarizes the performances of the Fe_2O_3 /DSC and the WO_3 /DSC tandem cells obtained by different techniques and the corresponding η_{STH} calculated with (equation 4.2).²² We consider here the standard heat of combustion of H_2 and a faradic efficiency (η_{Farad}) of 100%.

$$\eta_{STH} = \frac{\left(J_{op} \left(\frac{mA}{cm^2}\right) \cdot 1.23 (V) \cdot \eta_F\right)}{P_{solar} \left(\frac{mW}{cm^2}\right)} \quad (\text{equation 4.2})$$

In the case of the Fe_2O_3 /DSC tandem cell, the crossing point is far from the plateau region of the hematite electrode photocurrent. This results in a J_{op} far from the maximum net photocurrent obtainable. The limitation of this system is clearly the late onset of the photocurrent in the photoelectrode, despite the use of state-of-the-art strategies to shift cathodically the onset of the photocurrent by means of surface catalysis and passivation. This finding by itself justifies the ongoing efforts of the research community in understanding surface mechanisms and developing innovative approaches to reduce the over potential needed to perform water oxidation. In addition, an increased resistive behavior is observed on the J - V of the hematite photoanode measured *in situ* as compared to the theoretical curve. This can be explained by the fact that the *in situ* measurement of the photoanode is performed in a two-electrode manner as compared to a three electrodes measurement for the prediction, which therefore takes in account the resistance of the electrolyte and at the platinum-electrolyte interface.

In the case of the WO_3/DSC tandem cell, the photocurrent onset is not a limitation and the crossing point is very close to the plateau region of the photoanode (approx. 1000 mV). The limiting factor in this case is the low photocurrent obtainable by the photoanode due to poor absorption capability of tungsten trioxide in the visible region of the solar spectrum. However, the clear advantage over hematite in terms of onset potential of the photocurrent of this semiconductor allows this device to be the best performing overall.

Stoichiometric oxygen and hydrogen evolution under light-driven water splitting are well known to occur with faradaic efficiencies close to unity in both WO_3 and Fe_2O_3 based systems in the appropriate electrolyte.^{18,23} However, to verify that the measured photocurrent of our tandem cells originates from water splitting and not any undesired side reactions, the gases evolving from a Fe_2O_3 photoanode connected in series with a DSC were measured by gas chromatography over a period of 10 hours. The amounts of evolved gases as a function of operation time are reported in Figure 4.4 and the inset in Figure 4.4 shows the photocurrent obtained during gas measurement. Both the current and the gas evolution are reported after a period of about one hour of stabilization. The measured amounts of H_2 and O_2 are close (within 9% and 6%, respectively) to the theoretical amounts calculated by integrating the photocurrent over time and considering a four electron process for oxygen evolution and a two electron process for hydrogen evolution. The faradic efficiency approaches 100% for both gases, confirming that the observed photocurrents can be attributed to complete water splitting.

The photocurrent of the tandem cell using a hematite photoanode measured during same period kept 80% of its initial performances as shown inset Figure 4.4. The degradation of the overall performance could be attributed to the dye-sensitized solar cell. Indeed, the experiment was made without IR filter and the resulting heat on the PV device is likely to be detrimental to the organic dye and to the electrolyte based on a volatile organic solvent. We expect possible dramatic improvement of this result when considering the DSC stabilities reported previously.²⁴

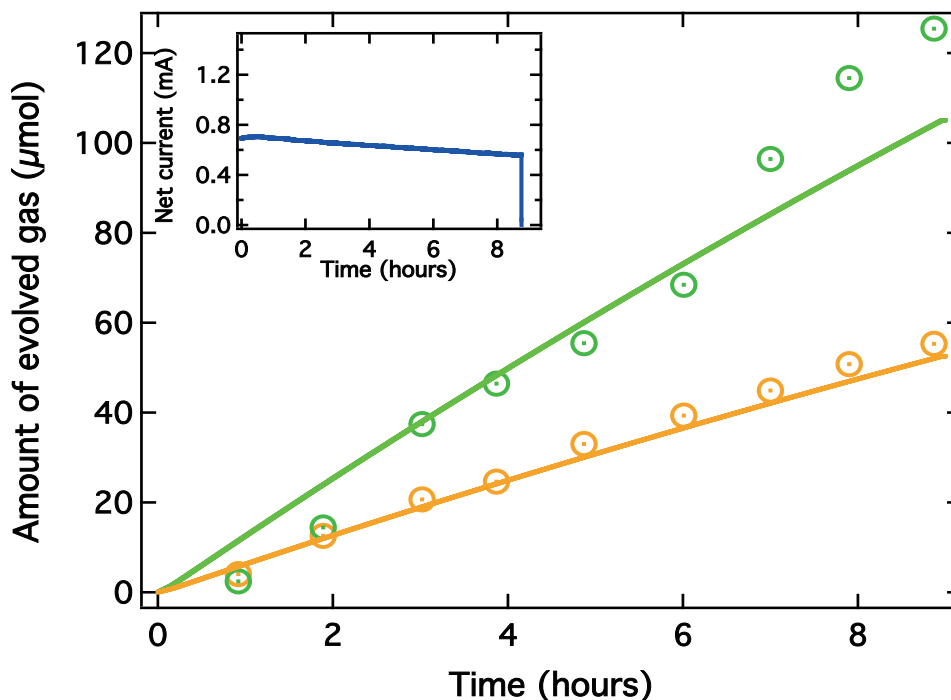


Figure 4.4: Faradic efficiency measurement of a tandem cell. Inset shows the net current measured during the experiment. The green and orange lines correspond to the integration of the net photocurrent divided by 2 and 4 respectively. The green and orange circled dots correspond respectively to H₂ and O₂ gases measured by gas chromatography during the experiment. After about nine hours, the light was turned off.

Overall our investigation of a D4 DSC/oxide-photoanode photoelectrochemical tandem cell reached promising solar to hydrogen conversion efficiency of up to $\eta_{STH} = 3.10\%$ for the WO₃/DSC and $\eta_{STH} = 1.17\%$ for the Fe₂O₃/DSC tandem cells. The lower performance of the Fe₂O₃/DSC tandem cell, despite a broader absorption than the tungsten trioxide based one, is attributed to the non-ideal charge collection from the semiconductor due to the well-known poor electron conductivity²⁵ and short hole diffusion length.²⁶ However, the performance of the WO₃/DSC device reported here is already about 50% of the maximum efficiency obtainable with this material supposing a total absorption of sub-band-gap photons and an internal quantum efficiency of 100% ($\eta_{STH, max} = 6.24\%$, with a band-gap of 2.6 eV) whereas the Fe₂O₃/DSC could possibly reach $\eta_{STH, max} = 15.36\%$ (assuming a bandgap of 2.1 eV). Efforts are being put in the research community into increasing the photocurrent obtainable from a hematite photoanode by nanostructuring^{16,27,28} and light management²⁹ strategies and reducing the onset potential of the photocurrent by surface passivation²⁰ and catalysis.¹⁶ Photocurrent densities as high as

3 mA.cm⁻² have been reported at applied potentials as low as 1.23 V *vs.* the reversible hydrogen electrode.

Table 4.1: Summary of the performances of the Fe₂O₃ / DSC and the WO₃ / DSC predicted from electro-optical study (TH), from in situ (IS) measurement and effective (eff).

	Predicted		In Situ		Effective	
	J_{op-TH} (mA.cm ⁻²)	η_{STH-TH} (%)	J_{op-IS} (mA.cm ⁻²)	η_{STH-TH} (%)	J_{op-eff} (mA.cm ⁻²)	η_{STH-TH} (%)
Fe ₂ O ₃ / DSC	0.84	1.03	0.78	0.96	0.95	1.17
WO ₃ / DSC	2.40	2.95	2.35	2.89	2.52	3.10

4.5 Conclusion

In conclusion, we demonstrated genuine D4 water splitting devices made with oxide-based semiconductors with, to our knowledge, the highest unassisted solar-to-hydrogen efficiency and stability ever reported. To accomplish this we leveraged recent advances in the photoanode and DSC performances to offer water splitting in a device which offers a dramatically simplified architecture compared to previous work. As this class of materials offers a wide range of inexpensive deposition methods we expect these simple systems could realistically allow hydrogen production at costs in agreement with market requirements. Indeed since all of the active layers can be solution processed³⁰ scalable roll-to-roll fabrication is possible. The WO₃/DSC tandem device reached about 50% of its theoretical maximum efficiency whereas the Fe₂O₃/DSC tandem device, with less than 8% of its maximum, offers a large room for improvement. In particular, improvement in the onset potential of the photocurrent will drastically improve the overall water splitting efficiency.

Supporting Information Available. Full experimental procedures and methods, J - V normalization and mismatch between the in-situ and measurements and calculated J - V curves are explained in the Appendix B of this thesis.

4.6 References

1. Walter, M. G. et al. Solar water splitting cells. *Chem. Rev.* 110, 6446–6473 (2010).
2. Weber, M. & Dignam, M. Efficiency of splitting water with semiconducting photoelectrodes. *J Electrochem Soc* 131, 1258–1265 (1984).
3. Khaselev, O. & Turner, J. A monolithic photovoltaic-photoelectrochemical device for hydrogen production via water splitting. *Science* 280, 425–427 (1998).
4. Gao, X., Kocha, S. & Frank, A. Photoelectrochemical decomposition of water using modified monolithic tandem cells. *International Journal of Hydrogen Energy* 24, 319–325 (1999).
5. Rocheleau, R. & Miller, E. High-Efficiency Photoelectrochemical Hydrogen Production Using Multijunction Amorphous Silicon Photoelectrodes - *Energy & Fuels* (ACS Publications). *Energy & fuels* 12, 3–10 (1998).
6. Kelly, N. & Gibson, T. Design and characterization of a robust photoelectrochemical device to generate hydrogen using solar water splitting. *International Journal of Hydrogen Energy* 1658–1673 (2006).
7. Reece, S. Y. et al. Wireless solar water splitting using silicon-based semiconductors and earth-abundant catalysts. *Science* 334, 645–648 (2011).
8. James, B., Baum, G. & Perez, J. Technoeconomic Analysis of Photoelectrochemical (PEC) Hydrogen Production. US Department of Energy, Office of Fuel Cell Technologies, DOE Office of Energy Efficiency and Renewable Energy (2009).
9. Graetzel, M. & Augustyński, J. Patent US6936143 - Tandem cell for water cleavage by visible light. (2005).
10. Arakawa, H. et al. Solar hydrogen production by tandem cell system composed of metal oxide semiconductor film photoelectrode and dye-sensitized solar cell. *Solar Hydrogen and Nanotechnology II* 6650, 665003 (2007).
11. Brillet, J. et al. Examining architectures of photoanode-photovoltaic tandem cells for solar water splitting. *J Mater Res* 25, 17–24 (2010).
12. Yum, J.-H. et al. A cobalt complex redox shuttle for dye-sensitized solar cells with high open-circuit potentials. *Nat Commun* 3, 631 (2012).
13. Valdés, A. & Kroes, G. J. First principles study of the photo-oxidation of water on tungsten trioxide (WO₃). *J. Chem. Phys.* 130, 114701 (2009).
14. Pendlebury, S. R. et al. Dynamics of photogenerated holes in nanocrystalline α -Fe₂O₃ electrodes for water oxidation probed by transient absorption spectroscopy. *Chem. Commun.* 47, 716–718 (2011).
15. Kanan, M. W. & Nocera, D. G. In situ formation of an oxygen-evolving catalyst in neutral water containing phosphate and Co²⁺. *Science* 321, 1072–1075 (2008).
16. Tilley, S. D., Cornuz, M., Sivula, K. & Graetzel, M. Light-induced water splitting with hematite: improved nanostructure and iridium oxide catalysis. *Angew. Chem. Int. Ed.* 49, 6405–6408 (2010).
17. Zhong, D. K. & Gamelin, D. R. Photoelectrochemical Water Oxidation by Cobalt Catalyst (“Co–Pi”)/ α -Fe₂O₃ Composite Photoanodes: Oxygen Evolution and Resolution of a Kinetic Bottleneck. *J Am Chem Soc* 132, 4202–4207 (2010).
18. Hisatomi, T. et al. Cathodic shift in onset potential of solar oxygen evolution on hematite by 13-group oxide overlayers. *Energy & Environmental Science* 4, 2512

- (2011).
19. Hisatomi, T. et al. A Ga_2O_3 underlayer as an isomorphic template for ultrathin hematite films toward efficient photoelectrochemical water splitting. *Faraday Discuss.* 155, 223 (2012).
 20. Le Formal, F. et al. Passivating surface states on water splitting hematite photoanodes with alumina overlayers. *Chem. Sci.* 2, 737–743 (2011).
 21. Solarska, R., Jurczakowski, R. & Augustynski, J. A highly stable, efficient visible-light driven water photoelectrolysis system using a nanocrystalline WO_3 photoanode and a methane sulfonic acid electrolyte. *Nanoscale* 4, 1553–1556 (2012).
 22. Chen, Z., Jaramillo, T. & Deutsch, T. Accelerating materials development for photoelectrochemical hydrogen production: Standards for methods, definitions, and reporting protocols. *J Mater Res* 25, 3–16 (2010).
 23. Mi, Q., Zhanaidarova, A., Brunshwig, B. S., Gray, H. B. & Lewis, N. S. A quantitative assessment of the competition between water and anion oxidation at WO_3 photoanodes in acidic aqueous electrolytes. *Energy & Environmental Science* 5, 5694–5700 (2012).
 24. Wang, P. et al. A stable quasi-solid-state dye-sensitized solar cell with an amphiphilic ruthenium sensitizer and polymer gel electrolyte. *Nat Mater* 2, 402–407 (2003).
 25. Guskos, N., Papadopoulos, G. & Likodimos, V. Photoacoustic, EPR and electrical conductivity investigations of three synthetic mineral pigments: hematite, goethite and magnetite. *Materials Research Bulletin* 37, 1051–1061 (2002).
 26. Kennedy, J. & Frese, K., Jr Photooxidation of Water at $\alpha\text{-Fe}_2\text{O}_3$ Electrodes. *J Electrochem Soc* 125, 709 (1978).
 27. Kay, A., Cesar, I. & Graetzel, M. New Benchmark for Water Photo-oxidation by Nanostructured $\alpha\text{-Fe}_2\text{O}_3$ Films. *J Am Chem Soc* 128, 15714–15721 (2006).
 28. Cornuz, M. & Graetzel, M. Preferential Orientation in Hematite Films for Solar Hydrogen Production via Water Splitting. *Chem Vapor Depos* 16, 291–295 (2010).
 29. Thimsen, E., Le Formal, F., Graetzel, M. & Warren, S. C. Influence of Plasmonic Au Nanoparticles on the Photoactivity of Fe_2O_3 Electrodes for Water Splitting. *Nano Lett* 11, 35–43 (2011).
 30. Brillet, J., Graetzel, M. & Sivula, K. Decoupling feature size and functionality in solution-processed, porous hematite electrodes for solar water splitting. *Nano Lett* 10, 4155–4160 (2010).

Part B
**Solution Based Colloidal
Hematite Photoanode for
water oxidation**

In the previous part, we have seen in details different architectures of Photoanode / Dye Sensitized Solar Cell tandem cells for photoelectrochemical water splitting. The photoanode material requirements are numerous and include in particular price and availability, appropriate band position, small bandgap for ample light absorption and chemical stability in aqueous environment.

Iron is the fourth most abundant element in the earth crust (6.3 % by weight) and has a tendency to oxidize in air to the ferrous (+2) and ferric (+3) states (rust). Hematite, the alpha phase of Fe_2O_3 , is the most thermodynamically stable phase of iron oxide and can be obtained easily from any other oxide, organometallic precursor and even metallic iron. Its bandgap of 1.9-2.2 eV¹ allowing the absorption of photons having a wavelength below around 600 nm makes it a great visible light absorber. In addition, Hematite is well known to be non-toxic. Those properties make this material an ideal candidate for solar water splitting.

However, hematite displays severe drawbacks. In particular, its poor majority carrier conductivity^{2,3} requires high doping levels to increase the ionized donor concentration and thus the electron conductivity in the crystal lattice. In addition, this

material has a relatively low absorption coefficient requiring 400-500 nm thick film to complete light absorption.^{4,5} The absorption depth of the photons can be calculated using Beer-Lambert law and ranges as high as 46 to 120 nm for photons wavelength ranging from 450 nm to 550 nm. This feature coupled to the short diffusion length ($L_d = 2-4$ nm) of minority carriers⁶ causes most photons absorbed deep into the bulk to photogenerate holes having poor probability to reach the semiconductor-electrolyte interface and therefore participate to water oxidation. The resulting low quantum efficiency, especially for longer wavelength, even when the electrode is placed under large anodic bias, brings the need of controlling the morphology of hematite photoanodes at the nanoscale. Indeed, a nanostructure with feature size approaching the carrier harvesting width - defined as the addition of the hole diffusion length L_d and the space charge layer width W - of 10 to 20 nm can ensure improved charge collection efficiency.

Numerous attempts to nanostructure hematite have animated the scientific community in the past decades and several different approaches have been demonstrated to be fairly efficient. A simple method to synthesize nanowire arrays with diameters of tenth of nanometers by controlled precipitation of Fe^{3+} has been first demonstrated by Hagfeld and co-workers^{7,8} followed by other methods to obtain similar types of morphologies, including thermal oxidation of iron foil^{9,10} and the use of anodic aluminum oxide (AAO) as a template for electrodeposited iron oxide.¹¹ Prakasam et al. further demonstrated nanostructuring by electrodeposition alone¹² and even nanotubes with 5 -6 nm thick walls could be obtained by sono-electrochemical anodization.¹³ The state of the art nanostructure was first demonstrated by Kay¹⁴ *et al.* and improved to reach the impressive 3.3 mA.cm⁻² net photocurrent.¹⁵

In this part, I focus on solution based colloidal hematite photoanodes for water oxidation. Making this film involves simple casting of a colloidal solution of 10 nm hematite nanoparticles obtained from thermal decomposition of iron pentacarbonyl on a conductive substrate. Earlier work has shown that this type of photoelectrode needs to be exposed to a functional annealing at about 800 °C to become photoactive. This effect has been attributed to the diffusion of dopant from the conductive substrate into the material.¹⁶ In Chapter 5, I report on the effect of intentional doping of such a photoanode. The functional annealing step also has a

detrimental effect on the nanostructure as the particles sinter together, resulting in an average feature size of 90 nm. In chapter 6, I demonstrate a new approach that allows the application of the functional annealing step while keeping the feature size in the order of 30 nm.

1. Kokorin, A. I. & Bahnemann, D. W. *Chemical Physics of Nanostructured Semiconductors*. (2003).
2. Horowitz, G. Capacitance-voltage measurements and flat-band potential determination on Zr-doped α -Fe₂O₃ single-crystal electrodes. *Journal of Electroanalytical Chemistry and Interfacial Electrochemistry* 159, 421–436 (1983).
3. Sanchez, C., Sieber, K. D. & Somorjai, G. A. The photoelectrochemistry of niobium doped α -Fe₂O₃. *Journal of Electroanalytical Chemistry and Interfacial Electrochemistry* 252, 269–290 (1988).
4. Itoh, K. & Bockris, J. Stacked thin-film photoelectrode using iron oxide. *J Appl Phys* 56, 874–876 (1984).
5. Itoh, K. & Bockris, J. Thin-Film Photoelectrochemistry - Iron-Oxide. *J Electrochem Soc* 131, 1266–1271 (1984).
6. Kennedy, J. & Frese, K., Jr Photooxidation of Water at α -Fe₂O₃ Electrodes. *J Electrochem Soc* 125, 709 (1978).
7. Lindgren, T. et al. Aqueous photoelectrochemistry of hematite nanorod array. *Sol Energ Mat Sol C* 71, 231–243 (2002).
8. Vayssieres, L., Beermann, N., Lindquist, S. & Hagfeldt, A. Controlled aqueous chemical growth of oriented three-dimensional crystalline nanorod arrays: Application to iron(III) oxides. *Chem Mater* 13, 233–235 (2001).
9. Fu, Y., Chen, J. & Zhang, H. Synthesis of Fe₂O₃ nanowires by oxidation of iron. *Chemical Physics Letters* 350, 491–494 (2001).
10. Wang, R., Chen, Y., Fu, Y., Zhang, H. & Kisielowski, C. Bicrystalline hematite nanowires. *J Phys Chem B* 109, 12245–12249 (2005).
11. Mao, A., Han, G. Y. & Park, J. H. Synthesis and photoelectrochemical cell properties of vertically grown α -Fe₂O₃ nanorod arrays on a gold nanorod substrate. *J Mater Chem* 20, 2247–2250 (2010).
12. Prakasam, H. E., Varghese, O. K., Paulose, M., Mor, G. K. & Grimes, C. A. Synthesis and photoelectrochemical properties of nanoporous iron (III) oxide by potentiostatic anodization. *Nanotechnology* 17, 4285–4291 (2006).
13. Mohapatra, S. K., John, S. E., Banerjee, S. & Misra, M. Water Photooxidation by Smooth and Ultrathin α -Fe₂O₃ Nanotube Arrays. *Chem Mater* 21, 3048–3055 (2009).
14. Kay, A., Cesar, I. & Graetzel, M. New Benchmark for Water Photo-oxidation by Nanostructured α -Fe₂O₃ Films. *J Am Chem Soc* 128, 15714–15721 (2006).
15. Tilley, S. D., Cornuz, M., Sivula, K. & Graetzel, M. Light-induced water splitting with hematite: improved nanostructure and iridium oxide catalysis. *Angew. Chem. Int. Ed.* 49, 6405–6408 (2010).

16. Sivula, K. et al. Photoelectrochemical Water Splitting with Mesoporous Hematite Prepared by a Solution-Based Colloidal Approach. *J Am Chem Soc* 132, 7436–7444 (2010).

Chapter 5. Controlling photo-activity of solution-processed hematite electrodes for solar water splitting

This chapter is adapted from a peer reviewed publication by Kevin Sivula, Jeremie Brillet, and Michael Grätzel published in 2010 in SPIEs journal OPTICAL ENGINEERING, Pages: 77700G-77700G-6.

Hematite is a promising material for solar energy conversion via photo-electrochemical water splitting. However, the precise control of substitutional doping and nanometer feature size is important for high photon harvesting efficiency. Doped and nanostructured hematite electrodes can be prepared by a simple solution-based colloidal approach however, a high temperature (800°C) annealing is required to activate the dopant atoms. This high-temperature annealing step also increases the particle size above the dimension necessary for high photon harvesting efficiencies. Here we investigate a strategy to control the two kinetic processes occurring during sintering (particle size increase and dopant diffusion/activation) by incorporating Ti dopant directly into the colloid solution and reducing the annealing time. We find that this strategy leads to porous, high-surface area hematite electrodes giving a solar photocurrent density of 1.1 mA.cm⁻² at 1.23 V vs. the reversible hydrogen electrode

(RHE) under standard testing conditions where only 0.56 mAcm^{-2} was observed at 1.23 V vs. RHE with our previous work. In addition, scanning electron micrographs examining the morphology of the electrodes suggests that our kinetic strategy is indeed effective and that further optimization may result in higher photocurrents.

5.1 Introduction

The poor electronic conductivity in hematite requires aggressive substitutional doping, which in turn greatly reduces the width of the space-charge layer responsible for separating a photo-generated electron from its corresponding vacancy (hole). In addition, the indirect band-gap transition in hematite results in a relatively poor absorption coefficient, especially for photons near the band edge¹. These limitations, coupled with the picosecond recombination of excited states and corresponding hole diffusion length² of only 2 – 4 nm define a need to control the nanostructure of hematite electrodes to afford a large semiconductor-liquid junction (SCLJ) while still allowing a continuous path for electrons to be collected at the substrate.

With the development of tools to analyze and control the structure and morphology of materials at the nanometer length scale, many reports of nanostructured hematite photo-anodes for solar water splitting have been recently published. In particular, impressive water splitting photocurrents of 2.2 mA.cm^{-2} and single wavelength conversion efficiencies of around 40 % (at $\lambda = 350 \text{ nm}$) at 1.23 V vs. RHE have been reported using a particle-assisted metal-organic chemical vapor deposition³. However, the scalability and cost of this approach are not ideal despite the atmospheric pressure conditions, and the cauliflower-type morphology observed places a significant portion of the hematite far from the SCLJ resulting in low conversion efficiencies at longer wavelengths⁴. Thus a more straightforward method of creating hematite photo-electrodes with the ideal morphology has been sought. An extremely simple technique to prepare hematite electrodes with the desired high surface area and continuous path for electron transport is to use a solution-based colloidal approach where nanoparticles of hematite are dispersed in a solution with an organic material (called a porogen) which can be later removed by thermal oxidation. The deposition of this colloid solution (sol) by an appropriate method (spin-coating, doctor blading) and subsequent thermal treatment gives a porous electrode with interconnected particles from sintering. This ubiquitous technique has been used with

many materials to create high surface electrodes for dye sensitized solar cells, sensors, and fuel cells. In addition, the ease and versatility of this method has made it a standard choice to produce nanostructured films with exclusively low-cost techniques. Hematite photo-anodes for solar water oxidation are no exception. Bjorksten *et al.* first reported the preparation of porous hematite electrodes by this approach in 1994.⁵ Here, Fe_2O_3 sols created by the hydrolysis of FeCl_3 were concentrated and combined with surfactant before they were doctor-bladed onto transparent conducting oxide substrates (F doped SnO_2) and sintered at 560 °C. Micron-thick, porous thin films of necked hematite were observed to have good adhesion to the substrate and a primary particle size in the 25 – 75 nm range. However the quantum efficiency (incident photon conversion efficiency, *IPCE*) of these photoanodes towards water splitting was quite low—on the order of 1 % at 400 mV vs. SCE in 0.1 M NaOH (1.36 V vs. RHE) with 400 nm incident irradiation. The limitation of this system was thought to be grain boundaries between the particles causing recombination and poor performance. This limitation was addressed by Qain *et al.* by altering the film thickness to optimize the light absorption/carrier transport issue.⁶ However no significant improvement was obtained.

Recently, our group reported a significant advance in the photo-activity of hematite films prepared by a solution-based colloidal approach.¹ Here we saw that a high temperature sintering (800 °C) activated the hematite films by allowing the diffusion and incorporation of dopant (Sn^{4+} diffusion from the substrate) into the porous films. However, the high temperature necessary caused an increase in the primary particle size from ca. 10 nm to around 100 nm due to sintering. Given the poor absorptivity in hematite compared to the hole diffusion length, the larger particle size kept the photocurrent below 1 $\text{mA}\cdot\text{cm}^{-2}$ at 1.23 V vs. RHE due an insufficient surface area to bulk ratio. Ideally, a hematite photo-anode would position all of the material within 10 – 20 nm from the electrolyte interface, contain enough hematite to absorb all of the solar light possible, and retain a continuous path for electron transport. The porous morphology afforded by the solution-based colloidal approach is ideal for this if the primary particle size is less than 40 – 50 nm. In this work we attempt to attain photoactive hematite electrodes with a smaller primary particle size by kinetically addressing the two processes occurring during the annealing process: dopant diffusion/activation and particle size growth by sintering.

5.2 Results and discussion

5.2.1 Kinetic control strategy

Since the two kinetic processes of particle size increase and dopant diffusion/activation that occur during annealing do not necessarily occur at the same rate, we were encouraged to gain control of the processes kinetically. If the diffusion/activation of the dopant occurs at a shorter time scale than the particle growth, simply optimizing the sintering time might allow a photoactive hematite electrode with a small particle size. In addition, in our previous work the dopant atoms diffused through the ca. 300 nm film from the tin oxide substrate. The time required to incorporate a sufficient concentration of dopant throughout the entire film would thus be directly related to the thickness of the film. We sought to address this by including dopants directly in the film before heat treatment by simply adding dopant atoms directly to the solution before processing.

Many different substitutional dopants have been reported to increase n-type conductivity in hematite (e.g. Ti^{4+} , Sn^{4+} , Zr^{4+} , Nb^{5+} , Mo^{6+} , Cr^{3+}).^{7,8} In order to facilitate the doping of hematite we investigated the incorporation of various transition metal organic complexes. $\text{Sn}(\text{OAc})_4$, $\text{Ti}(\text{OiPr})_4$, $\text{TiO}(\text{Acac})_2$, $\text{Ti}(\text{OtBu})_4$, $\text{Zr}(\text{Acac})_4$, $\text{Si}(\text{OAc})_4$ and $\text{SnCl}_4 \cdot 5\text{H}_2\text{O}$ exhibited a sufficient solubility in 2-propanol were screened by adding them to the Fe_2O_3 sol at various concentrations before doctor blading and sintering the films. The best photo-activity was found by using $\text{Ti}(\text{OiPr})_4$, however upon using lower sintering temperatures to attain photo-activity at lower temperatures we found no electrode (purposely doped or undoped) to have photo-activity at temperatures below 800 °C (result not shown). This is consistent with our previous observation and with studies on radioactive⁵⁵ Fe^{3+} ion diffusivity through hematite.⁹ That work revealed a significant change in the diffusion coefficient at temperatures around 800 – 900 °C. It is reasonable to assume that doping ions would also be kinetically limited to diffuse into the hematite lattice below this transition temperature. In addition other factors that require the high temperature like the relaxation of the hematite lattice to maximize the Madelung energy¹⁰ might also be important to attain photo active electrodes.

5.2.2 Water oxidation photo-current response

We were nevertheless able to significantly control the photo-activity by altering both the concentration of dopant added to the sol and changing the annealing time at 800 °C. Figure 5.1 shows the electrode current density in the dark and under simulated solar irradiation as a function of applied potential (vs. RHE) of hematite electrodes sintered at 800 °C for 2, 10 and 20 min (note the difference in ordinate scales). A control sample and three different titanium doping concentrations were used 2, 10, 20 at.% (based on Fe content).

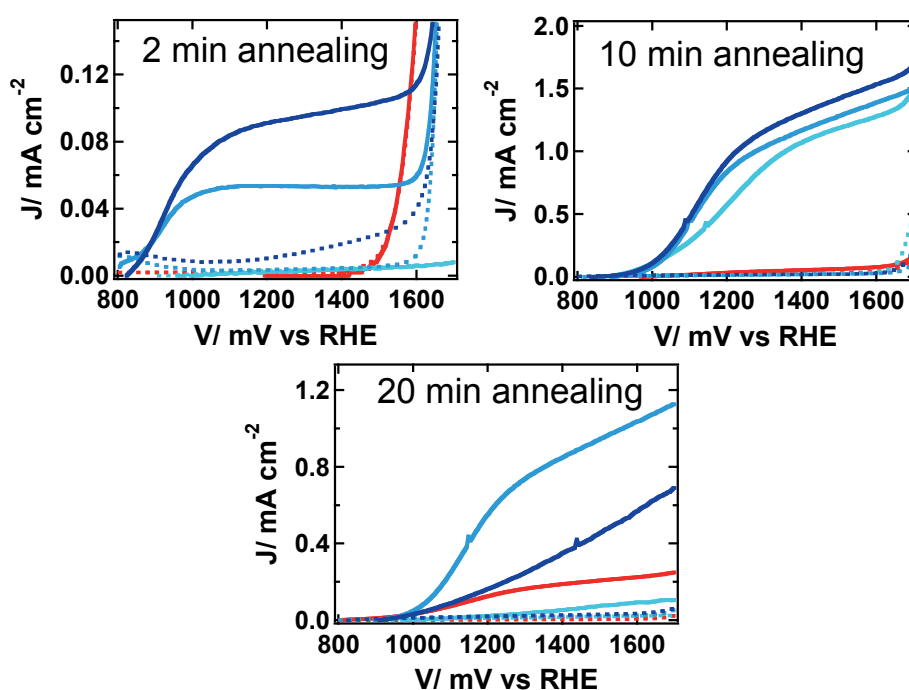


Figure 5.1 : Electrochemical current densities of the hematite electrodes versus the electrode potential in the dark (broken lines) and under simulated solar irradiation (solid lines, light source: AM 1.5G 100 mW.cm⁻², spectrally corrected). The three plots correspond to the three different annealing times. Red photo-current curves correspond to undoped control sample and the blue curves correspond to doped samples (light blue: 2 at.%, medium blue : 10 at.% and dark blue : 20 at.%). Note that the ordinate scale is different in each plot.

After 2 min at 800 °C we observed no photo-activity in the control and the electrode doped with only 2 at.% Ti (i.e. the dark current and the photo-current plots are the same). However, both the 10 and 20 at.% doped films showed significant photo-activity. Photo-current increased at ca. 900 mV vs. RHE and leveled-off at 0.05 and 0.10 mA.cm⁻² respectively, for the 10 and 20% doped samples. However, a

dark current was also observed in these electrodes. Both electrodes exhibited a dark oxidation wave at ca. 800 mV and the 20 at.% doped showed an even more pronounced dark current rising at 1100 mV. This suggests the presence of unoxidized species in the hematite film due to an insufficient annealing time.

The photo-current produced by the electrodes increased dramatically with longer annealing time, and after 10 min of annealing at 800 °C the 2, 10 and 20 at.% doped electrodes gave higher photo-current densities than reported previously for the Sn doped films. Indeed we observe a photocurrent density of 1.1 mA.cm⁻² at 1.23 V vs. RHE and up to 1.6 mA.cm⁻² before the onset of the dark current at 1.65 V with the 20 at.% doped sample. This is in stark contrast to the control electrode, which produced only minimal photocurrent after 10 min of annealing, and in the previous report where only 0.56 mA.cm⁻² was found at 1.23 V when annealing was performed for 20 min on a different SnO₂ substrate. In the current work annealing the samples for 20 min reduced the performance of the doped photo-anodes. There are three possible reasons for the reduction of photocurrent observed. First, the continued sintering of the films could increase the primary particle size and reduce the surface area. Second, for the case of the highly doped electrode (20 at.%) perhaps the full incorporation of the Ti causes a crystal phase change that disrupts charge transport or catalytic activity, and third the decomposition of the F:SnO₂ substrate resulting in the loss of conductivity according to our previous observations. Unfortunately, no one explanation can completely account for the observations here. While the over-doping is consistent with the 20 at.% sample according to the observed 11 at.% solubility of Ti in Fe₂O₃,¹¹ and no change in optical properties indicating a change in crystal structure was observed (result not shown). Next, the first explanation is consistent with the observations in the 10 at.% sample, but the drastic reduction of the photo-current in the 2 at.% sample cannot be explained without the third explanation, which seemingly does not affect the 10 at.% electrode. Why a complete explanation of the 20 min annealing results is not clear, two conclusions can be made: 20 min is beyond the optimal annealing time for the doped electrodes, but reasonable photo-activity can still be provided to the undoped electrode through Sn diffusion from the substrate verifying our previous results on a different (commercial) substrate. This latter point also suggests that the Ti(OiPr)₄ doping strategy is suitable for overcoming a kinetic competition between dopant diffusion (from the substrate) and the thermal

decomposition and conductivity loss in the substrate. Indeed we are able to confer superior photocurrents after only 10 min of annealing while 20 min was required before. However, it is not clear if this kinetic strategy is sufficient to control the particle size.

5.2.3 *Morphological effects of doping and sintering time*

To examine the effect of our doping and kinetically controlled sintering on the morphology of the electrodes we examined the films by scanning electron microscopy. The top-down micrographs of electrodes at the extremes of our parameter space of doping and annealing are shown in Figure 5.2.

First, considering the morphology of the control electrodes without added dopant as a function of annealing time, the expected large feature size after 20 min at 800 °C (Figure 5.2b) is seen in agreement with our previous results. In addition, the kinetic strategy to control the particle size is clearly effective as after only two minutes the electrode exhibits a desired smaller particle size (Figure 5.2a). The short annealing time is also sufficient to maintain a small particle size in the 20 at % doped film (Figure 5.2c) however the annealing time is clearly not sufficient to diffuse and activate the Ti dopant in the film as the observed photo-current remains low. Interestingly, the particle size of the 20 at.% doped sample after 20 min of sintering at 800 °C is significantly smaller (ca. 80 nm) compared to the control sample (ca. 120 nm). This suggests that the incorporation of the dopant retards the particle growth during sintering slightly. This observation also helps to explain the photo-current results in the 10 min annealed films, assuming that the amount of particle size retardation is directly related to the amount of dopant incorporated, as an increased photo-current is observed for increased dopant concentration. In addition, assuming the reduced performance of the 10 at.% doped sample annealed for 20 min compared to the same electrode annealed for only 10 min is due to an increase in particle size, we have shown that the kinetic control of the two processes of particle size increase and dopant diffusion/activation is possible, and improved solar water-splitting photo-currents can be obtained using this strategy. However, the precise control of the heat treatment is difficult with the short times required.

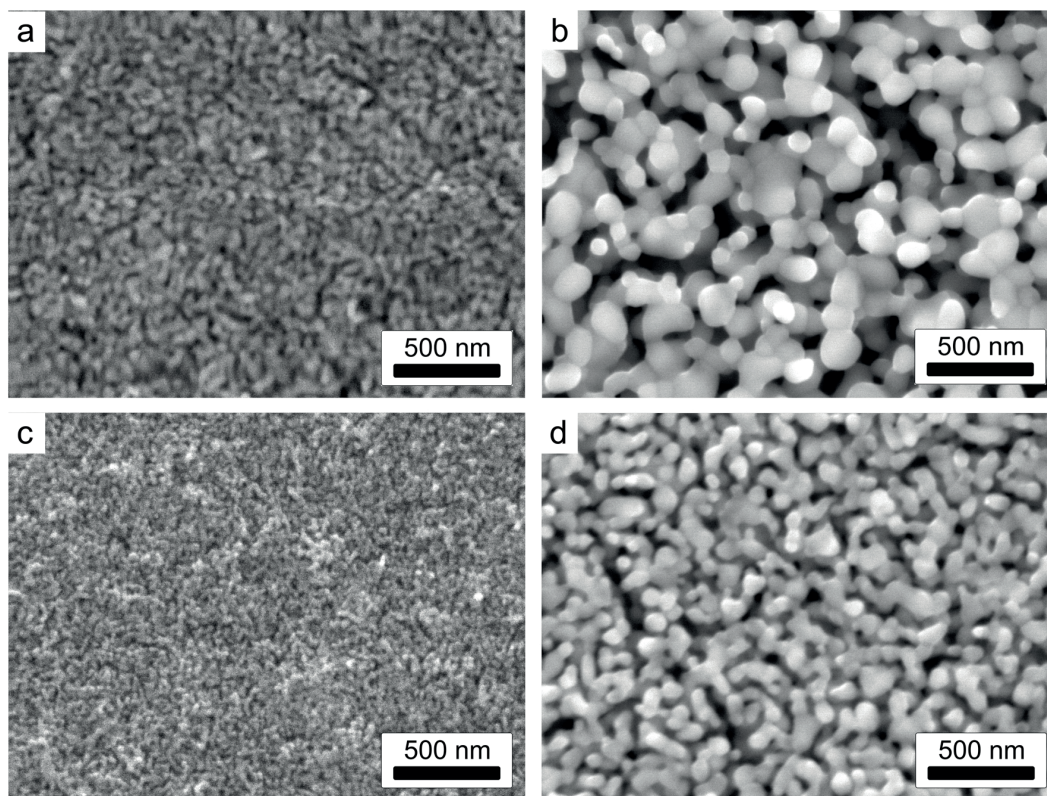


Figure 5.2: Top-down scanning electron micrographs of porous hematite photo-anodes sintered at 800 °C for 2 min (a, c) and 20 min (b,d). The top images (a,b) correspond to the control sample without dopant and the bottom images (c,d) are taken from electrodes doped with 20 at.% Ti.

5.3 Conclusions

With this work we report the largest water oxidation photo-currents at standard evaluation conditions using a hematite photo-anode prepared by a solution-based colloidal approach. By incorporating a Ti dopant directly into the Fe_2O_3 sol and annealing for a shorter time (10 min instead of 20 min) to limit particle growth by sintering we observed a photocurrent density of $1.1 \text{ mA}\cdot\text{cm}^{-2}$ at 1.23 V vs. RHE and up to $1.6 \text{ mA}\cdot\text{cm}^{-1}$ at 1.65 V where only $0.56 \text{ mA}\cdot\text{cm}^{-2}$ was observed at 1.23 V with our previous work. Electrodes annealed for only 2 min showed an even smaller particle size but were not photoactive as the dopant was not sufficiently incorporated and activated in the electrode films. Further optimization of this method may give even higher photocurrents however, a more rigorous and controllable method to control the feature size and dopant activation will be sought in Chapter 6 of this thesis.

Supporting Information Available. Full experimental procedures regarding the preparation of mesoporous thin films and methods for photoelectrochemical characterization and morphology characterization can be found in Appendix A and C of this thesis.

5.4 References

1. Sivula, K. et al. Photoelectrochemical Water Splitting with Mesoporous Hematite Prepared by a Solution-Based Colloidal Approach. *J Am Chem Soc* 132, 7436–7444 (2010).
2. Kennedy, J. & Frese, K., Jr Photooxidation of Water at α -Fe₂O₃ Electrodes. *J Electrochem Soc* 125, 709 (1978).
3. Kay, A., Cesar, I. & Graetzel, M. New Benchmark for Water Photo-oxidation by Nanostructured α -Fe₂O₃ Films. *J Am Chem Soc* 128, 15714–15721 (2006).
4. Cesar, I., Sivula, K., Kay, A., Zboril, R. & Graetzel, M. Influence of Feature Size, Film Thickness, and Silicon Doping on the Performance of Nanostructured Hematite Photoanodes for Solar Water Splitting. *J Phys Chem C* 113, 772–782 (2009).
5. Beermann, N., Vayssieres, L., Lindquist, S. & Hagfeldt, A. Photoelectrochemical studies of oriented nanorod thin films of hematite. *J Electrochem Soc* 147, 2456–2461 (2000).
6. Qian, X. et al. Photoelectrochemical characteristics of α -Fe₂O₃ nanocrystalline semiconductor thin film. *Journal of Nanoparticle Research* 2, 191–198 (2000).
7. Goodenough, J. Metallic oxides. *Progress in Solid State Chemistry* 5, 145–399 (1971).
8. Kleiman-Shwarsstein, A., Hu, Y.-S., Forman, A. J., Stucky, G. D. & McFarland, E. W. Electrodeposition of α -Fe₂O₃ Doped with Mo or Cr as Photoanodes for Photocatalytic Water Splitting.
9. Atkinson, A. & Taylor, R. Diffusion of Fe⁵⁵ in Fe₂O₃ single crystals. *J Phys Chem Solids* 4, (1984).
10. Pailhé, N., Wattiaux, A., Gaudon, M. & Demourgues, A. Impact of structural features on pigment properties of α -Fe₂O₃ hematite. *J Solid State Chem* 181, 2697–2704 (2008).
11. Berry, F., Greaves, C. & McManus, J. The Structural Characterization of Tin- and Titanium-Doped α -Fe₂O₃ Prepared by Hydrothermal Synthesis. *J Solid State Chem* (1997).

Chapter 6. Decoupling feature size and functionality in solution-processed, porous hematite electrodes for solar water splitting

This chapter is adapted from a peer-reviewed publication by Jeremie Brillet, Michael Graetzel and Kevin Sivula, published in 2010 in Nano Letters, 10 (10), pp 4155–4160.

I introduce here a simple solution-based strategy to decouple morphological and functional effects of annealing nanostructured, porous electrodes by encapsulation with a SiO₂ confinement scaffold before high temperature treatment. I demonstrate the effectiveness of this approach using porous hematite (alpha-Fe₂O₃) photo-anodes applied for the storage of solar energy via water-splitting and show that the feature size and electrode functionality due to dopant activation can be independently controlled. This allows a significant increase in water oxidation photocurrent from 1.57 mA.cm⁻² (in the control case) to 2.34 mA.cm⁻² under standard illumination conditions in 1 M NaOH electrolyte—the highest reported for a solution-processed hematite photo-anode. This increase is attributed to the improved quantum efficiency, especially with longer wavelength photons, due to a smaller particle size, which is afforded by our encapsulation strategy.

6.1 Functionality vs. Morphology conundrum

Nanocrystalline porous thin-films of various conducting or semiconducting materials prepared by solution-based colloidal routes are currently under extensive investigation as electrodes in important applications such as solar energy conversion,¹ batteries,² and sensors.³ The solution-based colloidal route offers an inexpensive path to electrodes with ultrahigh surface roughness factors to maximize interfacial charge transfer while maintaining a continuous charge transport network to the collecting substrate. Importantly, the preparation of large area electrodes using this technique is simple and amenable to roll-to-roll production. Fabrication follows a straightforward procedure: Typically, a nanoparticulate (crystalline or amorphous) colloid is first dispersed with an organic structure-directing material (the porogen). A thin film is next formed by coating the solution onto a substrate by one of various methods (e.g. doctor blading, screen printing, or spin coating). Heating then follows to remove the organic template and sinter the nanoparticles into a continuous and porous film. However, multiple processes can occur during the heating procedure. For example, the sintering and necking of nanoparticles, particle growth and coalescence, the incorporation and activation of dopant atoms, crystallization, phase changes, and the removal of defect states can all occur at different rates and at different temperatures.⁴ The convolution of these different processes can cause difficulty preparing functional nanostructures that require both specific feature size and charge carrier transport properties.

Hematite is an excellent example of a material exhibiting a convolution of processes occurring during annealing. Moreover hematite is a promising material for solar energy conversion due to its terrestrial availability, stability, and ability to absorb a significant fraction of solar irradiation. As such, hematite photo-electrodes are being studied by many groups for the storage of solar energy via photo-electrochemical water-splitting.⁵⁻¹¹ With a band-gap of 2.1 eV, a total 12.6 mA.cm⁻² of water-splitting photocurrent is possible with hematite under standard solar illumination conditions. This corresponds to a maximum possible 15 %STH conversion efficiency in a tandem cell with hematite as the water-oxidizing photo-anode.¹² However, hematite exhibits a relatively poor absorptivity of photons near its band-edge due to an indirect band gap,¹³ poor electronic conductivity requiring high concentrations of cation substitution,¹⁴ and picosecond-recombination of excited states leading to a photo-

generated hole diffusion length of only 2–4 nm.¹⁵ These non-ideal opto-electronic properties require an electrode morphology with all material 5–10 nm from the charge transfer interface (semiconductor-liquid junction, SCLJ) but still containing sufficient material to absorb all possible solar photons (equivalent to a ca. 400 nm compact film). Nanowire arrays^{6,16} or porous colloid-based films¹¹ with feature diameters of ca. 20 nm are thus highly attractive morphologies for enabling a high photon harvesting efficiency with hematite, especially if bottom-up solution-based fabrication processes are used. However, the annealing temperature required to facilitate the incorporation of substitutional dopants and obtain hematite with high water-splitting photo-activity using these solution-based methods has been shown to be around 800 °C.^{5,17} At these temperatures, the nanostructures of hematite sinter into features too large to attain high quantum efficiencies.¹⁷ Thus, the need to decouple the aspects of feature size and functionality during the annealing of hematite is apparent.

In general, kinetic methods like rapid thermal annealing have been reported to separate the relatively slow processes of particle growth from other processes occurring during heat treatment. However, rapid thermal annealing methods can be expensive, are not easily scaled, and only work in specific cases.¹⁸ Recently, researchers have addressed the trade-off between crystallinity and particle size using the so-called hard template approach where the desired material is synthesized inside the size-controlled pores of a template. The subsequent removal of the template by dissolution or etching reveals the material with a controlled feature size. This technique has already been demonstrated for the size-controlled preparation of hematite using templates of porous anodic alumina¹⁹ and mesoporous SiO₂ (KIT-6).²⁰ While the hard template approach has had much success in the preparation of individual nanocrystals and 3D-mesoporous networks of many materials, the successful application of this technique to create mesoporous networks attached to a substrate has been considered much more of a challenge, and a method to fabricate hematite electrodes with the ideal morphology as well as high photo-activity has remained elusive. However, a recently reported approach for the high temperature synthesis of TiO₂ nanoparticles dispersed in solution²¹ inspired our development of a new strategy for porous thin-film electrodes.

6.2 Decoupling by encapsulation

Porous and functional photo-anodes with controlled feature size were prepared using a solution-based encapsulation strategy schematically depicted in Figure 6.1. A hematite colloid, prepared by dispersing nanoparticles with a porogen (hydroxypropyl cellulose) in 2-propanol, was used to make the porous films. Previously, films prepared from similar solutions required an annealing temperature of 800 °C to diffuse and activate the dopants (Sn^{4+} from the substrate) and produce photo-activity.¹⁷ Here, in order to ensure the proximity of dopant atoms during the functional annealing, a Ti^{4+} source (titanium isopropoxide) was added to the colloidal solution before film deposition at a concentration of 5 at% with respect to iron

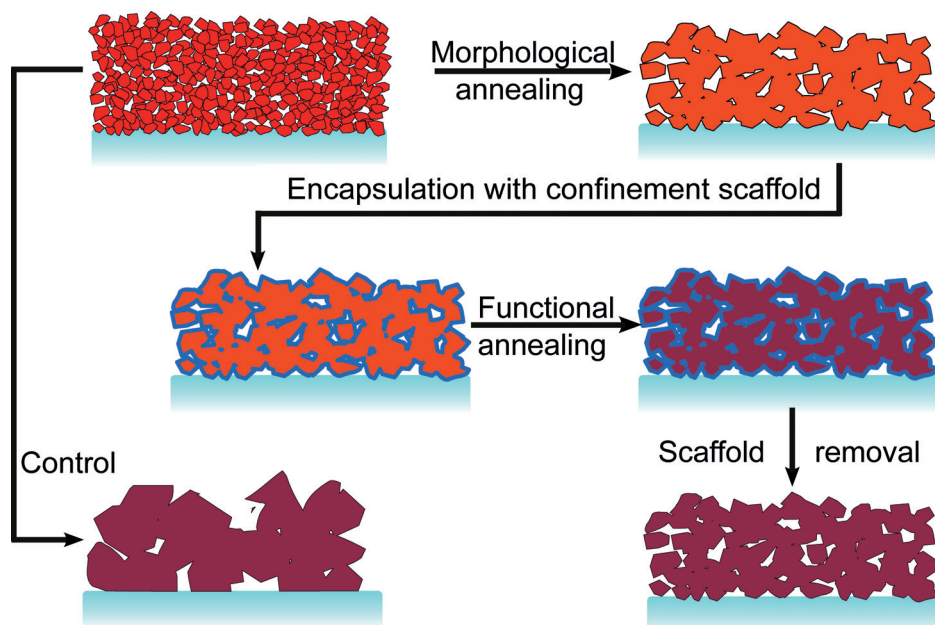


Figure 6.1 : Strategy to decouple feature size from other processes occurring during high temperature annealing. My approach is based on four steps: nanostructure formation (morphological annealing), encapsulation with a rigid scaffold, functional annealing, and finally, removal of the rigid scaffold. This process allows the obtention of a smaller feature size than a control sample only exposed to the functional annealing.

content. We found that with the addition of this dopant the minimum annealing temperature required to attain photo-activity remained 800 °C. This is consistent with a transition in cation diffusivity experimentally observed in hematite at approximately this temperature.²² After the film containing the Fe_2O_3 nanoparticles, dopant, and porogen was deposited on a heat resistant substrate ($\text{F}:\text{SnO}_2$ on alumino-boro-silicate, Solaronix) by doctor-blading, a first heat treatment (the morphological annealing) was

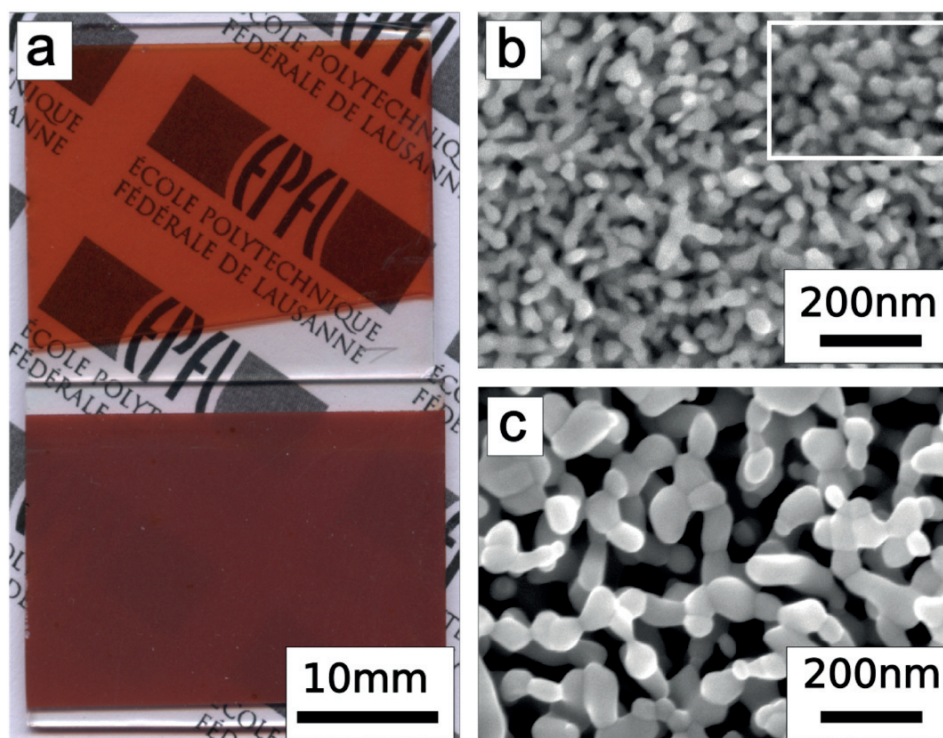


Figure 6.2 : Visual appearance (a, top corresponds to the encapsulated sample, bottom corresponds to control sample) and scanning electron micrographs of encapsulated (b) and control (c) porous hematite electrodes. The inset in (b) shows the morphology before encapsulation.

applied in order to remove the organics, sinter the particles, and thus to obtain the desired nanostructure. The best conditions were found to be $2\text{ }^{\circ}\text{C min}^{-1}$ to $500\text{ }^{\circ}\text{C}$ and a dwell time of 10 h, allowing an optimum between feature size, particle connectivity, and necking. Following cooling to room temperature, the nanostructure was then conformally coated with a thin temperature-stable layer of mesoporous silica as a confinement scaffold by immersing it in a methanol solution containing water (10.3 M), tetraethyl orthosilicate (TEOS, 77 mM) as a Si source, hexadecyltrimethylammonium chloride (C16TAC, 29 mM) as a structure directing agent, and aqueous ammonia (6.2 M) for hydrolysis following the procedure reported by Ogawa et al.²³ We chose to use a method developed under basic conditions in order to avoid the etching of Fe_2O_3 during the deposition, and we further lowered the deposition temperature to $0\text{ }^{\circ}\text{C}$ to ensure the conformal character of this coating step. The as-protected porous film was then exposed to the functional annealing ($800\text{ }^{\circ}\text{C}$ for 10 min) in order to activate the hematite. Once cooled down to room temperature, the rigid scaffold was removed by selective etching with 5 M NaOH. The deposition and later removal of the silica layer on this “encapsulated electrode” was confirmed with XPS by the presence of the Si 2s peak (binding energy 154.4 eV) and O 1s peak

(532.7 eV) attributable to SiO₂. Also, the Fe 2p peak (binding energy 710.7 eV) was significantly attenuated after SiO₂ deposition and returned to the original intensity following the selective etching (see Appendix C1). A control sample consisting of the exact same colloidal solution with porogen and Ti dopant was cast in the same way on conductive glass and only exposed to the morphological and the functional annealing steps to observe the effects of our confining strategy.

6.3 Smaller particles give higher photocurrents

The final morphology and appearance of the electrode subjected to the encapsulation procedure and the control electrode are shown in Figure 6.2. The strong effect of the encapsulation strategy on the particle size is immediately evident by eye (Figure 6.2a). The large particle size resulting from the high temperature annealing of the control film causes the scattering of unabsorbed photons and renders the film translucent with a high opacity. In stark contrast, the encapsulated electrode contains features with a size insufficiently small to scatter unabsorbed photons, and the film appears semi-transparent. The non-scattering character of the encapsulated electrode is in good agreement with the feature size observed by scanning electron microscopy (30 – 40 nm, Figure 6.2b) while the control sample (Figure 6.2c) has sintered to a significantly larger feature size (80 – 120 nm). In addition, we found that the final particle size could be controlled by changing the temperature of the morphological annealing step. Films annealed first at temperatures of 350 and 450 °C (instead of 500 °C) exhibited final feature sizes of ca. 20 and 25 nm, respectively, after the encapsulation and removal procedure (Appendix C2). Moreover, since the final size of the features in the encapsulated electrode are the same as that observed after the initial morphological annealing step (Figure 6.2b, inset), the effectiveness of our strategy to select the desired feature size while retaining the ability to anneal at high temperature is evident.

The effectiveness of the encapsulation strategy is further emphasized by the solar water-splitting capability of the electrodes. Water oxidation photocurrent versus voltage measurements were performed in 1 M NaOH electrolyte (pH 13.6) using a three-electrode cell with the Fe₂O₃ as the working electrode, a Pt counter electrode,

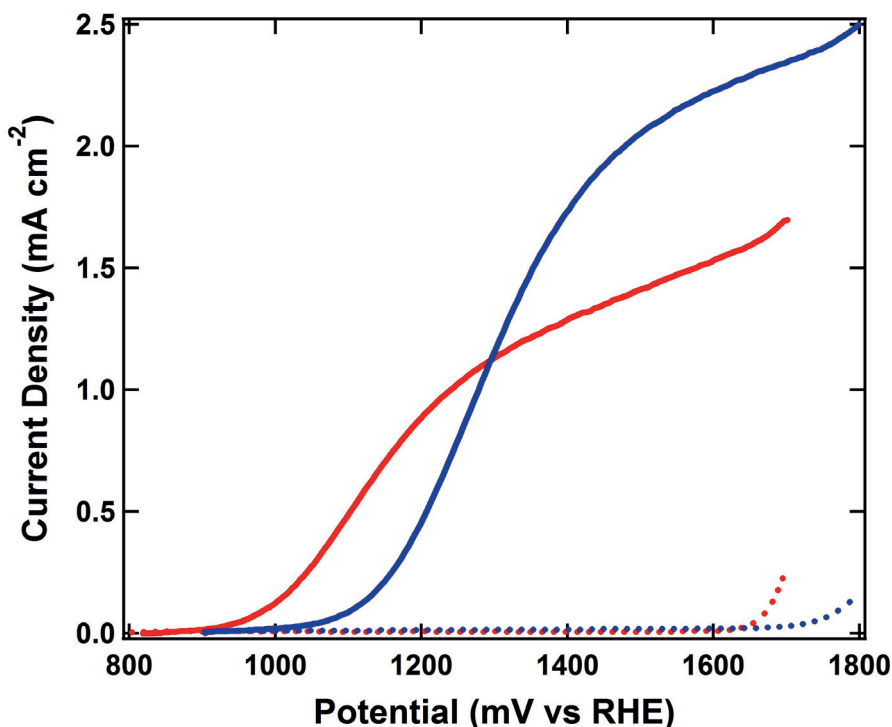


Figure 6.3 : Electrochemical water oxidation photocurrent (solid lines) and dark current (dotted lines) vs. applied voltage curves of control (red) and encapsulated (blue) photoanodes under simulated solar light (AM 1.5G 100 $\text{mW}\cdot\text{cm}^{-2}$, spectrally corrected) in 1 M NaOH electrolyte.

and an Ag/AgCl reference (reported with respect to the reversible hydrogen electrode, RHE). The current densities of the control and the encapsulated electrodes as a function of the applied voltage are shown in Figure 6.3. Upon sweeping the potential (50 mV s^{-1}) from 800 to 1700 mV vs. RHE under simulated solar illumination (AM 1.5G 100 mW cm^{-2} , spectrally corrected), the control electrode showed an onset of water oxidation photocurrent at 970 mV vs. RHE, which rose to reach $1.32 \text{ mA}\cdot\text{cm}^{-2}$ at 1430 mV vs. RHE and a maximum photocurrent of $1.57 \text{ mA}\cdot\text{cm}^{-2}$ before the onset of the dark current. It should be noted that the photocurrent observed with the control electrode here is slightly more than previously observed ($0.92 \text{ mA}\cdot\text{cm}^{-2}$ at 1430 mV vs. RHE),¹⁷ as we found the incorporated Ti dopant to slightly reduce the optimum annealing time at $800 \text{ }^\circ\text{C}$ from 20 min to 10 min and better preserve the conductivity of the F:SnO₂ substrate. This increase in photocurrent due to the Ti dopant is small compared to the enhancement found by using the confinement strategy. The water oxidation photocurrent of the encapsulated electrode ($500 \text{ }^\circ\text{C}$ morphological annealing) onsets at 1130 mV vs. RHE to reach $1.86 \text{ mA}\cdot\text{cm}^{-2}$ at 1430 mV vs. RHE with a maximum photocurrent of $2.34 \text{ mA}\cdot\text{cm}^{-2}$ before the onset of the dark current. The maximum photocurrent demonstrated here represents the highest

photocurrent ever reported for a solution-processed hematite film under standard solar illumination conditions and is furthermore near the values reported with state-of-the-art silicon-doped films prepared by atmospheric pressure chemical vapor deposition.^{9,24} However, we observe a considerable anodic shift of the photocurrent onset when using the encapsulation technique. This anodic shift indicates inferior water oxidation kinetics compared to the control electrode most likely due to surface trapping states resulting from the encapsulation technique. In accordance with other reports,²⁵⁻²⁷ this observation suggests that the surface trap states are a critical factor in the photocurrent onset potential of hematite as a water splitting photo-anode. Electrodes for which the morphological annealing was performed at lower temperatures (350 and 450 °C), exhibited the same shift in onset potential but gave lower photocurrents even though they exhibited smaller average particle size (Appendix C3). Assuming this is not due to increased bulk recombination resulting from residual carbon left from the lower-temperature porogen removal (not likely at 450 °C), this result suggests that a trade-off exists between particle size and electron transport in this type of film. The further optimization of the film thickness may contribute to the additional understanding of this aspect. Nevertheless, the encapsulated electrode prepared at the established conditions does demonstrate a significant enhancement in photocurrent.

In order to clearly understand the mechanism by which the encapsulating strategy enhances the photocurrent, further study of the spectral response is needed. As such, the incident photon-to-current conversion efficiency (*IPCE*) of each electrode was analyzed at the plateau photocurrent potential, V_{plat} , and plotted with respect to the photon wavelength (Figure 6.4a). In order to accurately compare the two electrodes, compensating for the different photocurrent onset behavior due to surface states, the photoanode action spectra were both measured at the plateau photocurrent potential, V_{plat} , which is defined as the potential where the first derivative of the photocurrent is a minimum. This was 1.43 and 1.63 V vs RHE, respectively, for the control and encapsulated electrodes. The encapsulated electrode shows a drastic improvement for all photon wavelengths as compared to the control (e.g. *IPCE* = 47% and 24% at 350 nm, respectively). Given the average photon penetration depth in hematite (the reciprocal of the absorption coefficient, a) which increases monotonically from $a^{-1} = 50$ nm at $\lambda = 350$ nm to $a^{-1} = 300$ nm at $\lambda = 550$ nm,¹³ the increase in

IPCE is indeed anticipated for all wavelengths of absorbed light. This is due to the smaller hematite feature size present in the encapsulated electrode, as even for photons with a wavelength of 350 nm, a greater fraction of photons will be absorbed in the critical region 5–10 nm from the SCLJ in a porous electrode with a 30 nm feature size as compared to 90 nm. This mechanism for improvement is expected to be more effective for longer wavelengths of light, which have deeper penetration depths. In fact, this effect is precisely observed when comparing the relative quantum efficiencies and light absorption of the electrodes as a function of wavelength. Figure 6.4b shows the *IPCE* spectra of the control and encapsulated electrodes normalized at $\lambda = 350$ nm. We see clearly the effect of the smaller particle size in the encapsulated electrode as a higher relative conversion of the incident photons with longer wavelengths. Indeed, by calculating the relative percent difference – defined as $RPI = (IPCE_{\text{encap}} - IPCE_{\text{control}}) / (0.5(IPCE_{\text{encap}} + IPCE_{\text{control}}))$ – in the *IPCE*, we can find the encapsulated electrode's ability to harvest each wavelength of light improves with respect to the control electrode as penetration depth of the photons increases (Figure 6.4a). The improved conversion efficiency of the longer wavelength photons is especially important for hematite, as half of its maximum possible $12.6 \text{ mA}\cdot\text{cm}^{-2}$ solar photocurrent is provided by the wavelength range of 500 – 600 nm due to the distribution of photons in the solar spectrum. This also helps to explain the dramatic increase in solar photocurrent observed by simply controlling the feature size of the electrode.

A trivial explanation for the increase in the encapsulated electrode's solar water-splitting photocurrent and *IPCE* would simply be an increased light absorption in that film. This is however unlikely, as the films were initially deposited with the same amount of hematite. I further counter this explanation with the light absorption data of the electrodes shown in Figure 6.4b. The measured fraction of photons absorbed (absorbivity) in the control electrode is higher than in the encapsulated electrode at each wavelength and also exhibits a significant response at wavelengths greater than the band gap (ca. 600 nm) due to scattering caused by the large particles. This scattering effect is diminished in the encapsulated electrode, and the measured absorbivity is less than the control electrode over all wavelengths. Thus, the increased *IPCE* exhibited by the encapsulated electrode is not due an increased absorption of the film but is rather due to the desired enhancement of photon absorption in high

proximity to the SCLJ due to the finer nanostructure. These data also eliminate the possibility of a photoactive iron silicate species (e.g., FeSi, α and β -FeSi₂) increasing the photocurrent as these species have band gap energies less than 2.0 eV,^{28,29} and an insignificant amount of both absorption and photon-to-electron conversion is observed at energies less than 2.0 eV (620 nm) in the treated electrode.

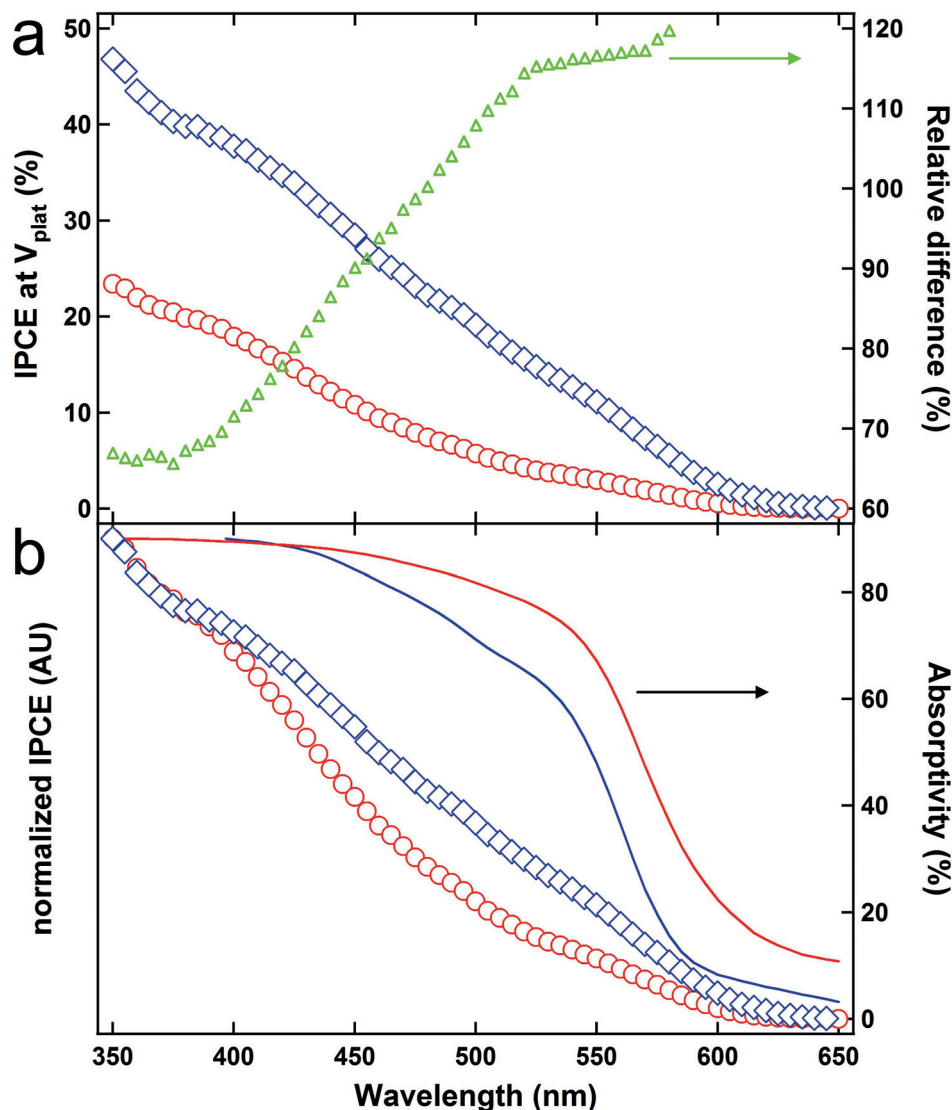


Figure 6.4 : a) Incident photon-to-current conversion efficiency at V_{plat} (see text) in 1 M NaOH electrolyte of control (circle markers) and encapsulated (500 °C morphological annealing, diamond markers) photo-anodes. The relative percent increase of the IPCE of the encapsulated electrode vs. the control is shown corresponding to the axis at right. b) Normalized IPCE (circle and diamond markers) and absorptivity (solid red and blue lines) for the control and encapsulated porous hematite electrodes, respectively.

The absorption data help to answer another important question concerning the light absorption and particle size in hematite. Recently, it has been reported that the optical transitions in hematite are altered in energy when heating the material to

high temperatures (ca. 800 °C) due to a relaxation in the crystal structure.³⁰ This structural relaxation has also been correlated to an increase in absorption coefficient and band-edge tailing parameter in porous films heated at these high temperatures.¹⁷ The complete understanding of the light absorption properties of hematite is certainly important for the application of solar energy conversion, however, with the previous work it remained unclear whether the structural relaxation and increase in absorption coefficient were due to the increase of feature size or if they were intrinsic to the material treated at high temperature regardless of crystalline domain size. Since the absorption of the encapsulated electrode shown here more closely resembles that of the 800 °C annealed control sample than the 400°C control sample previously reported,¹⁷ this suggests the structural relaxation¹⁷ and the increased band-edge tailing parameter can be afforded to hematite regardless of feature size. This observation also supports the suggestion that the structural relaxation itself plays an important role in the photoactivity of hematite. One example regarding the later aspect is described in the next section.

6.4 Attempt in passivating the surface

It is yet unclear whether the late onset potential of the photocurrent in all types of hematite photoanodes is caused by slow kinetics of the oxygen evolution reaction or if surface recombination at trapping states is the main factor. The first hypothesis has been investigated for years and the kinetics have been shown to be improved by using cobalt^{9,31} or iridium³² based surface catalysts. More recently, the passivation of surface states on water splitting hematite photoanodes has been demonstrated by using alumina overlayers coated conformally by atomic layer deposition (ALD).³³ This work identified for the first time the two distinct causes for the high overpotential observed in state-of-the-art nanostructured hematite photoanodes.

In this work and as further described in the Appendix C, the optimum photocurrent is obtained by using a morphological annealing at 500°C. This temperature is higher than the expected optimum at around 400°C, a temperature at which no organic compounds should be remaining in the film and at which a smaller feature size can be obtained. One hypothesis behind this result is that a competition must exist between efficient photogenerated hole diffusion to the surface (enabled by the small feature size) and hole recombination at the surface enhanced by greater

surface area, i.e smaller feature size. Indeed, if the injection of majority charge carrier is driven by the electric field of the space charge layer, a higher surface area for the same amount of photogenerated charges implies a dilution of the holes on the surface, therefore a larger depletion width and a weaker electric field. In addition, the late onset potential due to the harsh treatment of the nanostructure's surface (infiltration, high temperature and exposure to strong base for scaffold removal) could be arising from the incorporation of additional intra-band gap surface traps.

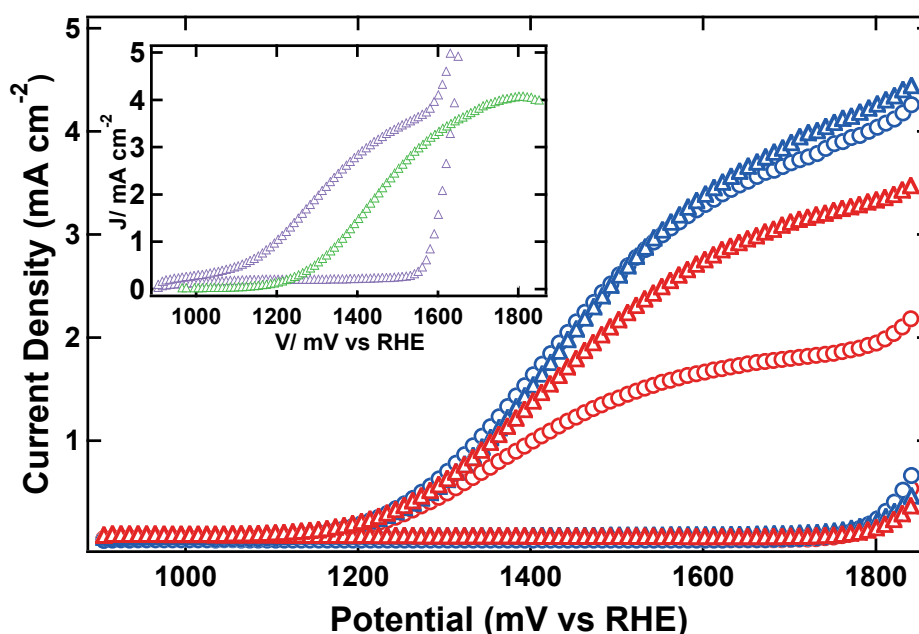


Figure 6.5 : Electrochemical water oxidation photocurrent and dark current vs. applied voltage curves of photoanodes with morphological annealing at 400°C (circles) and 500°C (triangles) before (red) and after (blue) the deposition by ALD of an alumina overlayer under simulated solar light (AM 1.5G 100 mW cm⁻², spectrally corrected) in 1 M NaOH electrolyte. Inset shows the net photocurrent (green) peaking above 4 mA.cm⁻² of the photoanode with morphological annealing at 500°C after ALD of alumina overlayer as well as photocurrent of the same electrode after cobalt nitrate catalyst treatment.

I applied the procedure described by Le Formal et al. to the system presented in this chapter in order to 1- verify the inclusion of surface traps by the infiltration process 2- passivate the surface by filling oxygen vacancies, dangling bonds or disorder in the cristalinity of the material. Samples similar to the encapsulated photoanodes presented earlier in this chapter with morphological annealing at 500°C and 400°C were coated with 20 cycles of alumina by ALD, using trimethylaluminium (TMA) as a metal precursor and water as an oxidant, identically to the literature. The result is presented in Figure 6.5. As seen before (see appendix C), the 400°C sample exhibits a

photocurrent of about half the one exhibited by the well optimized 500°C after rigid scaffold removal and both samples have a late onset potential of about 1200 mV. After deposition of the alumina overlayer, a strong increase of respectively 107 % and 29% in the photocurrent is observed to more than 4 mA.cm⁻² at 1800 mV for both samples. Other results (not shown here) exhibit similar behavior: if a similar amount of hematite is deposited, applying the ALD treatment annuls the difference in photocurrent induced by different morphological annealing temperature. This result suggests that the main limiting factor for this system is the quality of the surface rather than the size of the particles. However, the analysis of the *IPCE* spectra of the electrodes that would allow to further compare the effect of the nanostructure are not presented here. Interestingly, the improvement in the onset potential of the photocurrent expected from the literature was not observed. This feature is currently under investigation. In addition, the application of a Co²⁺ catalyst⁹ pushed the onset potential of the photocurrent about 150 mV cathodically, almost twice as much as what is expected from literature. This suggests that the encapsulation process mainly has detrimental influence on the kinetics of the oxygen evolution reaction.

Finally, the maximum net photocurrent (see inset Figure 6.5) obtained by applying the alumina overlayer exceeds 4 mA.cm⁻². This result has been reproduced with several samples and is the highest net photocurrent reported up to date with any hematite photoanode. It represents a benchmark in the field, even if the potential at which it is obtained is as high as 1800 mV.

6.5 Conclusion

In summary, a new encapsulation strategy where the morphological and functional effects of annealing are effectively decoupled has been experimentally demonstrated using porous hematite electrodes. Four simple solution-based steps are involved in this technique; the initial film deposition and morphological annealing first defines the average particle size and connectivity of the nanostructure, the encapsulation of this structure with a conformal silica layer next acts to confine and prevent further particle growth. The subsequent functional annealing activates the material at high temperature, and finally, the removal of the silica by selective etching gives the final porous electrode. I have shown that using this approach allowed the activation of nanostructured hematite photo-anodes with wide-ranging control over

the particle size in the porous film. The ability to decouple the particle size and the functionality led to a significant increase in the quantum conversion efficiency over the entire absorption spectrum as compared to the control sample, giving rise to the highest water oxidation photocurrent ($2.34 \text{ mA}\cdot\text{cm}^{-2}$ under standard illumination conditions) reported for solution-processed porous hematite photo-electrodes. Given the versatility of conformal SiO_2 deposition and removal (both acidic and basic conditions are available for both steps) our strategy could potentially be applied to any kind of complex substrate-based nanostructure where an annealing step is complicated by the sintering and collapse of the architecture. As such, more sophisticated nanostructures of hematite and other materials will now be accessible as electrodes. In addition, a combination of this strategy and the application of a surface passivating alumina overlayer allowed net photocurrents as high as $4 \text{ mA}\cdot\text{cm}^{-2}$ at 1800 mV, the highest photocurrent ever obtained with this material.

Supporting Information Available. Full experimental procedures, the results of the XPS surface analysis, and SEM and photoelectrochemical characterization of films with 350 and 450 °C morphological annealing. This material is available in the appendix C of this thesis.

6.6 References

1. Graetzel, M. Photoelectrochemical cells. *Nature* 414, 338–344 (2001).
2. Deng, D., Kim, M. G., Lee, J. Y. & Cho, J. Green energy storage materials: Nanostructured TiO_2 and Sn-based anodes for lithium-ion batteries. *Energy & Environmental Science* 2, 818 (2009).
3. Franke, M., Koplín, T. & Simon, U. Metal and Metal Oxide Nanoparticles in Chemiresistors: Does the Nanoscale Matter? *Small* 2, 36–50 (2006).
4. Bass, J. D., Grosso, D., Boissiere, C. & Sanchez, C. Pyrolysis, crystallization, and sintering of mesostructured titania thin films assessed by in situ thermal ellipsometry. *J Am Chem Soc* 130, 7882–7897 (2008).
5. Hu, Y.-S. et al. Pt-Doped $\alpha\text{-Fe}_2\text{O}_3$ Thin Films Active for Photoelectrochemical Water Splitting. *Chem Mater* 20, 3803–3805 (2008).

6. Beermann, N., Vayssieres, L., Lindquist, S. & Hagfeldt, A. Photoelectrochemical studies of oriented nanorod thin films of hematite. *J Electrochem Soc* 147, 2456–2461 (2000).
7. Saretni-Yarahmadi, S., Wijayantha, K. G. U., Tahir, A. A. & Vaidhyanathan, B. Nanostructured α -Fe₂O₃ Electrodes for Solar Driven Water Splitting: Effect of Doping Agents on Preparation and Performance. *J Phys Chem C* 113, 4768–4778 (2009).
8. Mohapatra, S. K., John, S. E., Banerjee, S. & Misra, M. Water Photooxidation by Smooth and Ultrathin α -Fe₂O₃ Nanotube Arrays. *Chem Mater* 21, 3048–3055 (2009).
9. Kay, A., Cesar, I. & Graetzel, M. New Benchmark for Water Photo-oxidation by Nanostructured α -Fe₂O₃ Films. *J Am Chem Soc* 128, 15714–15721 (2006).
10. Prakasam, H. E., Varghese, O. K., Paulose, M., Mor, G. K. & Grimes, C. A. Synthesis and photoelectrochemical properties of nanoporous iron (III) oxide by potentiostatic anodization. *Nanotechnology* 17, 4285–4291 (2006).
11. Bjoerksten, U., Moser, J. & Graetzel, M. Photoelectrochemical Studies on Nanocrystalline Hematite Films. *Chem Mater* 6, 858–863 (1994).
12. Brillet, J. et al. Examining architectures of photoanode-photovoltaic tandem cells for solar water splitting. *J Mater Res* 25, 17–24 (2010).
13. Marusak, L. & Messier, R. Optical absorption spectrum of hematite, α -Fe₂O₃ near IR to UV. *Journal of Physics and Chemistry of ...* (1980).
14. Sanchez, C., Sieber, K. D. & Somorjai, G. A. The photoelectrochemistry of niobium doped α -Fe₂O₃. *Journal of Electroanalytical Chemistry and Interfacial Electrochemistry* 252, 269–290 (1988).
15. Kennedy, J. & Frese, K., Jr Photooxidation of Water at α -Fe₂O₃ Electrodes. *J Electrochem Soc* 125, 709 (1978).
16. Peng, L. et al. Surface photovoltage characterization of an oriented α -Fe₂O₃ nanorod array. *Chemical Physics Letters* 459, 159–163 (2008).
17. Sivula, K. et al. Photoelectrochemical Water Splitting with Mesoporous Hematite Prepared by a Solution-Based Colloidal Approach. *J Am Chem Soc* 132, 7436–7444 (2010).
18. Kuo, Y. & Kozlowski, P. M. Polycrystalline silicon formation by pulsed rapid thermal annealing of amorphous silicon. *Appl Phys Lett* 69, 1092–1094 (1996).
19. Rooth, M. R. et al. Atomic Layer Deposition of Iron Oxide Thin Films and Nanotubes using Ferrocene and Oxygen as Precursors. *Chem Vapor Depos* 14, 67–70 (2008).
20. Jiao, F. et al. Synthesis of ordered mesoporous Fe₃O₄ and γ -Fe₂O₃ with crystalline walls using post-template reduction/oxidation. *J Am Chem Soc* 128, 12905–12909 (2006).
21. Mialon, G., Gohin, M., Gacoin, T. & Boilot, J.-P. High Temperature Strategy for Oxide Nanoparticle Synthesis. *ACS nano* 2, 2505–2512 (2008).
22. Atkinson, A. & Taylor, R. Diffusion of Fe⁵⁵ in Fe₂O₃ single crystals. *J Phys Chem Solids* 4, (1984).
23. Ogawa, M., Shimura, N. & Ayril, A. Deposition of Thin Nanoporous Silica Layers on Solid Surfaces. *Chem Mater* 18, 1715–1718 (2006).

24. Cesar, I., Sivula, K., Kay, A., Zboril, R. & Graetzel, M. Influence of Feature Size, Film Thickness, and Silicon Doping on the Performance of Nanostructured Hematite Photoanodes for Solar Water Splitting. *J Phys Chem C* 113, 772–782 (2009).
25. Horowitz, G. Capacitance-voltage measurements and flat-band potential determination on Zr-doped α -Fe₂O₃ single-crystal electrodes. *Journal of Electroanalytical Chemistry and Interfacial Electrochemistry* 159, 421–436 (1983).
26. Dare-Edwards, M. P., Hamnett, A. & Trevellick, P. R. Alternating-current techniques in semiconductor electrochemistry. *J. Chem. Soc., Faraday Trans. 1* 79, 2111–2124 (1983).
27. Le Formal, F., Graetzel, M. & Sivula, K. Controlling Photoactivity in Ultrathin Hematite Films for Solar Water-Splitting. *Adv Funct Mater* 20, 1099–1107 (2010).
28. Liu, Z., Watanabe, M. & Hanabusa, M. Electrical and photovoltaic properties of iron-silicide/silicon heterostructures formed by pulsed laser deposition. *Thin Solid Films* 381, 262–266 (2001).
29. Girlanda, R., Piparo, E. & Balzarotti, A. Band structure and electronic properties of FeSi and α -FeSi₂. *J Appl Phys* 76, 2837 (1994).
30. Pailhé, N., Wattiaux, A., Gaudon, M. & Demourgues, A. Impact of structural features on pigment properties of α -Fe₂O₃ hematite. *J Solid State Chem* 181, 2697–2704 (2008).
31. Zhong, D. K., Cornuz, M., Sivula, K., Graetzel, M. & Gamelin, D. R. Photo-assisted electrodeposition of cobalt–phosphate (Co–Pi) catalyst on hematite photoanodes for solar water oxidation. *Energy & Environmental Science* 4, 1759–1764 (2011).
32. Tilley, S. D., Cornuz, M., Sivula, K. & Graetzel, M. Light-induced water splitting with hematite: improved nanostructure and iridium oxide catalysis. *Angew. Chem. Int. Ed.* 49, 6405–6408 (2010).
33. Le Formal, F. et al. Passivating surface states on water splitting hematite photoanodes with alumina overlayers. *Chem. Sci.* 2, 737–743 (2011).

Part C
Nanostructures for the Dye
Sensitized Solar Cell

Dye-sensitized solar cells (DSCs) are one of the most promising photovoltaic technologies for production of renewable, clean, and affordable energy. They are generally made from cheap and nontoxic components and can be designed in a variety of different colors and transparencies, which distinguishes them as an ideal photovoltaic concept for integrated “green” architecture. Additionally, they have been shown to be competitive with other thin film technologies reaching certified efficiencies as high as 11.1% when using a triiodide/iodide (I_3^-/I^-) redox shuttle.¹⁻³

In DSCs, charge carrier generation takes place in a chemisorbed monolayer of photoactive dye that is sandwiched between a semiconducting oxide, usually anatase TiO_2 , and an electrolyte acting as electron and hole conducting materials, respectively. Because of the relatively low-absorption cross-section of the molecular sensitizer, a high surface area mesoscopic photoanode is necessary to ensure high dye loading and efficient light harvesting in the visible part of the solar spectrum. This implies that the DSC has an exceedingly large, heterogeneous interface through which electrons may be (parasitically) intercepted as a result of the slow electron transport. The latter is governed by an ambipolar diffusion mechanism controlled by trap-limited hopping through a relatively long and tortuous path to the transparent conductive electrode.⁴⁻⁷ It is further hindered by the low electron mobility in anatase TiO_2 nanoparticles and

the multiple grain boundaries in the mesoporous film.⁸

Given a charge collection time of milliseconds at the maximum power point,⁹ efficient charge extraction is only made possible when using the (I_3^-/I^-) redox couple through the slow interception of electrons by adjacent I_3^- .¹⁰ In addition to limited light harvesting by the dye, one of the main limiting factors of efficiency is the excessive driving force of 0.6 eV necessary for the dye-regeneration process leading to a significant loss-in-voltage of approximately 600 mV.^{7,11,12} This has sparked development and study of various alternative redox couples including p-type semiconductors.¹³ Increasingly, development has been centered around the use of organic hole-transporting materials (HTM) in solid-state DSCs (ss-DSCs).¹⁴⁻¹⁷

The electronic loss that is typically discussed for DSCs is slow transport-induced recombination.¹⁸⁻²¹ If charges recombine before reaching the electrode then this has a direct influence on the photocurrent and photovoltage. The open-circuit voltage is defined by the splitting of the quasi-Fermi level of electrons in the metal oxide and the redox potential of the electrolyte (quasi-Fermi level of holes in the hole-transporter). Hence, the closer the Fermi level in the metal oxide can be pushed toward the conduction band and LUMO level of the sensitizer, the higher the open-circuit voltage, and the smaller the loss-in-potential going from the level of the excited state of the dye to the quasi-Fermi level in the metal oxide. Two strategies can contribute to this upward shift and increase the open-circuit potential, namely reducing the recombination rate constant enabling the Fermi level to move closer to the conduction band before the recombination rate balances the charge generation rate or shifting the conduction band itself. Finally, enhancing the electron transport could improve charge collection and reduce IR losses, enhance the short-circuit current, and fill factor.^{12,18}

Several approaches have been proposed in order to reduce interfacial recombination and improve charge collection in liquid electrolytes and ss-DSCs including the use of radial collection nanostructures,⁷ one-dimensional ZnO and TiO₂ nanorods, and nanowires as photoanodes.²²⁻²⁵ and some are described in the previous chapter. Even though these approaches show great promise, they have yet to achieve power conversion efficiencies above 5% in liquid electrolyte DSCs and 1.7% in ss-DSCs. In this part of my thesis, I expose results on the strategies I have pursued

during the course of my PhD to improve the dynamics in the liquid and ss-DSC. From one-dimensional titania nanotubes, I have moved to tri-dimensional fibrous network of crystalline TiO₂ and more complex host-passivation-guest photoelectrode.

1. Chiba, Y. et al. Dye-sensitized solar cells with conversion efficiency of 11.1%. *Japanese Journal of Applied Physics* 45, 1638–1640 (2006).
2. Gao, F. et al. Enhance the Optical Absorptivity of Nanocrystalline TiO₂ Film with High Molar Extinction Coefficient Ruthenium Sensitizers for High Performance Dye-Sensitized Solar Cells. *J Am Chem Soc* 130, 10720–10728 (2008).
3. Graetzel, M. The advent of mesoscopic injection solar cells. *Prog. Photovolt: Res. Appl.* 14, 429–442 (2006).
4. Dloczik, L. et al. Dynamic Response of Dye-Sensitized Nanocrystalline Solar Cells: Characterization by Intensity-Modulated Photocurrent Spectroscopy. *J. Phys. Chem. B* 101, 10281–10289 (1997).
5. Kopidakis, N., Schiff, E., Park, N., van de Lagemaat, J. & Frank, A. Ambipolar diffusion of photocarriers in electrolyte-filled, nanoporous TiO₂. *J Phys Chem B* 104, 3930–3936 (2000).
6. van de Lagemaat, J., Zhu, K., Benkstein, K. D. & Frank, A. J. Temporal evolution of the electron diffusion coefficient in electrolyte-filled mesoporous nanocrystalline TiO₂ films. *Inorganica Chimica Acta* 361, 620–626 (2008).
7. Martinson, A. B. F. et al. Radial electron collection in dye-sensitized solar cells. *Nano Letters* 8, 2862–2866 (2008).
8. Abayev, I., Zaban, A., Fabregat-Santiago, F. & Bisquert, J. Electronic conductivity in nanostructured TiO₂ films permeated with electrolyte. *Phys Status Solidi A* 196, R4–R6 (2003).
9. Wang, Q. et al. Characteristics of high efficiency dye-sensitized solar cells. *J Phys Chem B* 110, 25210–25221 (2006).
10. Clifford, J. N., Palomares, E., Nazeeruddin, M. K., Graetzel, M. & Durrant, J. R. Dye dependent regeneration dynamics in dye sensitized nanocrystalline solar cells: Evidence for the formation of a ruthenium bipyridyl cation/iodide intermediate. *J Phys Chem C* 111, 6561–6567 (2007).
11. Zhang, Z., Chen, P., Murakami, T. N., Zakeeruddin, S. M. & Graetzel, M. The 2,2,6,6-tetramethyl-1-piperidinyloxy radical: An efficient, iodine-free redox mediator for dye-sensitized solar cells. *Adv Funct Mater* 18, 341–346 (2008).
12. Snaith, H. J. Estimating the Maximum Attainable Efficiency in Dye-Sensitized Solar Cells. *Adv Funct Mater* 20, 13–19 (2010).
13. O'Regan, B. C., Schwartz, D., Zakeeruddin, S. & Graetzel, M. Electrodeposited nanocomposite n-p heterojunctions for solid-state dye-sensitized photovoltaics. *Adv Mater* 12, 1263–+ (2000).
14. Bach, U. et al. Solid-state dye-sensitized mesoporous TiO₂ solar cells with high photon-to-electron conversion efficiencies. *Nature* 395, 583–585 (1998).
15. Snaith, H. J. et al. Efficiency Enhancements in Solid-State Hybrid Solar Cells via

- Reduced Charge Recombination and Increased Light Capture. *Nano Lett* 7, 3372–3376 (2007).
16. Wang, M. et al. High efficiency solid-state sensitized heterojunction photovoltaic device. *Nano Today* 5, 169–174 (2010).
 17. Cai, N. et al. An Organic D- π -A Dye for Record Efficiency Solid-State Sensitized Heterojunction Solar Cells. *Nano Lett* 11, 1452–1456 (2011).
 18. Barnes, P. R. F. et al. Re-evaluation of Recombination Losses in Dye-Sensitized Cells: The Failure of Dynamic Relaxation Methods to Correctly Predict Diffusion Length in Nanoporous Photoelectrodes. *Nano Lett* 9, 3532–3538 (2009).
 19. Kopidakis, N., Benkstein, K., van de Lagemaat, J. & Frank, A. Transport-limited recombination of photocarriers in dye-sensitized nanocrystalline TiO₂ solar cells. *J Phys Chem B* 107, 11307–11315 (2003).
 20. Nelson, J., Haque, S., Klug, D. & Durrant, J. Trap-limited recombination in dye-sensitized nanocrystalline metal oxide electrodes. *Phys. Rev. B* 63, – (2001).
 21. Snaith, H. J. et al. Charge collection and pore filling in solid-state dye-sensitized solar cells. *Nanotechnology* 19, – (2008).
 22. Law, M., Greene, L., Johnson, J., Saykally, R. & Yang, P. Nanowire dye-sensitized solar cells. *Nat Mater* 4, 455–459 (2005).
 23. Martinson, A. B. F., Elam, J. W., Hupp, J. T. & Pellin, M. J. ZnO nanotube based dye-sensitized solar cells. *Nano Lett* 7, 2183–2187 (2007).
 24. Mor, G. K., Varghese, O. K., Paulose, M., Shankar, K. & Grimes, C. A. A review on highly ordered, vertically oriented TiO₂ nanotube arrays: Fabrication, material properties, and solar energy applications. *Sol Energ Mat Sol C* 90, 2011–2075 (2006).
 25. Chen, P. et al. Solid-state dye-sensitized solar cells using TiO₂ nanotube arrays on FTO glass. *J Mater Chem* 19, 5325–5328 (2009).

Chapter 7. One-dimensional photoanodes for the DSC

This chapter is adapted from a peer-reviewed manuscript by Daibin Kuang, Jérémie Brillet, Peter Chen, Satoshi Uchida, Shaik. M. Zakeeruddin, and Michael Grätzel published in 2008 in ACS Nano, vol. 2 (6), pp 1113–1116 and another by Peter Chen, Jérémie Brillet, Hari Bala, Peng Wang, Shaik M. Zakeeruddin and Michael Grätzel published in 2009 in the Journal of Material Chemistry, vol. 19, pp 5325.

Dye-sensitized solar cells (DSCs) have attracted great interest in academic research due to the potential low cost alternative to the traditional silicon solar cells.¹ A DSC typically consists of a nanocrystalline TiO₂ film covered by a monolayer of dye molecules, redox electrolyte, and counter electrode. Cells based on randomly associated TiO₂ nanoparticles with a size of 10-30 nm have been widely used as photoanode achieving 11 % photovoltaic conversion efficiency.² Considerable efforts have been devoted to the development of more efficient photoanode materials including ordered meso-structured materials,³ one-dimension structured materials (nanorod, nanowire, nanotube) etc.⁴⁻⁶ In these materials superior photovoltaic performances may be achieved through the realization of photoanode materials with ordered structure resulting in the improvement of electron transport. Highly ordered TiO₂ nanotube arrays are particularly attractive candidates to achieve this task.⁶⁻⁸

7.1 Application of highly ordered TiO₂ nanotube-arrays in flexible Dye-sensitized Solar Cells

7.1.1 *Metallic foil substrate enables flexible DSC*

Flexible solar cells are of great advantage because of potential low cost roll-to-roll production and have been described previously by a number of groups.⁹⁻¹¹ Metal or transparent conductive copolymers were used as substrate for the working electrode and/or counter electrode but photovoltaic performance is hampered by slow electron transport in nanoparticle films that underwent low temperature sintering or/and a large resistance of the ITO polymer current collector. Recently our group has reported a remarkable light to electricity conversion efficiency for the flexible solar cells based on TiO₂ nanoparticles coated on the Ti foil as working electrode and ITO-PEN as counter electrode.¹² However these flexible DSCs contains volatile organic solvent electrolyte that precludes practical applications due to the organic solvent permeation across the plastic current collector. Hence, the ultimate redox electrolyte for flexible DSC application should be a solvent free electrolyte. Ionic liquids present significant practical advantages over organic solvent electrolytes and represent potential candidates to replace organic solvent electrolytes. Recently, we achieved a new record of 7.6 % efficiency for a new binary ionic liquid (1-propyl-3-methylimidazolium iodide and 1-ethyl-3-methyl-imidazolium tetracyanoborate) electrolyte based DSCs.¹³

Herein, we report for the first time on the use of ordered TiO₂ nanotube array as photoanode material for ionic liquid electrolyte-based rigid and flexible DSCs, that showed impressive photovoltaic performance.

7.1.2 *Making TiO₂ Nanotube arrays*

Highly ordered TiO₂ nanotube arrays were prepared by anodization of Ti foils (99.7 %, 0.25 mm, Aldrich) in a two-electrode cell containing a Pt counter electrode.¹⁴⁻¹⁶ The anodization was performed at 35 V at room temperature in a solution of 0.25 wt % NH₄F and 0.75 wt % H₂O in ethylene glycol for different time intervals that resulted in various nanotube lengths. The as-prepared TiO₂ nanotube samples were soaked in 0.04 M aqueous TiCl₄ solution for 30 min at 70 °C, which

improves the photocurrent and photovoltaic performance. The TiCl_4 treated TiO_2 nanotube samples were rinsed with water and ethanol and then annealed in air at $500\text{ }^\circ\text{C}$ for 3 h using a heating rate of $2\text{ }^\circ\text{C}/\text{min}$ in order to crystallize the initially amorphous anodized films. The sample morphology and crystallinity were characterized using scanning electron microscopy (JEOL FESEM) and X-ray diffraction (XRD), respectively. The sintered nanotube samples were immersed into 0.3 mM solution of a novel indoline organic dye coded as D205¹⁷ in acetonitrile and tert-butyl alcohol (volume ratio 1:1) for 16h. The newly developed binary ionic liquid electrolyte contained 0.05 M I_2 , 0.5 M N-butylbenzimidazole (NBB), 0.1 M Guanidinium thiocyanate (GuNCS) in a mixture of 65 vol % PMII and 35 vol % EMIB(CN)₄.^{13,18} Pt/FTO-glass or Pt/ITO-polyethylene naphthalate (ITO-PEN, a gift from Konarka, USA) were used as counter electrode for rigid or flexible solar cells, respectively. The detailed fabrication procedures and photovoltaic performance characterizations of DSCs are explained in Appendix A and B. Electrochemical impedance spectroscopy of the DSCs were obtained in the dark at -0.7 V forward bias using a potentiostat (EG&G, M273) equipped with a frequency response analyzer (EG&G, M1025). Transient photovoltage measurements employed a 200 ms exciting pulse generated by a ring of red light emitting diodes (LEDs, Lumiled) controlled by a fast solid-state switch. Transients were measured at different white light intensities ranging from 150% to 0.1% of AM 1.5 solar light ($1000\text{ W}/\text{m}^2$) and adjusted via tuning of the voltage applied to the bias diodes.

7.1.3 Flexible device performances

Figure 7.1 shows typical SEM images of TiO_2 nanotubes (TNT) obtained by the aforementioned anodization procedures. The average TNT lengths are $5\text{ }\mu\text{m}$, $7\text{ }\mu\text{m}$ and $14\text{ }\mu\text{m}$ as the anodization time increased from 2 h (a), 4 h (b) and 20 h (c), respectively. The closely packed highly ordered TNT were obtained at present anodization conditions independent of the time. Figure 7.1d is the enlarged image of the sample made with 4 h anodization, which shows $\sim 70\text{ nm}$ pore size with $\sim 8\text{ nm}$ TNT walls. The samples' structures were characterized by XRD measurements (data not shown). The XRD patterns of a $7\text{ }\mu\text{m}$ thick TNT film after annealing at $500\text{ }^\circ\text{C}$ for 3 h showed that the TNT samples have anatase structure in contrast to earlier work where the presence of rutile at the interface between the TNT and Ti substrate

was suggested.¹⁹ However, rutile was not witnessed in our present preparations.

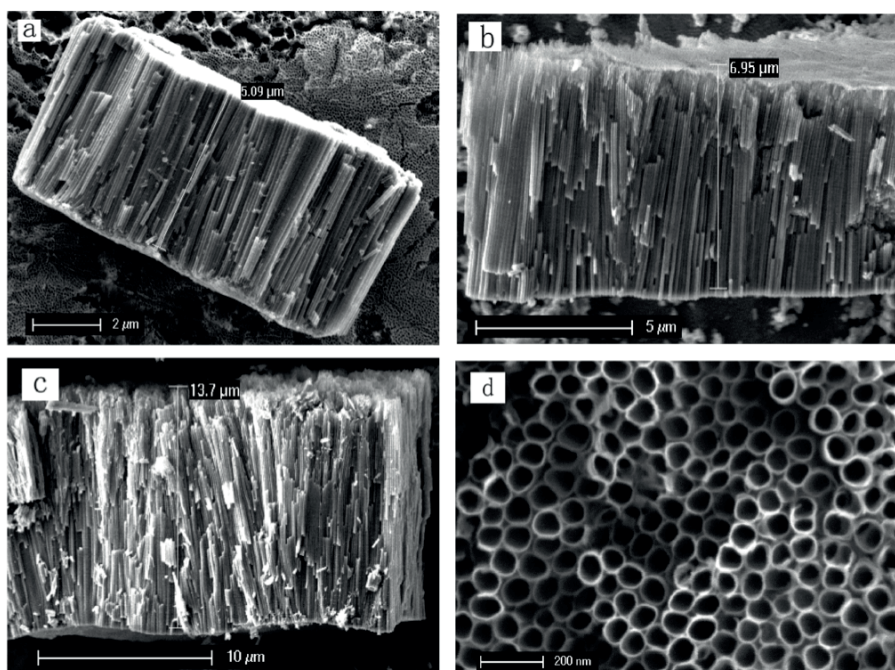


Figure 7. 1 : SEM images of TiO₂ nanotubes made with different anodization time: a) 2h, 5 μm in length; b) 4h, 7 μm in length; c) 20h, 14 μm in length; d) the enlarged image for the 4h sample, 70 nm pore size and 8 nm wall thickness.

Figure 7.2 shows the current-voltage curves of DSCs based on the organic dyes and the binary ionic liquid electrolyte as a function of TNT length under simulated AM 1.5 light. The short-circuit photocurrent densities (J_{sc}) obtained with TNTs of 5 μm, 7 μm and 14 μm length was 4.95 mAcm⁻², 5.58 mA.cm⁻² and 6.11 mA.cm⁻², respectively. The highest photovoltaic performance of 3.3 % was achieved with a 14 μm length TNT sample. Detailed photovoltaic performance parameters of the DSCs for films with different nanotube length are presented in Table. 7.1. The V_{oc} of the DSCs decreases with increasing length of TNT nanotube due to the increase in the dark current which scales with the surface area of the titania films, in agreement with previous nanoparticle based DSCs.²⁰ The V_{oc} values in table 7.1 are higher by about 40 mV compared to typical values obtained with nanocrystalline films that show a similar photocurrent of 5-6 mAcm⁻² and employ the same electrolyte and the same ionic liquid as the TNT cells. This finding is encouraging as it indicates that the recapture of conduction band electrons by the tri-iodide ions in the ionic liquids is slower for the TNT-based films than for random particular networks.

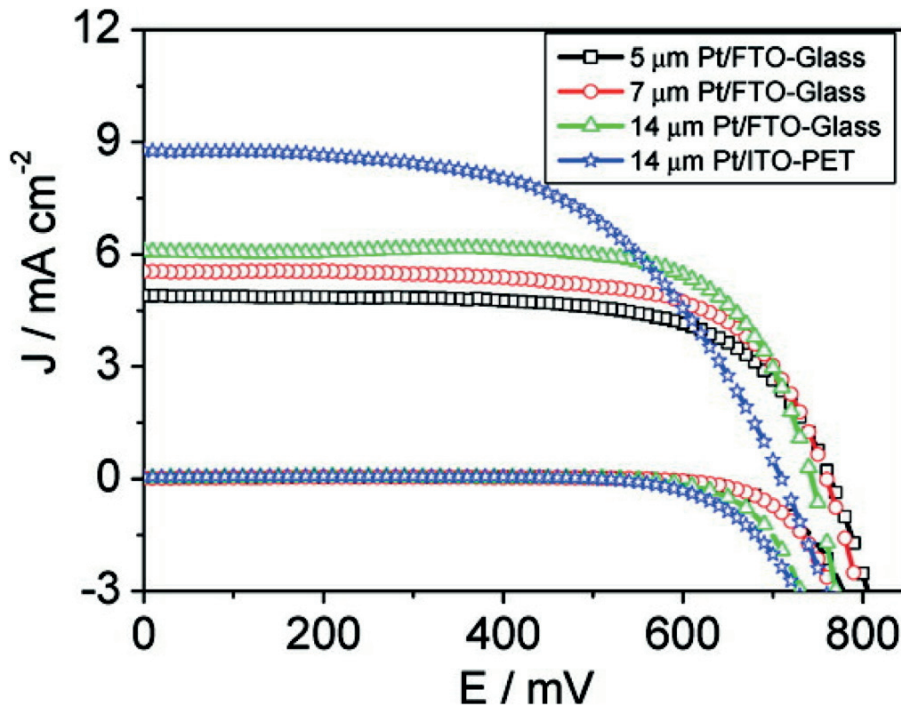


Figure 7.2 : Current-voltage characteristics of solar cells based on different TiO_2 nanotube lengths using rigid (Pt/FTO-glass) and flexible (Pt/ITO-PEN) substrates. Solid lines measured under AM 1.5 full sunlight (100 mW/cm^2) illumination. Dotted lines measured in the dark.

The dark current curves in Figure 7.2 confirm that the $14 \mu\text{m}$ TNT sample has a lower onset potential for the reduction of I_3^- than the other two samples which is in keeping with its higher surface area.

Table 7.1 : Photovoltaic performance parameters of solar cells based on different TiO_2 nanotube lengths with Pt/FTO-glass or Pt/ITO-PEN as counter electrodes measured under AM 1.5 full sunlight illumination (100 mW cm^{-2} , active area with a metal mask is 0.158 cm^{-2}).

TiO_2 NT length	Counter electrode	V_{oc} (mV)	J_{sc} (mA/cm^2)	Efficiency (%)	ff (%)
5	Pt/FTO-glass	763	4.95	2.52	66.6
7	Pt/FTO-glass	759	5.58	2.86	67.5
14	Pt/FTO-glass	743	6.11	3.29	72.5
14 (open cell)	Pt/ITO-PEN	709	8.99	3.58	56.1
14	Pt/ITO-PEN	705	7.80	3.19	58.0

In order to investigate a lightweight and flexible embodiment of the TNT cell, an ITO-PEN transparent conductive substrate was used to replace the FTO-Glass. It is interesting to note that the device made with flexible conductive Pt/ITO-PEN polymer substrate as counter electrode showed comparable photovoltaic performance to the Pt/FTO/Glass devices. The photovoltaic parameters (J_{sc} , V_{oc} , ff and η) of TiO_2 nanotube-based flexible solar cells were 8.99 mA.cm^{-2} , 709 mV , 0.561 and 3.58%

respectively (shown in Table 7.1). The flexible solar cells with Pt/ITO-PEN as counter electrode shows higher photocurrent compared to rigid solar cells with Pt/FTO-glass as counter electrode. This probably arises from the fact that the flexible counter electrode is directly placed on the TNT layer reducing optical losses as the triiodide ions contained in the ionic liquid filter the light that enters through the counter electrode.

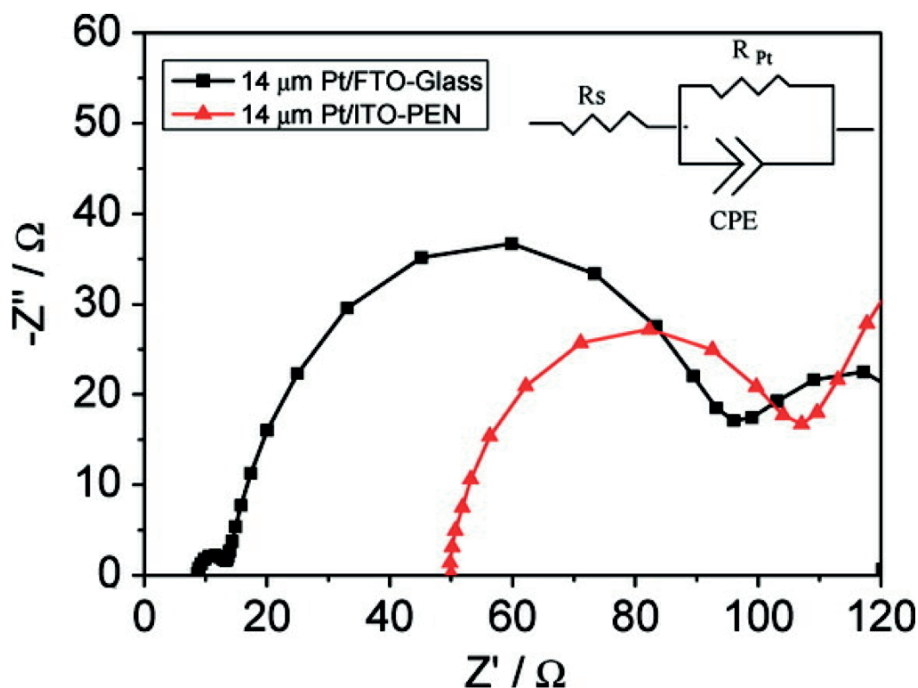


Figure 7.3 : Impedance spectra of DSCs based on 14 μm TiO_2 nanotube and rigid (Pt/FTO-glass) or flexible (Pt/ITO-PEN) counter electrodes, measured in the dark under -0.70 V applied bias. The inset shows the equivalent circuit used to analyse the high frequency semi circles.

Impedance spectroscopy has been regarded as a powerful technique to characterize the transport and recombination in DSCs and suitable physical models have been developed to accurately interpret the results.^{21,22} Impedance spectra were measured in the dark at an applied potential bias of -0.7 V. The high frequency semi circle in Nyquist plots corresponds to charge transfer at the counter electrode (Pt/redox interface). The reaction resistance of the counter electrode was analyzed by software (Z-view) using an equivalent circuit containing a constant phase element (CPE) and resistances (R) (Figure 7.4, inset). The series resistance (R_s) was found to be 8.9 ohm for rigid solar cells (FTO-glass) and 49.6 ohm for flexible solar cells (ITO-PEN). Further, the interface resistance of Pt/electrolyte (R_{Pt}) was 4.6 ohm and 62.4 ohm for Pt/FTO-glass and Pt/ITO-PEN, respectively. Therefore, the low f of

flexible DSC based on ITO-PEN substrate is attributed to higher R_s value and lower activity of the Pt catalyst on the ITO-PEN.

7.2 Solid-state dye-sensitized solar cells using TiO_2 nanotube arrays on FTO glass

7.2.1 *Transparent TiO_2 NT photoanode for SS-DSC*

Several research groups have used TNT arrays in DSCs using liquid electrolytes.^{7,23-27} Additionally, successful use of TNTs in polymer cells have yielded photocurrent densities as high as 12.4 mA/cm^2 .²⁸ In the Section 1 of this chapter, I report on a flexible DSC containing TNT arrays as photoanode and polyethylene naphthalate (PEN) as counter electrode in combination with a solvent free ionic liquid electrolyte.²⁹ Semiconductor quantum dots have been used as sensitizers by attaching them to the TNTs.^{30,31} Finally, different alloys like Ti-Fe-O and Ti-Cu-O were used to prepare TNTs for water splitting in photoelectrochemical cells.^{32,33}

In most cases, including in the first section of this chapter, the TNT arrays have been fabricated from a thick Ti film or foil, in which case the resulting TNTs rest upon an underlying Ti substrate. Here, arrays were synthesized from Ti thin films sputtered onto conducting materials such as FTO glass or metal substrates before being anodized to form the TNT arrays on these substrates.^{25,34} The TNT formation mechanism and their properties have been well described in the literature.^{7,8,14,35,36} While anodization is a simple and controllable process to make TNT arrays, it is known that the properties of these arrays are dependent on pore diameter, wall thickness and length of the tubes. The geometric features of TNT arrays are controlled by the nature of the electrolyte, the additives it contains, and the applied voltage. These factors have a significant influence on the growth, structure and morphology of the nanotubes.^{37,38}

The carrier density in the TNT array was found to be different when varying the electrolyte pH in an electrochemical cell.³⁹ The kinetic properties of DSCs using TNTs and nanoparticle films were compared using modulated photocurrent/photovoltage spectroscopy. It was found that the transport rate was similar in both cases but charge recombination was much slower in the TNT arrays. Thus electron lifetime was an order of magnitude greater than those obtained in

nanoparticle-based DSCs.⁶ A recent study also suggested that TNT-based DSCs would present a significantly higher charge-collection efficiency than their nanoparticle-based counterpart.⁴⁰ To the best of our knowledge there was no study on the penetration by solid-state hole transport material (HTM) into TNT arrays to form a parallel interpenetrating network for electron and hole transport. Herein, we present the first successful application of TNT arrays to ss-DSCs comprising a directional mesoporous structure forming direct charge transport channels normal to the conducting substrate.

7.2.2 Making TiO_2 NT on FTO

The TNT arrays were synthesized on FTO-coated glass substrate by way of depositing a double-layered structure comprising a Ti metal overlayer and a TiO_2 underlayer. For the ionic liquid DSC, the underlayer was synthesized by spray pyrolysis of ethanolic solution of di-iso-propoxy titanium-bis(acetylacetonate) [$Ti(acac)_2(i-C_3H_7O)_2$] in aerosol form. The metal overlayer was then deposited by conventional sputtering of a 1500 nm thick metal film from a Ti target. In this case, the 50 nm thick TiO_2 underlayer was first deposited by sputtering in a controlled O_2 atmosphere whereas the Ti overlayer was sputtered after shutting off the oxidizing gas and cleaning the target by Ar^+ milling for 5 minutes. The detailed parameters for the deposition process are listed in Table 7.3.

Table 7. 2 : Sputter deposition parameters for the TiO_2 and Ti film on FTO glass.

Process	Power (W)	Flow ratio Ar/ O_2 (sccm)	Process time (min)	Deposition rate ($nm.s^{-1}$)
Ignition	150	25/0	None	Shutter closed
Pre-sputter	150	20/2	5	Shutter closed
TiO_2 deposition	200	5/1	8–10	0.1
Target cleaning	200	20/0	5	Shutter closed
Ti deposition	150	10/0	60	0.3

Highly ordered TNT arrays were prepared by anodization of the Ti overlayer in a conventional two-electrode system using a platinum wire as counter electrode. The Ti overlayer was first thoroughly degreased by washing in acetone and ethanol for several minutes. No ultrasonic bath was used in order to minimize chances of delamination of the Ti/ TiO_2 from the conducting substrate. The distance between the working and counter electrode was kept at 3 cm. The anodization was conducted

at 35 V, without ramp, in an ethylene glycol electrolyte containing water (0.25 wt.%) and NH_4F (0.75 wt.%) until the homogeneous film turned transparent. After anodic oxidation, samples were rinsed with deionized water, ethanol and dried with compressed air. The as-prepared TNT arrays were soaked in 0.04 M TiCl_4 aqueous solution for 30 min at 70 °C to improve the photocurrent and photovoltaic performance of the DSCs. The TiCl_4 treated TNT samples were rinsed with deionized water and ethanol and then annealed in air at 500 °C for 3 hours (ramping rate 2 °C.min⁻¹) in order to crystallize the anodized amorphous films. The sample morphology was characterized using SEM.

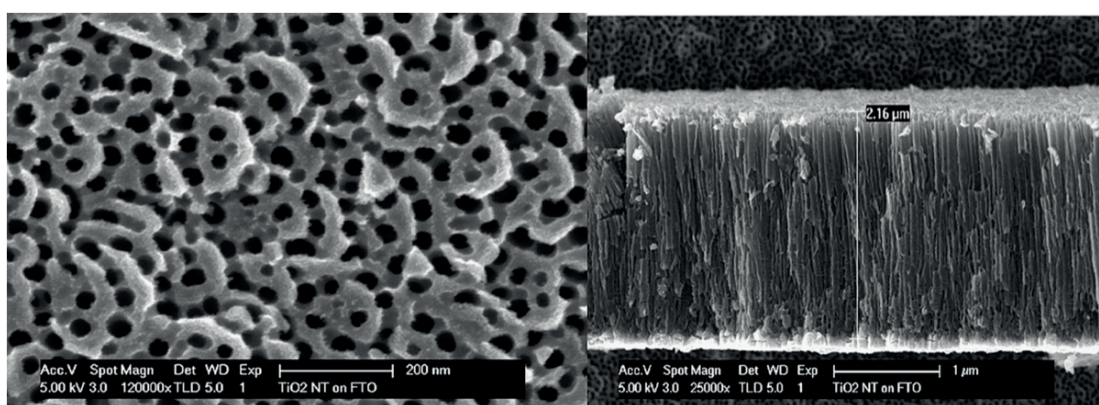


Figure 7.4 : Top view and cross section SEM image of TiO_2 nanotubes.

The surface of the TNT electrode was sensitized by immersing the array into a dye solution containing 300 mM C203 and 300 mM 3a,7a-dihydroxy-5b-cholanic acid in chlorobenzene at room temperature for 5 h.

7.2.3 Solid state device performances

SEM images of the TNT grown on top of the FTO glass substrate are shown in Figure 7.4. From the top view, we observed the pore diameter and a wall thickness of about 40–50 nm. The structure was found to be nano-wall-like instead of discrete tubes. The TiO_2 films were homogeneous across long range with a flat top layer and remained intact after annealing using the procedure described in the experimental section. By varying the parameters of anodization, we found it was possible to form separated TNT arrays but the top layer wasn't as smooth. Attempts using these films were unsuccessful due to individual tube protrusions creating a shunt path that deteriorates the cell performance. A flat top layer is advantageous to ensure an effective contact between the spin coated HTM and Au.

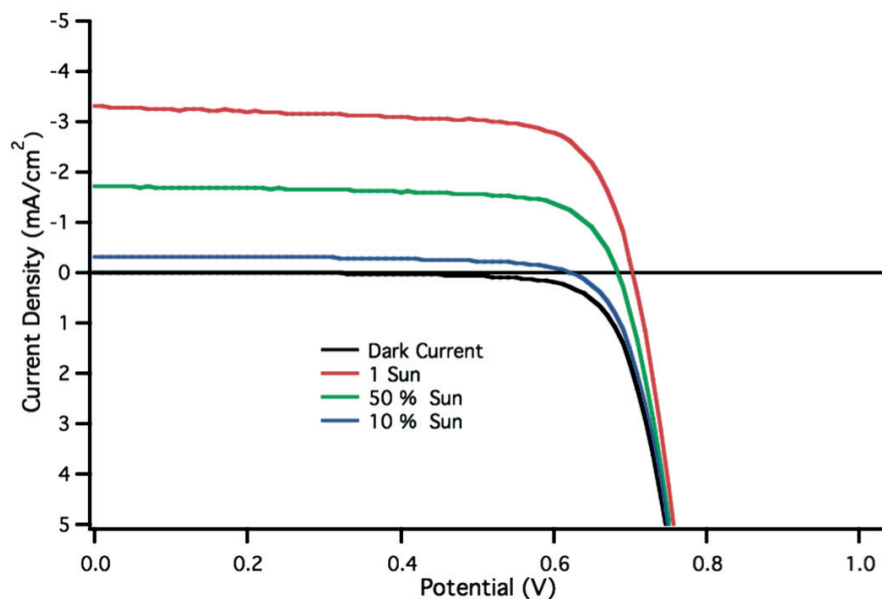


Figure 7.5 : *J-V* characteristics measured in the dark and under AM 1.5 G full sunlight illumination (100 mW cm^{-2}) of a TNT ss-DSC with C203 dye.

Some preliminary photovoltaic experiments were conducted to evaluate the use of these TNT arrays as negative electrode in ss-DSCs. The TNT arrays were sensitized using a high molar extinction coefficient organic dye coded as C203.⁴¹ This dye was chosen particularly for its high photon harvesting properties to counteract the effect of a lower surface area in the TNT arrays when compared to mesoporous TiO_2 electrodes. The surface of the TNT electrode was sensitized by immersing the array into a dye solution containing $300 \mu\text{M}$ C203 and $300 \mu\text{M}$ 3a,7a-dihydroxy-5b-cholanic acid in chlorobenzene at room temperature for 5 h. The devices were assembled using the standard ss-DSCs procedures described in the literature where we spin coated a solution of spiro-MeOTAD (0.17 M in chlorobenzene with Li-TFSI and ter-butylpyridine) on dye stained TNT arrays.⁴² The device fabrication was completed by thermal deposition of a Au positive electrode .

The *J-V* curves and monochromatic incident photon to current conversion efficiency (*IPCE*) spectrum of the ss-DSCs are shown in Figure 7.5 and 7.6. The short-circuit photocurrent density, open-circuit photovoltage, fill factor and efficiency of ss-DSCs are summarized in Table 7.4. In order to assess the light harvesting capacity of the TNT electrode, we compared the absorption spectrum of C203 dye adsorbed on a typical mesoporous TiO_2 film and our TNT arrays. Note that both films were approximately $2.0 \mu\text{m}$ thick.

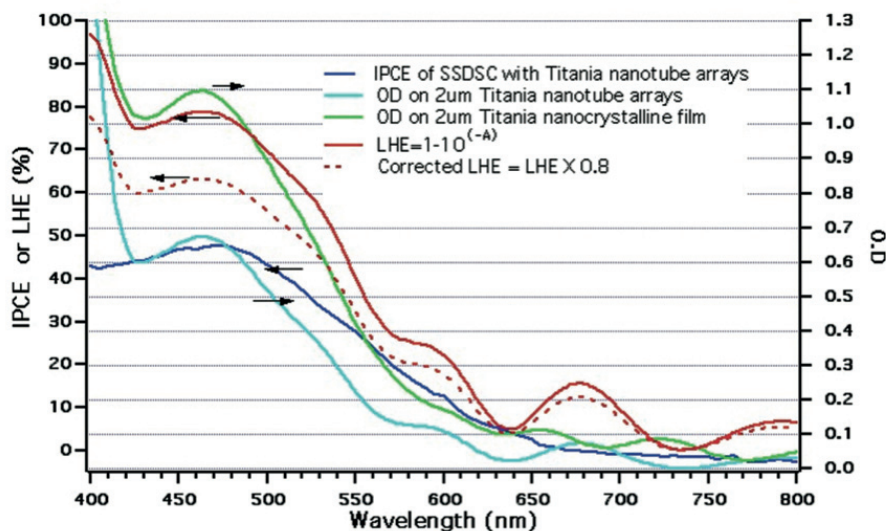


Figure 7.6 : IPCE characteristics of a TNT ss-DSC with absorbance of dye on TiO_2 film (nanotubes and nanoparticles) and the calculated and corrected LHE.

It can be seen in Figure 7.6 that the IPCE and absorption spectrum of the dye-sensitized TNT array shows the same C203 absorption features as the one obtained with the mesoporous TiO_2 film. Figure 7.6 also shows the relevant optical density for the NT arrays and the mesoporous films. The ratio of both was found to be about 60%. When we take into account that the dye loading on the NT array is about half of that in a mesoporous film, we believe that it is a significant result to obtain a current density of 3.30 mA/cm^2 and 1.67% efficiency at full sun intensity (AM 1.5) for a $2 \mu\text{m}$ thick ss-DSC. Assuming a 20% light loss from absorption and reflection from the FTO-coated substrate, one can estimate the internal quantum efficiency (*IQE*) using a simplified light harvesting efficiency (*LHE*) model (see equation (7.1)). The corrected LHE for our TiO_2 array is roughly 0.8 of the value given by equation (7.1) and is shown in Figure 7.6 as a red dashed line.

$$LHE = 1 - \exp(-\alpha) \quad (7.1)$$

As can be seen in Figure 7.6 the measured *IPCE* for the NT array is about 0.8–0.9 of the corrected *LHE* depending on the wavelength. Indeed, we find that the *IPCE* is closer to the corrected *LHE* in the red part of the spectrum than in the blue. We believe this is due to a stronger reflection from the gold counter electrode in the red than in the blue.⁴³ Since the dye's extinction coefficient is relatively low in this spectral region, the transmitted light is reflected back into the light harvesting TNT

array providing a second chance for the dye to absorb the photons, which translate into an enhanced *IPCE*. On the other hand, there is no gold reflection in the dye absorption measurement, and accordingly the *IPCE* is closer to the corrected *LHE* in the longer wavelength region. The wave-like absorption spectra in the red region appears due to the interference from the FTO substrate.

Table 7. 4 : Photovoltaic parameters of ss-DSCs made with TiO₂ nanotubes and nanocrystalline film at various light intensities.

TiO ₂ film	Light intensity (% sun)	V_{oc} (mV)	J_{sc} (mA/cm ²)	Efficiency (%)	ff (%)
Nanotube arrays	100.0	703.4	3.30	1.67	71.6
	51.0	682.6	1.72	1.64	71.4
	9.3	621.7	0.32	1.25	58.0
Nanocrystalline	100.0	930.0	5.10	3.42	71.1

A striking difference observed with the TiO₂ nanotube ss-DSC is the drop of voltage compared to the normal nanocrystalline ss-DSC devices (230 mV less than a nanoparticle-based cell). We suspect that further optimizing blocking TiO₂ under layer and sputtering parameters could mitigate this drop of V_{oc} . In a normal solid-state device, the blocking layer is made by spray pyrolysis and seems to block the junction more effectively than the underlayer presented here.

Photovoltaic experiments were conducted using the same transparent electrode with 2.8 μm thin nanotube arrays sensitized with C203 and ionic liquid as electrolyte. The devices were made using Pt/FTO glass as counter electrode and the two electrodes were separated by a 25 μm thick Surlyn hot-melt gasket and sealed up by heating. The internal space was filled with a solvent free ionic liquid based electrolyte using a vacuum back filling system. The solvent free ionic liquid electrolyte contained 0.05 M I₂, 0.5 M N-butylbenzimidazole, 0.1 M guanidinium thiocyanate in a mixture of 1-propyl-3-methylimidazolium iodide and 1-methyl-3-ethyl imidazolium tetracyanoborate, with a volume ratio of 65/35.¹⁸ The electrolyte-injecting hole made in advance by an ultrafine sandblaster on the counter electrode glass substrate was sealed with a Bynel sheet and a thin glass cover by heating.

The photocurrent action spectrum of the device is shown in Figure 7.7 as an inset. The *IPCE* exceeds 75% at 490 nm. As shown in Figure 7.7, the short-circuit photocurrent density, open-circuit photovoltage, and fill factor of the device under an irradiance of AM 1.5 G full sunlight are 7.9 mA.cm⁻², 677 mV and 0.693, respectively, yielding an overall conversion efficiency of 3.8%. It is remarkable to obtain such an

impressive performance with a 2.8 μm thin NT array film.

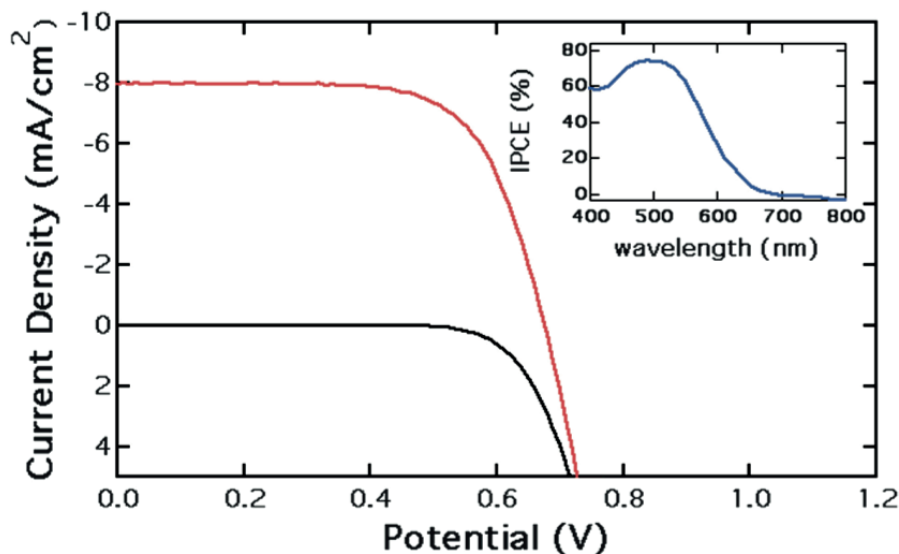


Figure 7.7 : J - V characteristics measured in the dark and under AM 1.5 G full sunlight illumination (100 mW cm^{-2}) of a 2.8 μm TiO_2 nanotube film with C203 dye and solvent free ionic liquid electrolyte. The inset is the photocurrent action spectra of the same DSC device.

7.3 Conclusion

Flexible DSC prepared with TiO_2 nanotube arrays grown on a metallic foil as photoanode and transparent conductive polymer ITO-PEN as counter electrode in combination with ionic liquid electrolyte obtained 3.6 % efficiency at AM 1.5 simulated full sun light. I have shown that the photovoltaic performance of devices depends on the length of nanotube. Flexible ionic liquid electrolyte solar cells will stimulate considerable interests for academic research and practical applications.

In addition, I have shown that TNT array fabricated by anodization of a sputtered Ti/ TiO_2 double layer film on an FTO-coated glass substrate can work efficiently in a ss-DSC. This novel TiO_2 electrode material is well suited for inclusion in ss-DSCs because of its flat and smooth top surface, a critical property that reduces chances of shunt in the cell. Even though the surface area of TiO_2 NT film is shown to be lower than in a comparable mesoporous film, I have shown that this novel ss-DSC morphology can deliver significant performance using a high molar extinction coefficient and IQE molecular dye sensitizer. Using panchromatic dyes with high molar extinction coefficients to absorb even more visible light could further increase

the performance of these cells.

7.4 References

1. O'Regan, B. C. & Graetzel, M. A low-cost, high-efficiency solar cell based on dye-sensitized colloidal TiO₂ films. *Nature* 353, 737–740 (1991).
2. Nazeeruddin, M. K. et al. Combined experimental and DFT-TDDFT computational study of photoelectrochemical cell ruthenium sensitizers. *J Am Chem Soc* 127, 16835–16847 (2005).
3. Zukulová, M. et al. Organized mesoporous TiO₂ films exhibiting greatly enhanced performance in dye-sensitized solar cells. *Nano Lett* 5, 1789–1792 (2005).
4. Adachi, M. et al. Highly Efficient Dye-Sensitized Solar Cells with a Titania Thin-Film Electrode Composed of a Network Structure of Single-Crystal-like TiO₂ Nanowires Made by the “Oriented Attachment” Mechanism. *J Am Chem Soc* 126, 14943–14949 (2004).
5. Law, M., Greene, L., Johnson, J., Saykally, R. & Yang, P. Nanowire dye-sensitized solar cells. *Nat Mater* 4, 455–459 (2005).
6. Zhu, K., Neale, N. R., Miedaner, A. & Frank, A. J. Enhanced Charge-Collection Efficiencies and Light Scattering in Dye-Sensitized Solar Cells Using Oriented TiO₂ Nanotubes Arrays. *Nano Lett* 7, 69–74 (2007).
7. Mor, G. K., Varghese, O. K., Paulose, M., Shankar, K. & Grimes, C. A. A review on highly ordered, vertically oriented TiO₂ nanotube arrays: Fabrication, material properties, and solar energy applications. *Sol Energ Mat Sol C* 90, 2011–2075 (2006).
8. Grimes, C. A. Synthesis and application of highly ordered arrays of TiO₂ nanotubes. *J Mater Chem* 17, 1451 (2007).
9. Miyasaka, T. & Kijitori, Y. Low-temperature fabrication of dye-sensitized plastic electrodes by electrophoretic preparation of mesoporous TiO₂ layers. *J Electrochem Soc* 151, A1767–A1773 (2004).
10. Kang, M., Park, N., Ryu, K., Chang, S. & Kim, K. A 4.2% efficient flexible dye-sensitized TiO₂ solar cells using stainless steel substrate. *Sol Energ Mat Sol C* 90, 574–581 (2006).
11. Dürr, M. et al. Low-temperature fabrication of dye-sensitized solar cells by transfer of composite porous layers. *Nat Mater* 4, 607–611 (2005).
12. Ito, S. et al. High-efficiency (7.2%) flexible dye-sensitized solar cells with Ti-metal substrate for nanocrystalline-TiO₂ photoanode. *Chem. Commun.* 4004–4006 (2006).
13. Kuang, D. et al. Stable, high-efficiency ionic-liquid-based mesoscopic dye-sensitized solar cells. *Small* 3, 2094–2102 (2007).
14. Prakasam, H. E., Shankar, K., Paulose, M., Varghese, O. K. & Grimes, C. A. A new benchmark for TiO₂ nanotube array growth by anodization. *J Phys Chem C* 111, 7235–7241 (2007).
15. Gong, D., Grimes, C. A. & Varghese, O. Titanium oxide nanotube arrays prepared by anodic oxidation. *J Mater Res* 16, 3331–3334 (2001).
16. Macak, J. M., Zlamal, M., Krysa, J. & Schmuki, P. Self-organized TiO₂ nanotube layers as highly efficient photocatalysts. *Small* 3, 300–304 (2007).

17. Kuang, D., Uchida, S., Humphry-Baker, R., Zakeeruddin, S. M. & Graetzel, M. Organic Dye-Sensitized Ionic Liquid Based Solar Cells: Remarkable Enhancement in Performance through Molecular Design of Indoline Sensitizers. *Angew. Chem. Int. Ed.* 47, 1923–1927 (2008).
18. Kuang, D., Wang, P., Ito, S., Zakeeruddin, S. M. & Graetzel, M. Stable Mesoscopic Dye-Sensitized Solar Cells Based on Tetracyanoborate Ionic Liquid Electrolyte. *J Am Chem Soc* 128, 7732–7733 (2006).
19. Varghese, O. K., Gong, D., Paulose, M., Grimes, C. A. & Dickey, E. C. Crystallization and high-temperature structural stability of titanium oxide nanotube arrays. *J Mater Res* 18, 156–165 (2011).
20. Kuang, D. et al. High Molar Extinction Coefficient Heteroleptic Ruthenium Complexes for Thin Film Dye-Sensitized Solar Cells. *J Am Chem Soc* 128, 4146–4154 (2006).
21. Bisquert, J. Theory of the impedance of electron diffusion and recombination in a thin layer. *J. Phys. Chem. B* 106, 325–333 (2002).
22. Wang, Q., Moser, J. & Graetzel, M. Electrochemical impedance spectroscopic analysis of dye-sensitized solar cells. *J. Phys. Chem. B* 109, 14945–14953 (2005).
23. Mor, G. K., Shankar, K., Paulose, M., Varghese, O. K. & Grimes, C. A. Use of highly-ordered TiO₂ nanotube arrays in dye-sensitized solar cells. *Nano Letters* 6, 215–218 (2006).
24. Paulose, M. et al. Backside illuminated dye-sensitized solar cells based on titania nanotube array electrodes. *Nanotechnology* 17, 1446–1448 (2006).
25. Paulose, M., Shankar, K., Varghese, O., Mor, G. & Grimes, C. A. Application of highly-ordered TiO₂ nanotube-arrays in heterojunction dye-sensitized solar cells. *J Phys D Appl Phys* 39, 2498–2503 (2006).
26. Ong, K. G., Varghese, O. K., Mor, G. K., Shankar, K. & Grimes, C. A. Application of finite-difference time domain to dye-sensitized solar cells: The effect of nanotube-array negative electrode dimensions on light absorption. *Sol Energ Mat Sol C* 91, 250–257 (2007).
27. Shankar, K. et al. Highly Efficient Solar Cells using TiO₂ Nanotube Arrays Sensitized with a Donor-Antenna Dye. *Nano Lett* 8, 1654–1659 (2008).
28. Mor, G. K., Shankar, K., Paulose, M., Varghese, O. K. & Grimes, C. A. High efficiency double heterojunction polymer photovoltaic cells using highly ordered TiO₂ nanotube arrays. *Appl Phys Lett* 91, 152111 (2007).
29. Kuang, D. et al. Application of highly ordered TiO₂ nanotube arrays in flexible dye-sensitized solar cells. *ACS nano* 2, 1113–1116 (2008).
30. Sun, W.-T. et al. CdS Quantum Dots Sensitized TiO₂ Nanotube-Array Photoelectrodes. *J Am Chem Soc* 130, 1124–1125 (2008).
31. Kongkanand, A., Tvrđy, K., Takechi, K., Kuno, M. & Kamat, P. V. Quantum dot solar cells. Tuning photoresponse through size and shape control of CdSe-TiO₂ architecture. *J Am Chem Soc* 130, 4007–4015 (2008).
32. Mor, G. K., Prakasam, H. E., Varghese, O. K., Shankar, K. & Grimes, C. A. Vertically oriented Ti-Fe-O nanotube array films: Toward a useful material architecture for solar spectrum water photoelectrolysis. *Nano Lett* 7, 2356–2364 (2007).
33. Mor, G. K. et al. P-type Cu--Ti--O nanotube arrays and their use in self-biased

- heterojunction photoelectrochemical diodes for hydrogen generation. *Nano Lett* 8, 1906–1911 (2008).
34. Mor, G. K., Varghese, O. K., Paulose, M. & Grimes, C. A. Transparent Highly Ordered TiO₂ Nanotube Arrays via Anodization of Titanium Thin Films. *Adv Funct Mater* 15, 1291–1296 (2005).
 35. Macak, J., Tsuchiya, H. & Schmuki, P. High-Aspect-Ratio TiO₂ Nanotubes by Anodization of Titanium. *Angew. Chem. Int. Ed.* 44, 2100–2102 (2005).
 36. Macak, J. M. et al. TiO₂ nanotubes: Self-organized electrochemical formation, properties and applications. *Curr Opin Solid St M* 11, 3–18 (2007).
 37. Chanmanee, W. et al. Formation and Characterization of Self-Organized TiO₂ Nanotube Arrays by Pulse Anodization. *J Am Chem Soc* 130, 965–974 (2008).
 38. Albu, S., Kim, D. & Schmuki, P. Growth of Aligned TiO₂ Bamboo-Type Nanotubes and Highly Ordered Nanolace. *Angew. Chem. Int. Ed.* 120, 1943–1945 (2008).
 39. Fabregat-Santiago, F. et al. High carrier density and capacitance in TiO₂ nanotube arrays induced by electrochemical doping. *J Am Chem Soc* 130, 11312–11316 (2008).
 40. Jennings, J. R., Ghicov, A., Peter, L. M., Schmuki, P. & Walker, A. B. Dye-Sensitized Solar Cells Based on Oriented TiO₂ Nanotube Arrays: Transport, Trapping, and Transfer of Electrons. *J Am Chem Soc* 130, 13364–13372 (2008).
 41. Qin, H. et al. An organic sensitizer with a fused dithienothiophene unit for efficient and stable dye-sensitized solar cells. *J Am Chem Soc* 130, 9202–+ (2008).
 42. Snaith, H. J. et al. Charge collection and pore filling in solid-state dye-sensitized solar cells. *Nanotechnology* 19, – (2008).
 43. Snaith, H. J. et al. Efficiency Enhancements in Solid-State Hybrid Solar Cells via Reduced Charge Recombination and Increased Light Capture. *Nano Lett* 7, 3372–3376 (2007).

Chapter 8. Three-dimensional titania nanostructures for fast charge extraction

This chapter is adapted from peer-reviewed publications by Nicolas Tétreault, Jérémie Brillet et al. published in 2011 in Nano Letters, 11 (11), pp 4579–4584 and in ACS Nano, 4 (12), pp 7644–7650 in 2011.

8.1 Improved charge dynamics through a 3D host-passivation-guest electrode

8.1.1 Motivations

In the past, efforts have been put into ZnO and SnO₂ as alternatives to TiO₂ in DSCs due to their higher electronic conductivity and electron mobility when compared to TiO₂.¹ Despite faster electron transport,¹ only rather poor device efficiencies have been reported to date for DSCs employing nanocrystalline SnO₂.²⁻⁶ In part, this was found to be due to a two to three orders of magnitude increase in the recombination rates when the high mobility material is in direct contact with the sensitizer and/or the electrolyte.¹ This has triggered research on the addition of blocking (passivating) layers covering the ZnO or SnO₂ in order to reduce this recombination rate resulting in higher photovoltage.^{2,7,8}

Herein, I report on a novel bottom-up 3D host-passivation-guest (H-P-G) electrode concept that enables structural control on the electron extraction,

conduction band, and the recombination dynamics as well as on the optical scattering in photovoltaic devices. This new type of electrode is exemplified herein by incorporating it into a DSC photoanode to significantly improve photocurrent, fill factor, and most importantly the photovoltage. This is shown through a strong decrease in dark current when comparing a 3D TiO₂ host to high electron mobility Al:ZnO and SnO₂ hosts. To ensure high dye loading, the macropores contained in the passivated 3D host are infiltrated with anatase TiO₂ nanoparticles to form a conformal mesoporous film enabling optimized sensitization and electron injection characteristics found in traditional nanoparticle-based DSCs. Using this novel architecture, an increase in the photovoltage of up to 110 mV over state-of-the-art TiO₂, ZnO, and SnO₂-based DSCs is obtained. The straightforward and simple bottom-up fabrication technique produces a highly optically scattering photoanode that could enable enhanced light harvesting,⁹ fast charge extraction, reduced interfacial recombination, and lower IR loss to significantly increase the cell photovoltage, photocurrent, and the fill factor.¹⁰ The concept electrode is well suited for DSCs since only a small volume fraction is lost to the optically inactive 3D host material leaving most of the volume for the light harvesting sensitized nanoparticle TiO₂ mesoporous film.

8.1.2 Tailoring a H-P-G photoanode

A schematic representation of the intermediate materials involved in the fabrication of a 3D H-P-G photoanode for DSCs is shown in Figure 8.1. The overall fabrication method is inspired by micromolding in inverse opals (MISO) first developed for the synthesis of large-area oxide inverse opals and then extended for high-temperature fabrication of full-photonic bandgap semiconductor photonic crystals from polymer templates.^{11,12} A dispersion of polystyrene microspheres in isopropanol is used to obtain a highly disordered opal template of uniform thickness. Using large monodispersed spheres enables the formation of a uniform template with predictably large interconnecting pores extending in all three spatial dimensions. The thickness of the template is adjusted through the volume concentration of spheres in the isopropanol dispersion (22 vol.% for 10–12 μm thick template film). The dispersion is then doctor bladed, a scalable fabrication technique, on a transparent

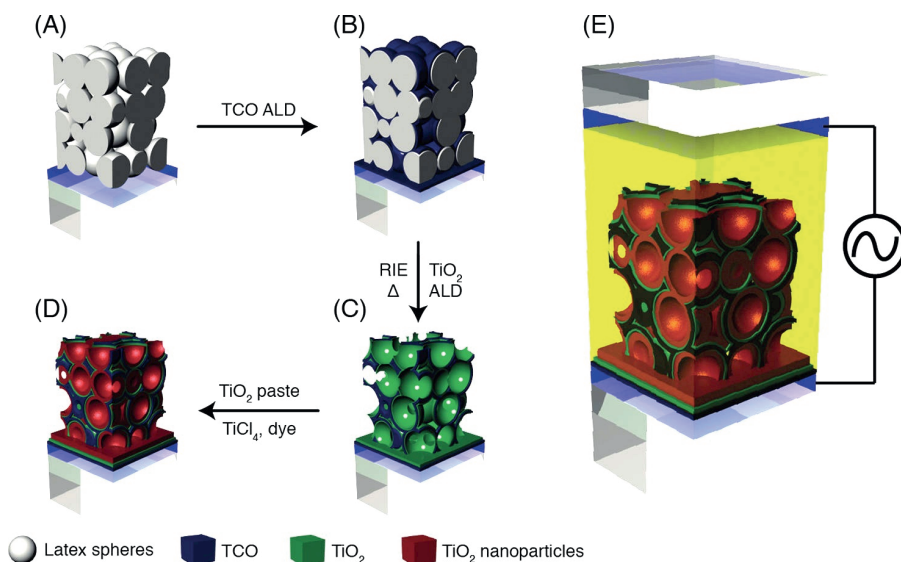


Figure 8.1: Schematic representation of the synthesis method for a 3D host-passivation-guest DSC. (A) Doctor-bladed, disordered template of 2.2 μm polystyrene spheres. (B) Layer-by-layer conformal deposition of the host material (Al:ZnO, TiO₂) by ALD. (C) After RIE to open the top surface, the template is removed by annealing at 360 °C to reveal a disordered inverse opal of host material. It is then conformally coated with 25 nm of dense TiO₂ by ALD. (D) Pore filling with high surface area nanocrystalline TiO₂ and dye loading. (E) Liquid electrolyte infiltration and sealing of the dye sensitized solar cell.

conductive FTO-covered glass substrate to reveal a large-area highly light scattering disordered template (Figure 8.1a). It is then heated and infiltrated with 90 nm of Al/ZnO (1:9), SnO₂, or TiO₂ in a highly conformal fashion by atomic layer deposition (ALD) (Figure 8.1b). Recently ALD has been gaining interest as a powerful research tool for creating highly conformal layers on nanostructured electrodes¹³ and has even been used for surface state passivation of TiO₂ in dye sensitized solar cells¹⁴ and Fe₂O₃ for water photolysis.¹⁵ The deposition temperature is optimized to increase the template interconnecting pore size by softening of the polymer beads ensuring proper sphere necking.¹⁶ Large interconnecting pores between spheres will enable proper filling with the guest nanocrystalline TiO₂ later on. A quick dry reactive ion etching (RIE) of the infiltrated opal's top surface oxide is performed before removing the polymer template by annealing (360 °C, 15 min.) We thus obtain a 3D host backbone that is well connected to the underlying FTO-glass front electrode. The direct electronic connection will ensure efficient charge extraction throughout the interconnected 3D H-P-G electrode. The surfaces of the TCO backbone are then conformally coated with 25 nm of dense TiO₂ by ALD in order to reduce interfacial recombination between electrons in the highly conducting TCO backbone and the I₃⁻ oxidized electrolyte (Figure 8.1c).¹ After calcination (500 °C, 15 min.) the hexagonal

wurtzite, cassiterite, and anatase crystal structures of the Al:ZnO, SnO₂, and TiO₂, respectively, were confirmed by powder X-ray diffraction (data not shown). In order to provide enough surface area for dye sensitization and efficient light harvesting, the macroporous inverse TCO backbone is infiltrated by sequential doctor-blading of a low viscosity 17 nm anatase nanocrystal paste (Figure 8.1d).

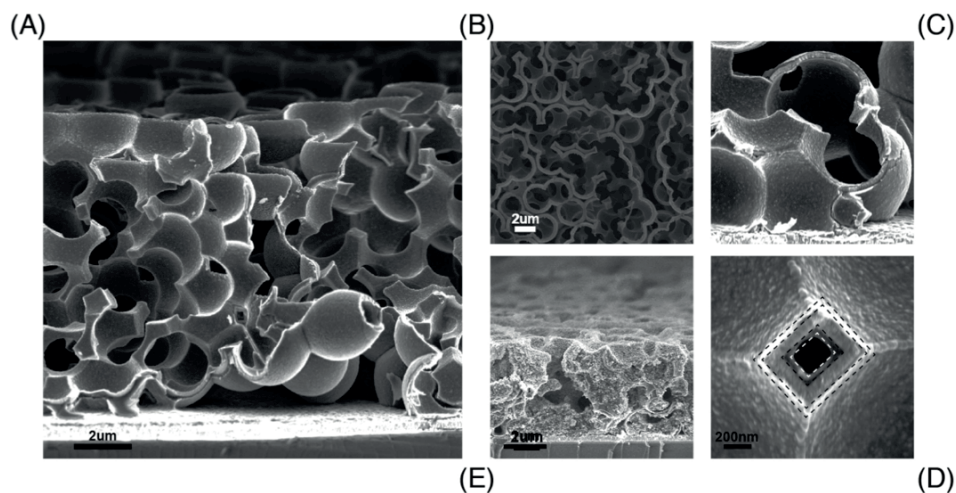


Figure 8.2 : Scanning electron micrograph of a self-assembled 3D Al/ZnO |TiO₂| host-guest dyes-sensitized solar cell photoanode. (A) Cross-sectional view of a disordered TiO₂ passivated 3D Al/ZnO backbone. (B) Top-view of the 3D macroporous Al/ZnO after top surface removal by reactive ion etching and template removal by annealing. (C) High-magnification micrograph showing the TiO₂ covered 3D macroporous Al/ZnO host in direct contact with the front FTO electrode. (D) High-magnification micrograph showing the 3D Al/ZnO conformally coated with a 25 nm thin film of dense TiO₂ inside and out. (E) Complete photoanode after infiltration and calcination of the TiO₂ nanoparticle paste.

Scanning electron micrographs (SEM) of a 3D Al:ZnO |TiO₂| anatase nanoparticles H-P-G photoanode are presented in Figure 8.2. The cross-sectional and top view (Al:ZnO host) micrographs (Figure 8.2a,b) clearly show the high pore connectivity throughout the 3D open structure as well as the significant disorder inherited from the polystyrene template. From these micrographs, we can conclude that the backbone only uses a small volume fraction of the 3D film (10%). This is an additional advantage of the 3D macroporous structure where the high degree of necking between the templating spheres and the very thin (90 nm) film of metal oxide host deposited leave the vast majority of the volume for filling with the guest material. The macroporous structure further enables the conformal coating of the 3D host on both sides with dense TiO₂ by ALD (Figure 8.2c,d). The role of the TiO₂ overlayer is to passivate the TCO surface to improve its chemical stability and further reduce recombination rate at the conductive transparent oxide - electrolyte interface. Visible

in Figure 8.2c is the direct contact between the 3D host and the FTO–glass that will ensure unhindered electron transfer from the 3D host–guest structure and the front DSC electrode. Additionally, subsequent TiO_2 deposition was found to cover the FTO in addition to the 3D host to effectively block recombination at the FTO–electrolyte interface. Figure 8.2e shows the 3D Al:ZnO | TiO_2 | anatase nanoparticles H-P-G electrode after partial filling with mesoporous anatase to constitute the finished 3D TCO photoanode. We estimate from SEM pictures that about 50% on the internal volume is filled with the anatase TiO_2 nanoparticles.

8.1.3 H-P-G photoanode in DSCs

8.1.3.1 Methods

Complete DSC devices were prepared using 10–12 μm thick 3D TiO_2 | TiO_2 | anatase nanoparticles, Al:ZnO | TiO_2 | anatase nanoparticles and SnO_2 | TiO_2 | anatase nanoparticles H-P-G photoanodes on a FTO–glass substrate. In both cases, 90 nm of the host and 25 nm of TiO_2 were deposited by ALD for a maximum wall thickness of 140 nm. Individual infiltrations were separated by 10 min heating at 120 °C to ensure solvent evaporation and densification of the conformal paste thin film. The electrode is then calcined to burn off the organic materials found in the paste (500 °C, 60 min, 2 °C/min ramp).¹⁷ In order to improve the anatase nanoparticle connectivity and increase the photocurrent, the TiO_2 and SnO_2 H-P-G photoanodes were immersed into a 40 mM aqueous TiCl_4 solution at 70 °C for 30 min and washed with water and ethanol.¹⁷ This treatment could not be done on the Al:ZnO-based electrode since it is not chemically stable enough to sustain immersion in strong acid at elevated temperature. We should thus expect a penalty on the photocurrent for this photoanode.

The films are sintered for 30 min at 500 °C before dipping in a 0.3 mM Z907 solution for 10 min. Following the immersion procedure, the dye-sensitized electrodes were rinsed with acetonitrile and dried in air. The photoanodes are then assembled using a thermally platinized FTO (TEC15) counter electrode using a 25 μm thick hot melt ring and sealed by heating. The cell internal space was filled with a I_3^-/I^- electrolyte in a 85:15 acetonitrile/valeronitrile mixture. Detailed procedure for the photoanode preparation and DSC assembly can be found in Annex D.

8.1.3.2 Device performances

Shown in Figure 8.3a are the J - V characteristics for the DSCs based on TiO_2 , SnO_2 , and Al:ZnO 3D host photoanodes. I found an increase in short-circuit current density going from a TiO_2 ($J_{sc} = 6.9 \text{ mA.cm}^{-2}$) to Al/ZnO ($J_{sc} = 7.9 \text{ mA.cm}^{-2}$) and SnO_2 ($J_{sc} = 10.4 \text{ mA.cm}^{-2}$). The absence of TiCl_4 treatment could explain the lower photocurrent for the Al:ZnO host as this treatment enhances connectivity between anatase TiO_2 nanoparticles to significantly increase the photocurrent and photovoltage in state-of-the-art DSCs by improving electron hopping at the anatase nanoparticle boundaries.¹⁸ It is possible that the increase in photocurrent observed is a direct consequence of the high electron mobility in the Al:ZnO and SnO_2 hosts (241 and $16.5 \text{ cm}^2.(\text{V s})^{-1}$, respectively), which is five to six orders of magnitude higher than measured for anatase TiO_2 nanoparticles at high voltage ($V = 0.8 \text{ V}$, $2.30 \times 10^{-4} \text{ cm}^2.(\text{V s})^{-1}$) as shown in table 8.1.

Table 8.1 : Table of the electron mobilities and diffusion coefficients for TiO_2 nanoparticle film and Al:ZnO and SnO_2 ALD films annealed at 500°C .

Material	Mobility (cm^2 / Vs)	Diffusion coefficient (cm^2 / s)
TiO_2 NP	2.30×10^{-4}	6.00×10^{-6}
Al:ZnO	241	6.19
SnO_2	16.5	0.423

In addition, the fill factor is found to be greater for the Al:ZnO ($\mathcal{f} = 0.77$) host than for the TiO_2 ($\mathcal{f} = 0.73$) host. Regardless of the host material, the 3D H-P-G photoanodes all present photovoltages well above the $V_{oc} = 730 \text{ mV}$ obtained with the best performing Z907 DSCs.¹⁹ Indeed, an improvement of 60 and 110 mV for TiO_2 ($V_{oc} = 791 \text{ mV}$) and Al:ZnO ($V_{oc} = 842 \text{ mV}$) hosts are obtained, respectively. A significant increase in photovoltage is to be expected when reducing the dark current, which depends on the conduction band position and recombination dynamics in the cell. Indeed, a significant decrease in the dark current is observed going from the TiO_2 to the Al:ZnO host as can be seen in Figure 8.3b.

When compared to previous studies using high mobility materials like SnO_2 and ZnO passivated with TiO_2 in liquid electrolyte DSCs we find that the photovoltage obtained with the 3D host-guest photoanodes are higher by at least 90–100 mV.²⁻⁶ Additionally, an increase of about 60 and 110 mV over our published

state-of-the-art values for Z907 dye and iodine-based volatile electrolyte is obtained for 3D TiO₂ and Al:ZnO hosts, respectively. One of the major advantages in using transparent high mobility materials, for example, ZnO and SnO₂, for charge injection and collection in DSCs lies in its relatively low transport resistance when compared to that of anatase TiO₂ nanoparticles.^{20,21} However, this advantage was found to be counterbalanced by faster electron recombination dynamics with the oxidized electrolyte via intrabandgap surface states ultimately limiting the efficiency of such cells. This led to the study of various capping materials (Al₂O₃, TiO₂, MgO, etc.) that slow down recombination leading to increases in photocurrent and photovoltage.^{2,7,8} In addition to acting as an effective protection layer for the chemically unstable ZnO against the acidic dye solution,²² the complete coverage of the host material with ALD of a dense 25 nm TiO₂ layer can passivate surface traps¹⁵ and increase charge transfer resistance to the oxidized dye and electrolyte.

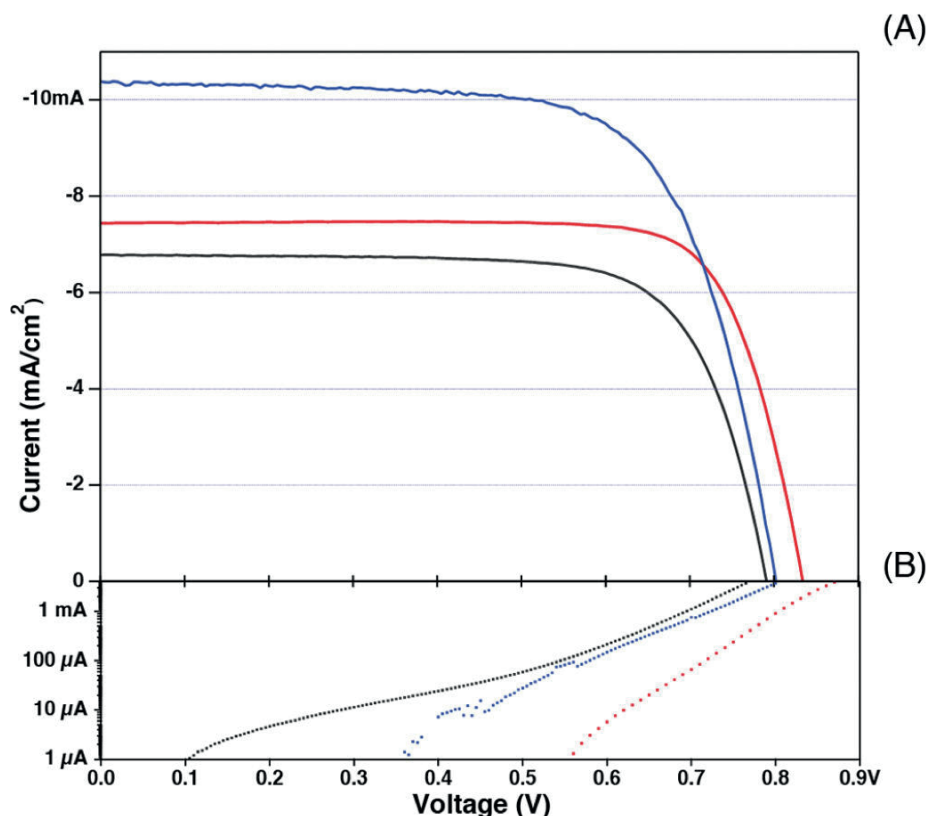


Figure 8.3: Photocurrent density-voltage (J - V) characteristics of the 3D host-passivation-guest dye-sensitized solar cells under AM 1.5 illumination and in the dark. Solid (A) and dashed (B) lines represent the current under standard illumination and in the dark, respectively, for Al/ZnO (red, $J_{sc} = 7.5 \text{ mA}\cdot\text{cm}^{-2}$, $V_{oc} = 842 \text{ mV}$, $ff = 0.77$, $\eta = 4.9\%$), SnO₂ (blue, $J_{sc} = 10.4 \text{ mA}\cdot\text{cm}^{-2}$, $V_{oc} = 803 \text{ mV}$, $ff = 0.70$, $\eta = 5.8\%$) and TiO₂ (black, $J_{sc} = 6.9 \text{ mA}\cdot\text{cm}^{-2}$, $V_{oc} = 791 \text{ mV}$, $ff = 0.73$, $\eta = 4.0\%$) hosts.

This is clearly visible in the decrease in dark current observed (Figure 8.3b).

According to the literature, this can be due to a decrease in recombination or a shift of the conduction band towards vacuum.²³ Both would lead to a shift in the quasi-Fermi level with respect to the redox potential of the electrolyte and contribute to the significant increase in the observed photovoltage.² These findings will motivate further mechanistic studies on the role of the various interfaces, conduction pathways, and electronic properties of the various materials that could induce band bending, affect injection dynamics, or shift the conduction band position.

8.2 Fast charge extraction through a 3D Fibrous Network of Crystalline TiO₂ Nanowires in a Solid State DSC

8.2.1 Motivations

DSCs are one of the most promising photovoltaic technologies for production of renewable, clean, and affordable energy. Liquid electrolyte-based DSCs have reached efficiencies as high as 11.1%.^{9,24,25} However, these liquid-based DSCs may suffer from potential leakage and corrosion problems;^{26,27} the potential disadvantages have sparked research in DSCs that have solid-state hole transport materials (HTMs) instead of liquid electrolytes. One of the most widely used HTMs is spiro-MeOTAD (2,2',7,7'-tetrakis-(N,N-di-p-methoxyphenylamine)9,9'-spirobifluorene).²⁸ Devices with spiro-MeOTAD as HTM have already attained efficiencies over 5%,^{29,30} which is still below the efficiency of liquid electrolyte DSCs. The lower efficiency is primarily a consequence of incomplete light harvesting. Indeed, high-performance solid-state DSCs (ss-DSCs) are still limited to a 2–3 μm thick active layer that is far thinner than needed to achieve good optical absorption for most of the currently used sensitizers.³¹ There are two factors that limit the ss-DSCs from being more efficient at a thickness of >2 μm: incomplete filling of the mesoporous TiO₂ films with spiro-MeOTAD and electron–hole recombination. Studies show that recombination is 2 orders of magnitude faster and electron diffusion length is 1 order of magnitude lower in ss-DSCs than in liquid DSCs.³²⁻³⁵ Pore filling has been the focus of a thorough study that linked the cell efficiency and optimal thickness to the pore filling by way of varying the spinning speed and concentration of spiro-MeOTAD in the infiltrating solution.³⁶ However, the optimal thickness remained below 3 μm.

Electron transport in DSCs is governed by an ambipolar diffusion mechanism controlled by trap-limited hopping through a relatively long and tortuous path to the transparent substrate.³⁷⁻³⁹ Given a charge collection time of milliseconds at the maximum power point,⁴⁰ efficient charge extraction is only made possible through the extraordinarily slow interception of electrons by adjacent I_3^- . However, this recombination pathway is 2 orders of magnitude faster in ss-DSCs, which makes it one of the main limiting factors in their efficiency. Several approaches have been proposed in order to improve charge collection in liquid electrolyte and ss-DSCs including the use of radial collection nanostructures² and one-dimensional ZnO and TiO₂ nanorods and nanowires as photoanodes.^{3,41-43} Even though these approaches show great promise, they have yet to achieve power conversion efficiencies above 5% in liquid electrolyte DSCs and 1.7% in ss-DSCs.

One of the major issues with these novel photoanodes is their limited roughness factor which greatly limits dye loading and, ultimately, absorption and photocurrent. In liquid DSCs, improved light harvesting has been demonstrated using backscattering overlayer,⁴⁴ mesoporous macroparticles,⁴⁵ mixtures of macroparticles and nanoparticles,⁹ as well as photonic crystals.⁴⁶⁻⁴⁸ However, the limited thickness in ss-DSCs prohibits the use of these different strategies and necessitates the development of thin-film electrodes that are inherently diffusive.

8.2.2 *Anatase nanowires*

In this sub-chapter, I present the first high-efficiency ss-DSC built using a three-dimensional (3D) fibrous network of anatase nanowires self-assembled from fused single-crystal nanorods. This novel photoanode material is the first to incorporate a high-conductivity network for efficient electron extraction, a relatively high roughness factor for dye loading, and large pores for enhanced light harvesting through light scattering. From high-resolution scanning and transmission electron microscopy (HRSEM and TEM), it is found that the 3D fibrous network is formed of primary TiO₂ nanorods that self-assemble into interconnected single-crystalline nanowires. This morphology offers large pores that efficiently scatter light to enhance light harvesting and a high roughness factor of 144 that permits adequate dye loading. A detailed study using electrochemical impedance spectroscopy (EIS) shows that this 3D morphology presents a significantly higher conductivity over a wide range of

applied potential as well as faster electron transport than comparable nanoparticle-based ss-DSCs which result in improved collection efficiencies. Using a state-of-the-art organic dye,⁴⁹ these factors combine to achieve the highest reported power conversion efficiency in a nanowire-based solid-state device of 4.9% under AM1.5. This result puts this novel morphology in direct competition with conventional nanoparticle-based ss-DSCs, which until recently were capable of achieving only slightly higher power conversions than 5% (AM1.5).^{29,30}

The primary building block of this 3D fibrous network is the single-crystal nanorod. These subparticles are obtained from the thermal decomposition of titanate nanowires between 20 and 60 nm in diameter and 1 and 20 μm in length. A detailed procedure for the synthesis of this material is available in Appendix D. In short, nanowires are produced by a two-step hydrothermal process. In a typical synthesis, a mixture of anatase and NaOH solution is treated at 130 °C for 36 h. The resulting white powder undergoes a second hydrothermal treatment at 200 °C while mixed with KOH. The obtained nanowires are subsequently collected, washed, and dried at 250 °C. In order to produce a solution for doctor blading that would both exhibit good wettability on FTO glass substrate and produce smooth thin films, the nanowires are sonicated in isopropyl alcohol for 30 min. The nanowire solution of 24 mg/mL in isopropyl alcohol is then doctor bladed using a 40 μm spacer (3M) to obtain the desired film thickness of 2.5 μm .

The nanowires go through an oriented attachment growth mechanism to form a 3D network of nanorods.⁵⁰ At first, nanowires self-assemble in two dimensions parallel to the FTO glass substrate during the doctor blading process. The network consequently condenses during the evaporation of isopropyl alcohol, enhancing the number of contact points between the individual nanowires (Figure 8.4a). During the subsequent thermal decomposition, each titanate nanowire undergoes a transformation into chain-like assembly of truncated anatase nanorods (Figure 8.4b,c).⁵¹ Figure 8.4c,d shows high-resolution TEM images of the interconnected TiO_2 nanorods elongated in the [001] direction. All images clearly show single-crystalline nanorods with lattice fringes of the (101) plane obtained. The analysis of the interface between two attached nanorods reveals reduced lattice fringes' misorientation through grain boundaries from one particle to the next, confirming the topotactic transformation of the nanowires.⁵² Oriented attachment also occurs

spontaneously at the contact point between nanowires to yield a stabilized 3D network of nanorods with enhanced grain boundaries.⁵⁰ The crystal structure of the 3D network of nanorods is confirmed by the XRD peak positions obtained which are consistent with the standard powder diffraction pattern of the pure anatase phase of TiO_2 (JCPDF 21-1272) with no secondary phase or rutile formation observed. An averaged primary crystallite size of 13.6 nm is predicted from the full width at half-maximum value of the (101) XRD peak using Scherrer's equation. This is in good agreement with the average nanorod diameter obtained by analyzing TEM images.

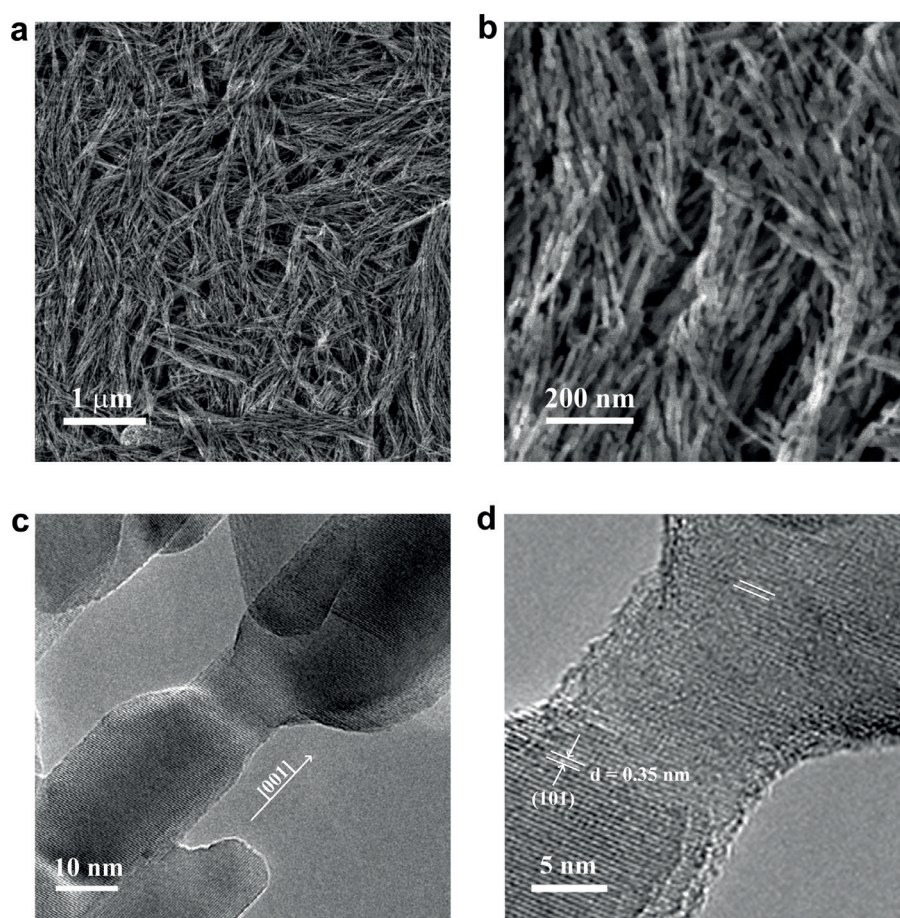


Figure 8.4 : Oriented attachment of nanorods into a 3D fibrous network of single-crystalline anatase nanowires. (a) High-resolution scanning electron micrograph of the top surface showing nanowire aggregates and the macroporous structure. (b) Oriented self-assembly of the nanorods into the 3D fibrous network. (c) High-resolution transmission electron micrograph showing the continuous [001] crystal orientation across two nanorods. (d) Continuous (101) crystal plane and spacing across the junction.

Using a nitrogen adsorption–desorption technique, the specific surface area, pore diameter, and pore volume for the fibrous anatase network are compared with that of conventional films obtained from a 23 nm anatase nanoparticles paste prepared in-house (Figure 8.5a).⁵³ Conventional films offer a narrow pore size

distribution in the mesoporous regime ranging from 4 to 18 nm, while the average pore size is centered at 13 nm and the corresponding total pore volume is about 0.3 cm³/g. By comparison, the 3D network of nanorods exhibits a wide pore size distribution composed of large 10–50 nm mesopores and 50–120 nm macropores. The films' porosity is about 40% higher than that of conventional films resulting in almost double the total volume of pores (0.58 cm³.g⁻¹) with the majority (75%) of these pores being larger than 50 nm. This is the result of low packing density of the nanowires due to their large anisotropy and allows for efficient infiltration with the HTMs. In fact, the observed hysteresis in the pressure isotherm shows a H3 feature generally associated with aggregates of thin, flaky particles giving rise to slit-shaped pores. Finally, nanorod and nanoparticle-based films exhibit a BET surface area of 60 and 83 m².g⁻¹, respectively. Although the 144 roughness factor of the 3D architecture of nanorods developed in this study is higher than in previous nanowire-based ss-DSCs, it remains lower than the 374 roughness factor of conventional films. Consequently, the dye loading is reduced and would greatly limit light harvesting if it occurred in transparent, nanoparticle-based films.

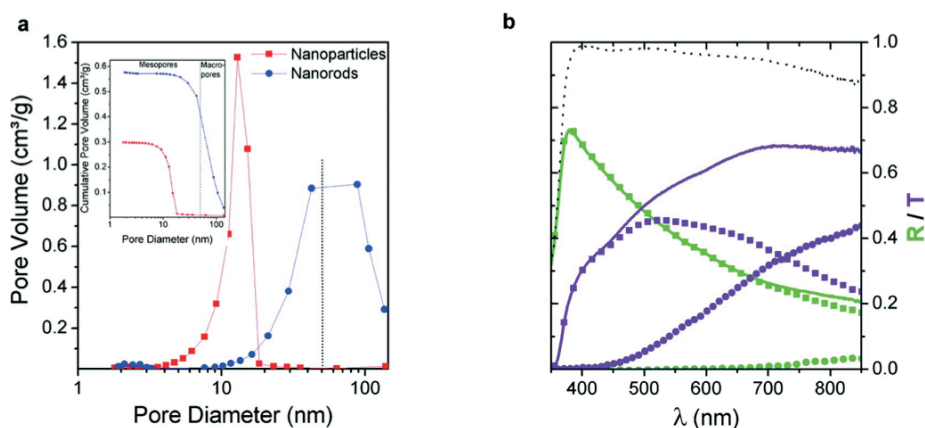


Figure 8.5 : Physical and optical properties of the 3D fibrous network electrode. (a) Comparison of the pore volume and diameter for thin-film electrode made of conventional 23 nm anatase nanoparticles (red) and the 3D fibrous network of anatase nanowires (blue). (b) Total transmittance (purple, solid) and reflectance (green, solid) in a 2.5 μm thick 3D fibrous network thin film on FTO glass substrate including the specular (round dots) and diffused (square dots) contributions. Black dotted line represents the total amount of light measured.

However, lower dye loading in the 3D network film is partly compensated by significant light scattering in the film. Indeed, Chiba *et al.* have shown that efficient light scattering significantly increases light harvesting in the DSC and, consequently, its photocurrent.⁹ In the nanowire-based photoanode, the aggregation mechanism

provides for both large aggregates and macropores (Figure 8.4a) capable of effective light scattering, as can be seen in Figure 8.5b. About 20–40% of visible light is scattered in transmission and reflection for 2.5 μm thick films.

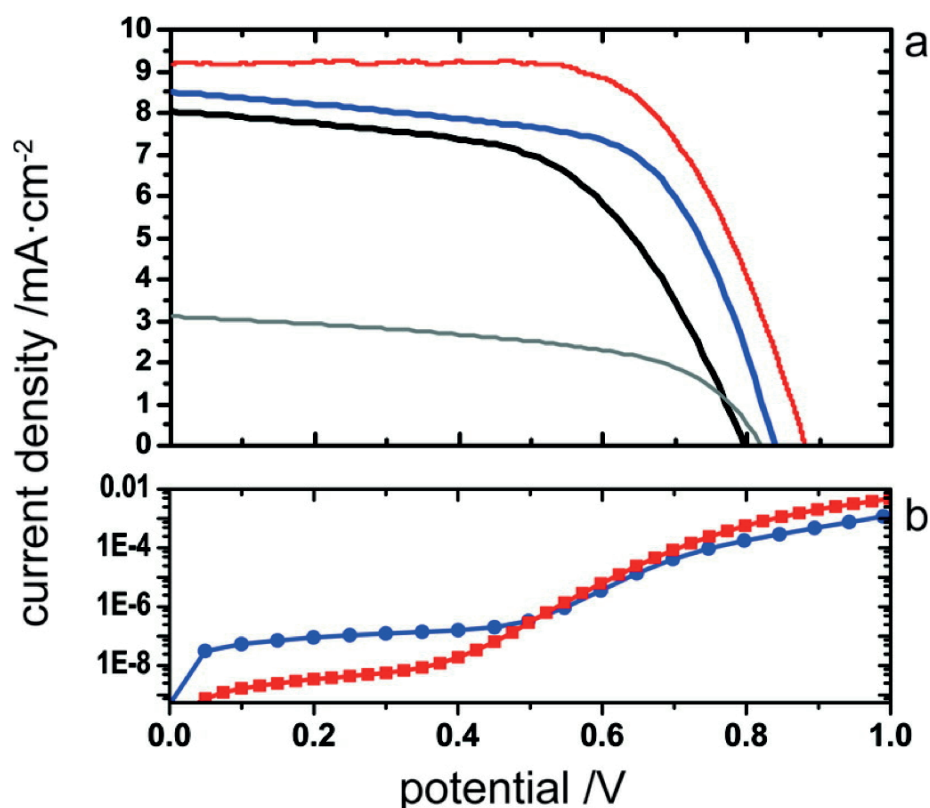


Figure 8.6 : Photocurrent density–voltage (J – V) characteristics of the 3D fibrous network and nanoparticle-based ss-DSCs. (a) J – V characteristics for the as-prepared (gray, $J_{sc} = 3.1 \text{ mA}\cdot\text{cm}^{-2}$, $V_{oc} = 820 \text{ mV}$, $ff = 0.55$, $\eta = 1.5\%$), TiCl_4 -treated (black, $J_{sc} = 8.0 \text{ mA}\cdot\text{cm}^{-2}$, $V_{oc} = 795 \text{ mV}$, $ff = 0.56$, $\eta = 3.9\%$), ALD-treated electrodes (blue, $J_{sc} = 8.50 \text{ mA}\cdot\text{cm}^{-2}$, $V_{oc} = 838 \text{ mV}$, $ff = 0.63$, $\eta = 4.9\%$), and TiCl_4 -treated nanoparticle-based cell (red, $J_{sc} = 9.1 \text{ mA}\cdot\text{cm}^{-2}$, $V_{oc} = 881 \text{ mV}$, $ff = 0.67$, $\eta = 5.4\%$). (b) Comparison of the dark current for a conventional nanoparticle film (red) and the 3D fibrous network film (blue).

Complete DSC devices were prepared using 2.5 μm doctor bladed thin films on FTO glass. After calcination in air at 600 $^\circ\text{C}$ for 2 h, the thin film is dipped overnight in an acetonitrile solution of C218 high extinction coefficient organic dye.⁴⁹ The thin film is then ready to be infiltrated with a solution of spiro-MeOTAD hole transport material, tert-butyl pyridine, and lithium bis(trifluoromethylsulfonyl)imide salt in chlorobenzene. To do so, each film is covered by a small quantity (50–70 μL) of the spiro-MeOTAD solution before spin coating at 1200 rpm for 45 s in order to maximize pore filling.³⁶ After spin coating, a 100 nm gold counter electrode was applied by thermal. Figure 8.6 shows the J – V for the bare 3D fibrous network ss-DSCs as well as for cells which have been treated in aqueous acidic TiCl_4 or by

atomic layer deposition (ALD) of TiO_2 (<1 nm) to improve interconnectivity.

The photocurrent for the bare nanowire-based thin film is significantly increased from 3.1 to 8.0 and 8.5 $\text{mA}\cdot\text{cm}^{-2}$ for the TiCl_4 and ALD-treated films, respectively. This increase results from an improved connectivity between the nanorods' aggregates. Additionally, ALD-treated films present a slightly improved fill factor and photovoltage ($ff = 0.63$, $V_{oc} = 838$ mV) when compared to the bare and TiCl_4 -treated film ($ff = 0.56$, $V_{oc} = 795$ mV). Further investigations are ongoing in order to better understand the slight advantage of ALD deposition versus the conventional TiCl_4 treatment for 3D fibrous network-based ss-DSCs. Figure 8.6b shows the characteristic dark shunt resistance is visible in the $J-V$ curves of the different cells which is due to nanorods sticking through the thin spiro-MeOTAD overlayer and contacting the gold counter electrode. This contributes to a slightly lower than expected fill factor when compared to that of conventional nanoparticle ss-DSCs which is closer to $ff \approx 0.70$.³⁰ Finally, the 3D single-crystalline network of anatase nanorods gives an overall power conversion efficiency of 4.9% which is close to the published efficiency record of 5% for a solid-state spiro-MeOTAD DSC.³⁰

In this work, the electrical behavior of the 3D fibrous network spiro-MeOTAD-based ss-DSCs was studied by electrochemical impedance spectroscopy. The impedance spectra were analyzed using the transmission line model.^{32,54-56} One advantage of this method is that it enables the direct comparison of electronic parameters like conductivity of the TiO_2 , transport time, and lifetime of electrons in conventional nanoparticle-based films and in the 3D fibrous network ss-DSCs. In particular, the latter is compared to a nanoparticle-based cell sensitized with the same C218 dye and with very similar photovoltaic performances ($ff = 0.69$, $V_{oc} = 810$ mV, $J_{sc} = 8.2$ $\text{mA}\cdot\text{cm}^{-2}$, $\eta = 5.4\%$). In order to prevent the light-induced variation of the spiro-MeOTAD doping level during impedance measurements, all parameters presented were obtained in the dark.

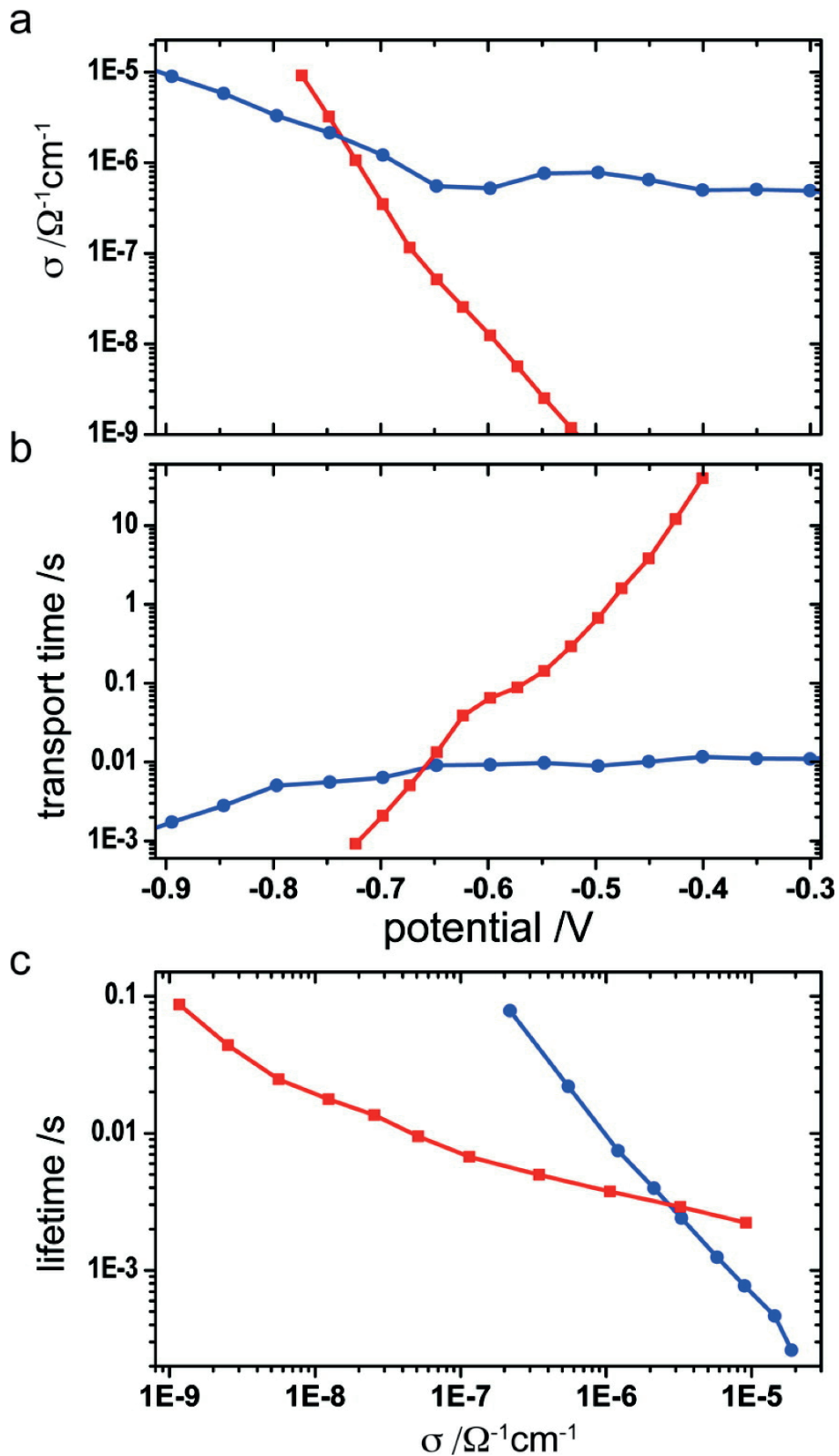


Figure 8.7: Electrochemical impedance spectroscopy in the dark. (a) Comparison of the conductivity in ss-DSCs made with conventional nanoparticles (red) and with the 3D fibrous network (blue). (b) Comparison of the transport time and (c) of the electron lifetime in the same respective ss-DSCs.

First, it can be seen that the conductivity of the 3D fibrous network is higher than its nanoparticle counterpart up to about 750 mV (Figure 8.7a). The conductivity of the fibrous network stays constant over a wide range of applied potential. This indicates a high doping density which is most probably caused by hydrogen intercalation during the nanowire synthesis.⁵⁷ The higher doping level was determined by the Mott–Schottky plots, which confirmed up to an order of magnitude higher charge carrier concentration in the 3D fibrous network and a shift of the flat band potential to higher forward bias.⁵⁸ Likewise, the transport time in the 3D fibrous network can be up to several orders of magnitude shorter than that in the nanoparticle-based film, especially at lower bias potentials (Figure 8.7b). This result clearly confirms that the nanowires have an advantage in electron transport when compared to a conventional nanoparticle film. This is in part the result of the higher doping density in the films, but it is also most probably due to the longer diffusion length of the electron before having to hop on another nanowire.⁵⁹ Finally, the comparison of the electron lifetime shows the same tendency (Figure 8.7c). At low potentials (or low TiO₂ conductivity), the 3D fibrous network ss-DSC shows a longer lifetime than that measured in the nanoparticle-based cell. At 750–800 mV (or $3 \times 10^{-6} \Omega^{-1} \cdot \text{cm}^{-1}$), the electron lifetime in the 3D fibrous network drops below that measured in the nanoparticle-based ss-DSCs. These measurements confirm the high quality of the anatase fibrous network in terms of crystallinity and electronic properties. The superior light scattering as well as the shorter transport time and longer electron lifetime at the maximum power point contribute to a higher photocurrent and charge collection efficiency in the ss-DSC. These favorable optical and electronic characteristics help explain the high-power conversion efficiency obtained with this novel morphology in spite of the lower dye loading.

8.3 Conclusion

In this chapter, I show a novel bottom-up 3D H-P-G DSC photoanode made of a high electron mobility host, a passivating conformal blocking layer and a high surface area guest to improve short circuit current density, fill factor, and photovoltage. The 3D H-P-G photoanode exhibits a strong decrease in dark current when using Al:ZnO with electron mobility and diffusion coefficient up to 6 orders of magnitude higher than that of anatase TiO₂ nanoparticles. By completely covering the 3D host with a dense passivating TiO₂ thin film and filling its macropores with

anatase nanoparticles, we ensure a high surface area for dye loading and maintain injection dynamics typical of anatase nanoparticle-based DSCs. Using this novel 3D H-P-G morphology partially filled with anatase nanoparticles, we show an increase in photovoltage of up to 110 mV over state-of-the-art TiO_2 and ZnO DSCs with Z907 and I_3^-/I^- redox couple. The concept electrode is well suited for DSC since only a small volume fraction is lost to the transparent 3D host material leaving most of the volume for the light harvesting sensitized mesoporous anatase TiO_2 . The straightforward and simple bottom-up fabrication technique produces a highly optically scattering 3D photoanode material that could enhance light harvesting and charge extraction and reduce interfacial recombination to significantly increase the cell photovoltage, photocurrent and the fill factor in various low cost photovoltaic technologies.⁶⁰

In addition, the first high-efficiency ss-DSC built using a 3D fibrous network of anatase nanowires self-assembled from fused single-crystal nanorods was presented. This novel photoanode material is the first to incorporate a high-conductivity network for efficient electron extraction, a high roughness factor for dye loading, and large pores for enhanced light harvesting through light scattering. XRD, HRSEM, and TEM were used to show that the primary protonated titanate nanorods spontaneously orient themselves and self-assemble into secondary nanowires of joined particles with optimized anatase crystallographic orientations. This morphology offers large pores that efficiently scatter light to enhance light harvesting and a high roughness factor of 144 that permits good dye loading. Through a detailed study using electrochemical impedance spectroscopy, it was confirmed that this 3D morphology presents a significantly higher conductivity, shorter transport time, and longer electron lifetime over a wide range of applied potential than comparable nanoparticle-based ss-DSCs which result in improved collection efficiencies. Ultimately, these factors combine to give the highest recorded power conversion efficiency in a nanowire-based solid-state device of 4.9% (AM1.5). This novel 3D network of single-crystalline nanowires presents morphological and electronic characteristics that put it in direct competition with conventional nanoparticle-based ss-DSCs, which are now capable of achieving only slightly higher power conversions of 5% (AM1.5).

Supporting Information Available. Full experimental procedures including H-P-G photoanode fabrication, nanowire synthesis and suspension as well as further titanate nanowire decomposition analysis. This material is available in the appendix D of this thesis.

8.4 References

1. Green, A., Palomares, E., Haque, S., Kroon, J. & Durrant, J. Charge transport versus recombination in dye-sensitized solar cells employing nanocrystalline TiO₂ and SnO₂ films. *J. Phys. Chem. B* 109, 12525–12533 (2005).
2. Martinson, A. B. F. et al. Radial electron collection in dye-sensitized solar cells. *Nano Letters* 8, 2862–2866 (2008).
3. Martinson, A. B. F., Elam, J. W., Hupp, J. T. & Pellin, M. J. ZnO nanotube based dye-sensitized solar cells. *Nano Lett* 7, 2183–2187 (2007).
4. Kay, A. & Graetzel, M. Dye-sensitized core-shell nanocrystals: Improved efficiency of mesoporous tin oxide electrodes coated with a thin layer of an insulating oxide. *Chem Mater* 14, 2930–2935 (2002).
5. Ramasamy, E. & Lee, J. Ordered Mesoporous SnO₂-Based Photoanodes for High-Performance Dye-Sensitized Solar Cells. *J Phys Chem C* 114, 22032–22037 (2010).
6. Yang, W., Wan, F., Chen, S. & Jiang, C. Hydrothermal Growth and Application of ZnO Nanowire Films with ZnO and TiO₂ Buffer Layers in Dye-Sensitized Solar Cells. *Nanoscale Research Letters* 1486–1492 (2009).
7. Prasittichai, C. & Hupp, J. T. Surface Modification of SnO₂ Photoelectrodes in Dye-Sensitized Solar Cells: Significant Improvements in Photovoltage via Al₂O₃ Atomic Layer Deposition. *J Phys Chem Lett* 1, 1611–1615 (2010).
8. Snaith, H. J. & Ducati, C. SnO₂-Based Dye-Sensitized Hybrid Solar Cells Exhibiting Near Unity Absorbed Photon-to-Electron Conversion Efficiency. *Nano Lett* 10, 1259–1265 (2010).
9. Chiba, Y. et al. Dye-sensitized solar cells with conversion efficiency of 11.1%. *Japanese Journal of Applied Physics* 45, 1638–1640 (2006).
10. Snaith, H. J. Estimating the Maximum Attainable Efficiency in Dye-Sensitized Solar Cells. *Adv Funct Mater* 20, 13–19 (2010).
11. Miguez, H., Tétreault, N., Yang, S., Kitaev, V. & Ozin, G. A new synthetic approach to silicon colloidal photonic crystals with a novel topology and an omni-directional photonic bandgap: Micromolding in inverse silica opal (MISO). *Adv Mater* 15, 597–600 (2003).
12. Tétreault, N. et al. New route to three-dimensional photonic bandgap materials: Silicon double inversion of polymer templates. *Adv Mater* 18, 457–+ (2006).
13. Kim, H., Lee, H.-B.-R. & Maeng, W. J. Applications of atomic layer deposition to nanofabrication and emerging nanodevices. *Thin Solid Films* 517, 2563–2580 (2009).
14. Li, T. C. et al. Surface Passivation of Nanoporous TiO₂ via Atomic Layer Deposition of ZrO₂ for Solid-State Dye-Sensitized Solar Cell Applications. *J Phys Chem C* 113,

- 18385–18390 (2009).
15. Le Formal, F. et al. Passivating surface states on water splitting hematite photoanodes with alumina overlayers. *Chem. Sci.* 2, 737–743 (2011).
 16. Miguez, H. et al. Mechanical stability enhancement by pore size and connectivity control in colloidal crystals by layer-by-layer growth of oxide. *Chem. Commun.* 2736–2737 (2002).
 17. Ito, S., Murakami, T., Comte, P., Liska, P. & Graetzel, C. Fabrication of thin film dye sensitized solar cells with solar to electric power conversion efficiency over 10%. *Thin Solid Films* 4613–4619 (2008).
 18. O'Regan, B. C. et al. Influence of the TiCl_4 Treatment on Nanocrystalline TiO_2 Films in Dye-Sensitized Solar Cells. Charge Density, Band Edge Shifts, and Quantification of Recombination Losses at Short Circuit.
 19. Cao, Y. et al. Dye-Sensitized Solar Cells with a High Absorptivity Ruthenium Sensitizer Featuring a 2-(Hexylthio)thiophene Conjugated Bipyridine. *The Journal of Physical Chemistry C* 113, 6290–6297 (2009).
 20. Martinson, A. B. F., McGarrah, J. E., Parpia, M. O. K. & Hupp, J. T. Dynamics of charge transport and recombination in ZnO nanorod array dye-sensitized solar cells. *Phys. Chem. Chem. Phys.* 8, 4655–4659 (2006).
 21. Martinson, A. B. F. et al. Electron Transport in Dye-Sensitized Solar Cells Based on ZnO Nanotubes: Evidence for Highly Efficient Charge Collection and Exceptionally Rapid Dynamics. *J Phys Chem A* 113, 4015–4021 (2009).
 22. Keis, K., Magnusson, E., Lindstrom, H., Lindquist, S. & Hagfeldt, A. A 5% efficient photo electrochemical solar cell based on nanostructured ZnO electrodes. *Sol Energ Mat Sol C* 73, 51–58 (2002).
 23. He, C., Zheng, Z., Tang, H., Zhao, L. & Lu, F. Electrochemical Impedance Spectroscopy Characterization of Electron Transport and Recombination in ZnO Nanorod Dye-Sensitized Solar Cells. *The Journal of Physical Chemistry C* 113, 10322–10325 (2009).
 24. Gao, F. et al. Enhance the Optical Absorptivity of Nanocrystalline TiO_2 Film with High Molar Extinction Coefficient Ruthenium Sensitizers for High Performance Dye-Sensitized Solar Cells. *J Am Chem Soc* 130, 10720–10728 (2008).
 25. Graetzel, M. The advent of mesoscopic injection solar cells. *Prog. Photovolt: Res. Appl.* 14, 429–442 (2006).
 26. Snaith, H. & Schmidt-Mende, L. Advances in liquid-electrolyte and solid-state dye-sensitized solar cells. *Adv. Mater.* 19, 0 (2007).
 27. Yanagida, S., Yu, Y. & Manseki, K. Iodine/Iodide-Free Dye-Sensitized Solar Cells. 42, 0 (2009).
 28. Bach, U. et al. Solid-state dye-sensitized mesoporous TiO_2 solar cells with high photon-to-electron conversion efficiencies. *Nature* 395, 583–585 (1998).
 29. Snaith, H. J. et al. Efficiency Enhancements in Solid-State Hybrid Solar Cells via Reduced Charge Recombination and Increased Light Capture. *Nano Lett* 7, 3372–3376 (2007).
 30. Wang, M. et al. High efficiency solid-state sensitized heterojunction photovoltaic device. *Nano Today* 5, 169–174 (2010).
 31. Schmidt-Mende, L., Zakeeruddin, S. M. & Graetzel, M. Efficiency improvement in

- solid-state-dye-sensitized photovoltaics with an amphiphilic Ruthenium-dye. *Applied Physics Letters* 86, 0 (2005).
32. Fabregat-Santiago, F. et al. Electron Transport and Recombination in Solid-State Dye Solar Cell with Spiro-OMeTAD as Hole Conductor. *J. Am. Chem. Soc.* 131, 5 (2009).
 33. Jennings, J. & Peter, L. M. A reappraisal of the electron diffusion length in solid-state dye-sensitized solar cells. *J. Phys. Chem. Lett.* 111, 0 (2007).
 34. Kruger, J., Plass, R., Graetzel, M., Cameron, P. & Peter, L. M. Charge transport and back reaction in solid-state dye-sensitized solar cells: A study using intensity-modulated photovoltage and photocurrent spectroscopy. *J. Phys. Chem. B* 107, 0 (2003).
 35. Snaith, H. & Graetzel, M. Electron and hole transport through mesoporous TiO₂ infiltrated with spiro-MeOTAD. *Adv. Mater.* 19, 0 (2007).
 36. Ding, I.-K. et al. Pore-Filling of Spiro-OMeTAD in Solid-State Dye Sensitized Solar Cells: Quantification, Mechanism, and Consequences for Device Performance. *Adv Funct Mater* 19, 2431–2436 (2009).
 37. Dloczik, L. et al. Dynamic response of dye-sensitized nanocrystalline solar cells: Characterization by intensity-modulated photocurrent spectroscopy. *J. Phys. Chem. B* 101, 10281–10289 (1997).
 38. Kopidakis, N., Schiff, E., Park, N., van de Lagemaat, J. & Frank, A. Ambipolar diffusion of photocarriers in electrolyte-filled, nanoporous TiO₂. *J Phys Chem B* 104, 3930–3936 (2000).
 39. van de Lagemaat, J., Zhu, K., Benkstein, K. D. & Frank, A. J. Temporal evolution of the electron diffusion coefficient in electrolyte-filled mesoporous nanocrystalline TiO₂ films. *Inorganica Chimica Acta* 361, 620–626 (2008).
 40. Wang, Q. et al. Characteristics of high efficiency dye-sensitized solar cells. *J Phys Chem B* 110, 25210–25221 (2006).
 41. Law, M., Greene, L., Johnson, J., Saykally, R. & Yang, P. Nanowire dye-sensitized solar cells. *Nat Mater* 4, 455–459 (2005).
 42. Mor, G. K., Shankar, K., Paulose, M., Varghese, O. K. & Grimes, C. A. Use of highly-ordered TiO₂ nanotube arrays in dye-sensitized solar cells. *Nano Letters* 6, 215–218 (2006).
 43. Chen, P. et al. Solid-state dye-sensitized solar cells using TiO₂ nanotube arrays on FTO glass. *J Mater Chem* 19, 5325–5328 (2009).
 44. Kay, A. & Graetzel, M. Low cost photovoltaic modules based on dye sensitized nanocrystalline titanium dioxide and carbon powder. *Sol Energ Mat Sol C* 44, 0 (1996).
 45. Chen, D., Huang, F., Cheng, Y.-B. & Caruso, R. A. Mesoporous Anatase TiO₂ Beads with High Surface Areas and Controllable Pore Sizes: A Superior Candidate for High-Performance Dye-Sensitized Solar Cells. *Adv. Mater.* 21, 2206–2210 (2009).
 46. Halaoui, L., Abrams, N. & Mallouk, T. Increasing the conversion efficiency of dye-sensitized TiO₂ photoelectrochemical cells by coupling to photonic crystals. *J. Phys. Chem. B* 109, 9 (2005).
 47. Mihi, A., Calvo, M. E., Anta, J. A. & Miguez, H. Spectral Response of Opal-Based Dye-Sensitized Solar Cells. *J Phys Chem C* 112, 13–17 (2008).
 48. Guldin, S. et al. Dye-Sensitized Solar Cell Based on a Three-Dimensional Photonic

- Crystal. Nano Letters 10, 2303–2309 (2010).
49. Li, R., Liu, J., Cai, N., Zhang, M. & Wang, P. Synchronously Reduced Surface States, Charge Recombination, and Light Absorption Length for High-Performance Organic Dye-Sensitized Solar Cells. *J. Phys. Chem. B* 114, 0 (2010).
 50. Penn, R. & Banfield, J. Morphology development and crystal growth in nanocrystalline aggregates under hydrothermal conditions: Insights from titania. 63, 1549–1557 (1999).
 51. Zhang, Q., Liu, S.-J. & Yu, S.-H. Recent advances in oriented attachment growth and synthesis of functional materials: concept, evidence, mechanism, and future. *J. Mater. Chem.* 19, 191–207 (2009).
 52. Alimohammadi, M. & Fichthorn, K. A. Molecular Dynamics Simulation of the Aggregation of Titanium Dioxide Nanocrystals: Preferential Alignment. *Nano Letters* 9, 4198–4203 (2009).
 53. Wang, P. et al. Enhance the performance of dye-sensitized solar cells by Co-grafting amphiphilic sensitizer and hexadecylmalonic acid on TiO₂ nanocrystals. *J. Phys. Chem. B* 107, 325–333 (2003).
 54. Bisquert, J. Theory of the impedance of electron diffusion and recombination in a thin layer. *J. Phys. Chem. B* 106, 325–333 (2002).
 55. Bisquert, J., Garcia-Belmonte, G., Fabregat-Santiago, F. & Compte, A. Anomalous transport effects in the impedance of porous film electrodes. 1, 429–435 (1999).
 56. Fabregat-Santiago, F., Bisquert, J., Palomares, E., Haque, S. A. & Durrant, J. R. Impedance spectroscopy study of dye-sensitized solar cells with undoped spiro-OMeTAD as hole conductor. 100, 034510 (2006).
 57. Di Valentin, C., Pacchioni, G. & Selloni, A. Reduced and n-Type Doped TiO₂: Nature of Ti³⁺ Species. *J. Phys. Chem. Lett.* 113, 20543–20552 (2009).
 58. Bisquert, J., Garcia-Belmonte, G. & Fabregat-Santiago, F. Modelling the electric potential distribution in the dark in nanoporous semiconductor electrodes. 3, 337–347 (1999).
 59. Nakade, S. et al. Dependence of TiO₂ nanoparticle preparation methods and annealing temperature on the efficiency of dye-sensitized solar cells. *J. Phys. Chem. B* 106, 10004–10010 (2002).
 60. Moser, J., Wolf, M., Lenzmann, F. & Graetzel, M. Photoinduced charge injection from vibronically hot excited molecules of a dye sensitizer into acceptor states of wide-bandgap oxide semiconductors. *Z Phys Chem* 212, 85–92 (1999).

FINAL CONCLUSION

Chapter 9. Final Conclusion, Outlook and Recommendations

The work conducted in this thesis aimed at improving the performances of an oxide-based tandem cell for photoelectrochemical water splitting. In the Part A of this document, we have seen different PEC systems for solar hydrogen generation. In particular, I have demonstrated new tandem architectures using metal-oxide photoanodes and dye-sensitized solar cells. In the Part B, I report on my contribution to the improvement of an easily processable nanostructured hematite photoanode, addressing known limitations such as poor charge conduction and diffusion. In particular, I have shown a method to precisely control the feature size of the morphology independent of the activation temperature. In Part C, organized titania nanostructures are synthesized and applied as a photoanode in the DSC in an attempt to improve charge dynamics.

The conclusions of each section are summarized below.

9.1 Tandem cells for photoelectrochemical water splitting

In this part, the motivations and theoretical framework for the PEC water splitting were examined. The maximum theoretical maximum efficiency of 10 %STH obtainable with a single perfect material in a S2 scheme can be surmounted to up to 20 %STH by using a tandem approach. Several approaches available were reviewed, including photovoltaic / photovoltaic, photovoltaic / photoanode and photoanode / photocathode approaches. Practical device considerations in terms of engineering were also mentioned.

Three different T6 tandem configurations using hematite photoanodes and DSCs with dye tuned to optimize light harvesting have been analyzed in terms of optics and spectral response. A simple optical model was presented to predict the performance of the device, according to which the novel trilevel architecture (hematite / squaraine dye DSC / black dye DSC) was found to produce the highest operating photocurrent density and thus the highest solar to hydrogen conversion efficiency (1.36 %STH).

Subsequently, based in advances in both fields, genuine D4 water splitting devices were demonstrated using tungsten trioxide and hematite electrodes as photoanodes and high voltage cobalt complex electrolyte based DSC as a single electron bias provider. Efficiencies as high as 3.1%STH - a ten-fold improvement over previous demonstrations with this class of device - was demonstrated. By further scrutinizing the photon pathways and exploitation routes in the discrete optical elements of the device, I was able to identify the bottlenecks and limitations of a α - Fe_2O_3 / DSC as well as a WO_3 oxide / DSC tandem cell and further suggest routes for improvement. In addition, the optical model proposed earlier was shown to accurately anticipate the operation conditions of such systems. This work describes a breakthrough in the inexpensive solar-to-chemical conversion using improved photon management in a dual-absorber tandem cell and will undoubtedly constitute a benchmark for solar fuel production by solution processable oxide based devices.

9.2 Solution based colloidal hematite photoanode for water oxidation

Hematite ($\alpha\text{-Fe}_2\text{O}_3$) is a great candidate material for oxygen evolving photocathodes due to its availability, low cost, non-toxicity and appropriate band gap allowing extensive absorption in the visible part of the spectrum. However, it suffers severe drawbacks, among which are poor majority carrier conductivity and a short diffusion length of minority charge carrier with regard to photon penetration depth. This circumstance causes most photogenerated charges to have a low probability of reaching the semi-conductor / liquid junction and thus to participate in the water oxidation reaction. This feature requires the use of hematite morphologies having feature size in the range of 10-20 nm.

A solution-based colloidal approach offers a simple and easily scalable method to obtain nanostructured hematite. However, this type of nanostructure needs to be exposed to an annealing step at 800 °C to become photoactive. This has been attributed to the diffusion of dopants from the substrate. In addition, this annealing step sinters the 10 nm particles colloid into a feature size approaching 100 nm.

Here, I first show the effect of intentionally doping this material on the sintering and photoactivity. I then demonstrate a new method to decouple the morphological and functional effects of annealing by encapsulating the nanostructure in a rigid scaffold. It consists in depositing a conformal silica layer by solution based means between the morphological annealing step - where the feature size of the nanostructure can be controlled - and the functional annealing step that triggers photoactivity in the material. This strategy allowed applying high temperature annealing steps while controlling the feature size of the nanoparticles. This latter strategy coupled to further passivation of surface states allowed an improvement of the net photoactivity of this type of photoanode by a factor of two. A reproducible net photocurrent exceeding 4 mA.cm⁻² was obtained. This result represents the highest performance reported for hematite under one sun illumination.

9.3 Nanostructures for the dye sensitized solar cell

Unidimensional titania nanotubes arrays have been of great interest in the past few years due to the potential faster electron pathway to the electrode it could offer. Here, I have demonstrated the possibility of using this type of nanostructure made on a low cost metallic titanium opaque foil by potentiostatic anodization in flexible DSCs using ITO-PEN as a counter electrode and ionic liquid as a redox mediator. The efficiency of 3.6 % was obtained under AM 1.5 simulated solar illumination. The main limiting factor for this type of device was found to be the charge transfer resistance at the counter electrode, which had a detrimental effect on the fill factor.

Alternatively, I demonstrated a method to grow TNT arrays on transparent substrate from sputtered Ti/TiO₂ double layer on FTO-glass. A flat overlayer resulting from incomplete anodization process was kept on top of the structure. This overlayer prevented protrusion to create a shunt path between the anode and the gold counterelectrode and allowed the use of this nanostructure in solid-state devices for the first time to obtain an efficiency of 1.67 %.

I then showed a novel bottom-up 3D host-passivation-guest photoanode for the DSC made of a high electron mobility host, a passivating conformal blocking layer and a high surface area guest to improve short circuit current density, fill factor, and photovoltage. I used Al/ZnO, SnO₂ and TiO₂ (control) as host materials, TiO₂ as passivating material and anatase nanoparticles as guest material. The tridimensionality of the structure was obtained by the use of a self-assembled disordered opal template simply casted on the conductive substrate. An increase in photovoltage of up to 110 mV over the state of the art TiO₂ and ZnO DSCs with Z907 dye and I₃⁻ / I⁻ redox couple was obtained.

Finally, I presented the first high efficiency ss-DSC built using a 3D fibrous network of anatase nanowires self assembled from fused single crystal-nanorods. This nanostructure was found by impedance spectroscopy to exhibit higher electron conductivity, shorter transport time and longer electron lifetime over a wide range of applied bias. This material gave a 4.9 % efficient solid state device.

9.4 Outlook and recommendations

9.4.1 Bringing the Tandem PEC to the market place

The PEC tandem cell based on one photoanode and one single DSC is a device that could potentially be exploited at a commercial level. It is difficult to assess exactly the price that could be obtained for a kilogram of hydrogen with this system. But provided that such a system can be produced at a price of 150 \$.m⁻² and can deliver a photocurrent of 5 mA.cm⁻², the capital cost of hydrogen would be as low as 4 \$.kg⁻¹ a performance competing with those of PV-electrolyzer systems.¹ This figure is equivalent to obtaining the energy contained in one liter of refined unleaded 95 for as low as 0.89 \$, less than half of the retail price of gasoline in most European countries.²

To reach this goal, engineering efforts have to be deployed to reduce system price and address optical losses by the design a monolithic device. We have seen in chapter 6 that a photocurrent of over 4 mA.cm⁻² can be obtained from a simple solution based hematite photoanode. Considering the theoretical maximum photocurrent of about 13 mA.cm⁻² obtainable with hematite a target of 5 mA.cm⁻² for the full system seems realistic.

9.4.2 The ideal hematite photoanode

In this thesis, I have mentioned strategies to nanostructure hematite, incorporate dopant, passivate the semiconductor / liquid junction and improve the oxygen evolution reaction kinetics by means of catalysis. More challenges have attracted my eye in the course of the PhD, including the recombination and difficult charge transfer at the semiconductor / substrate interface on one hand and the design of clever hybrid nanostructures on the other hand.

The first has animated the community in the past few years and several materials have been shown successful into acting as buffer-layers, such as SiO_x,³ Ga₂O₃,⁴ TiO₂ and Nb₂O₅,⁵ helping relaxing crystal lattice stresses between the transparent conductive oxide and the photoactive material. The champion material, niobium oxide, usually allows an increase in the photocurrent of about 0.6 mA.cm⁻² whereas gallium oxide shifts the onset potential of the photocurrent about 100 mV

cathodically.

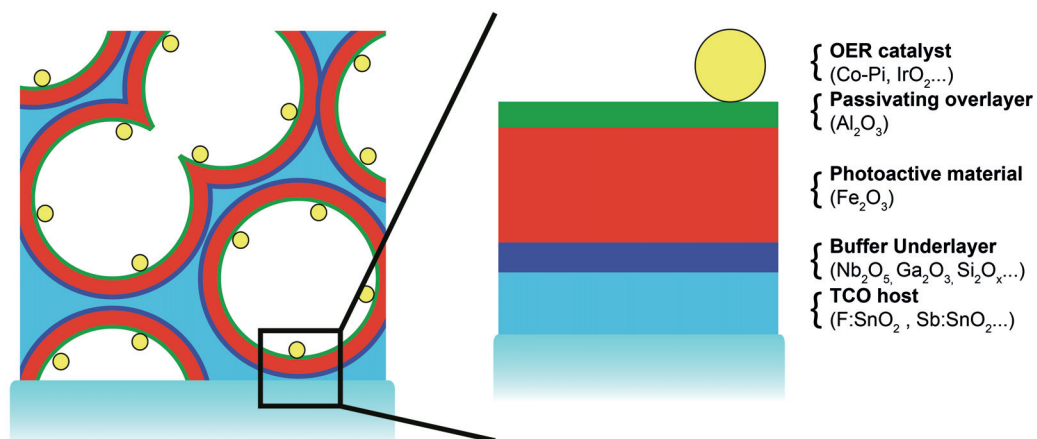


Figure 9.1: Scheme of the ideal photoanode.

Clever hybrid nanostructures similar to the one presented in the first section of chapter 8 where the absorption and the charge conduction functions of the materials are decoupled represent arguably the easiest approach for obtaining the ideal photoanode morphology. The self-assembled organic template offers excellent control over the pore size and connectivity. The aspect ratio can be easily tuned by simply selecting polystyrene spheres of different sizes and use colloidal solutions of different concentration. Finally the deposition method of the template is trivial. Such a template can be conformally coated with transparent conductive oxide (TCO) material. After removal of the organic template, the revealed conductive host can then be coated in one single step with a buffer-layer, followed by the optimal thickness of doped photoactive material and a passivating overlayer. Atomic layer deposition is the ideal technique as it allows conformal deposition with precise control over the thickness of the material deposited. Finally the photoanode can be finalized with the deposition of a water oxidation catalyst on the exposed surface. Figure 9.1 depicts the ideal photoanode described above. This electrode is currently under investigation.

9.5 Last word...

Economical solar hydrogen production is at a stone's throw away. The finding and innovations presented in this thesis and the recent advances of the scientific community also find application in other solar fuel production approaches, by means of CO₂ reduction in particular. Ammonia and formic acid are examples of energy vectors competing with hydrogen.

I am convinced the international community will keep on investing money and efforts into finding efficient alternative for energy production, distribution and use. I am curious to see what the future will bring, what the next generation habits will be, how we will finally make full use of the most valuable resource we have on the planet: the Sun.

1. Figures provided by Julian Keable and Brian Holcroft, Stored Solar.
2. GIZ 2011, Worldwide Retail Prices of Gasoline (US cents per liter), International Fuel Prices 2010/2011, German International Cooperation, Eschborn, viewed 4th March, 2011.
3. Le Formal, F., Graetzel, M. & Sivula, K. Controlling Photoactivity in Ultrathin Hematite Films for Solar Water-Splitting. *Adv Funct Mater* 20, 1099–1107 (2010).
4. Hisatomi, T. et al. A Ga₂O₃ underlayer as an isomorphic template for ultrathin hematite films toward efficient photoelectrochemical water splitting. *Faraday Discuss.* 155, 223 (2012).
5. Hisatomi, T. et al. Enhancement in the Performance of Ultrathin Hematite Photoanode for Water Splitting by an Oxide Underlayer. *Adv Mater* 24, 2699–2702 (2012).

Appendix

Appendix A

Equipment and Characterization

Characterization of the DSC:

Current-Voltage curves

A 450 W xenon light source (Oriel, USA) was used to characterize the solar cells. The spectral output of the lamp was matched in the region of 350–750 nm with the aid of a Schott K113 Tempax sunlight filter (Präzisions Glas & Optik GmbH, Germany) so as to reduce the mismatch between the simulated and true solar spectra to less than 4 %. Various incident light intensities were regulated with neutral wire mesh attenuators. The current–voltage characteristics of the cell under these conditions were obtained by applying external potential bias to the cell and measuring the generated photocurrent with a Keithley model 2400 digital source meter (Keithley, USA).

IPCE measurement

A modulated light intensity data acquisition system was used to control the Incident Photon-to-Current conversion Efficiency (*IPCE*) measurement. The modulation frequency was about 1 Hz. Light from a 300 W Xenon lamp (ILC Technology, USA) was focused through a computer controlled Gemini-180 double monochromator (Jobin Yvon Ltd., UK) onto the photovoltaic cell under test. A white light bias was used to bring the total light intensity on the device under test closer to operating conditions. The devices were masked to attain an illuminated active area of 0.2 cm². The monochromator was incremented through the visible spectrum to

generate the $IPCE(\lambda)$ as defined below.

$$IPCE(\lambda) = 1240(J_{SC}/\lambda)$$

where λ is the wavelength, J_{SC} is short-circuit current photocurrent (mA cm^{-2}), and Φ is the incident radiative flux (W.m^{-2}). This curve can be derived from the measured absorption spectrum of the adsorbed photosensitizer for comparison.

Electrochemical Impedance Spectroscopy Measurements

The electrochemical impedance spectroscopy (EIS) measurements of the samples were performed at 20 °C using a sinusoidal potential perturbation of 10 mV, which was applied over a frequency range from 1 MHz down to 0.1 Hz (Autolab PG30). Measurements were analyzed using the transmission line model from Bisquert et al.

Photoanodes Characterization:

Photoelectrochemical characterization:

Photocurrent measurements were performed to estimate the solar photocurrent of the photo-anodes in a three-electrode configuration with 1 M NaOH (pH 13.6) as electrolyte for Fe_2O_3 and 1 M HClO_4 (Fluka, ACS reagent puriss in Milli-Q water, 25°C, pH = 0) for the WO_3 , using Ag/AgCl in saturated KCl as a reference electrode. The hematite electrodes were scanned at 50 mV.s^{-1} between -300 mV vs. Ag/AgCl and the onset of the dark current (800 mV and 900 mV vs. Ag/AgCl, respectively for the control and encapsulated electrodes). The potential is reported relative to the reversible hydrogen electrode potential (RHE). The samples were illuminated (area = 0.5 cm^2) with simulated sunlight from a 450 W xenon lamp (Osram, ozone free) using a KG3 filter (3 mm, Schott) with a measured intensity of 1 sun (100 mW.cm^{-2} , spectrally corrected) at the sample face. Photocurrent action spectra were obtained under light from a 300 W Xe lamp with an integrated parabolic reflector (Cermex PE 300 BUUV) passing through a monochromator (Bausch & Lomb, bandwidth 10 nm fwhm). The wavelength was scanned at 1 nm/s , and the monochromatic photocurrent of the Fe_2O_3 electrode compared with that of a UV enhanced Si-photodiode (Oriel 71883) of known $IPCE$ spectrum. In order to be consistent with previous work, the photo-anode action spectra were measured at the

potential corresponding to the plateau current defined at the minimum of the first derivative of the photocurrent.

IPCE measurement

The photoanodes photocurrent action spectra were obtained under light from a 300 W Xe-lamp with integrated parabolic reflector (Cermax PE 300 BUUV) passing through a monochromator (Bausch & Lomb, bandwidth 10 nm fwhm). The sample was biased to 1.03 V vs RHE in order to approach the device operating conditions.

Common characterization

UV-vis spectra: Total transmittance spectra were measured with a Varian Cary 5 spectrophotometer equipped with an 11 cm diameter integrating sphere coated with polytetrafluoroethylene (PTFE). The photoanodes were wetted with water and covered with a microscopy cover glass in order to reduce light reflections at the Fe₂O₃ or WO₃ surface, and to approach the conditions in the photoelectrochemical cell. The absence of sample was used as a blank in order to take into account light absorption from each material of the devices and every reflection at the interfaces. The absorptivity, A , was calculated from these measurements with the formula $A = 1 - T - R$, with T the total transmittance and R the total reflectance.

Scanning Electron Microscopy (SEM):

The morphology of the mesoporous hematite thin films were characterized using a high-resolution scanning electron microscope (FEI XL30 SFEG). The acceleration voltage was 5 keV while an in-lens detector was employed with a working distance of 5 mm. The samples were investigated after the photoelectrochemical measurements and sample positions coincided with the illuminated area.

Mobility Measurement on Al/ZnO and SnO₂

Electron mobility in Al/ZnO and SnO₂ was obtained using Hall Effect measurement (Microworld HMS-3000) on a 90 nm thick film on glass substrate at

room temperature in the dark.

Appendix B

Supporting information to Chap.4

Materials and Methods

Hematite photoanode fabrication

Silicon-doped hematite photoanodes were made by atmospheric pressure chemical vapor deposition (APCVD) from $\text{Fe}(\text{CO})_5$ (Aldrich 99.999%) and tetraethoxylane (TEOS; Aldrich 99.999%) on F:SnO₂-coated glass (TEC15, Hartford Glass) as previously reported in the literature. Precautions were made to select deposition parameters offering an optimal transparency and light scattering as well as the lowest onset potential of the photocurrent. Six cycles of ALD of Al₂O₃ and a cobalt catalyst were deposited on the surface of the cauliflower nanostructure in order to further improve the onset potential of the photocurrent.

Tungsten trioxide photoanode fabrication

Mesoporous WO₃ photoanodes were synthesized using an earlier reported aqueous sol-gel method. The precursor consisted of (poly)tungstic acid, freshly prepared by elution of a solution of Na₂WO₄ through the cation exchange column, and of an organic additive acting as porogen, low molecular weight polyethylene glycol (PEG) 300. To insure high porosity of the final films the precursor contained an excess of PEG, corresponding to the WO₃/PEG ratio of 0.6 w/w. The colloidal precursor was deposited onto conductive F:SnO₂-coated glass plates (Pilkington Glass,

resistance 8-10 Ω /square) using doctor-blade technique, dried in air at 100°C and, subsequently, the sample was annealed in flowing oxygen at 550°C for 30 min. The final *ca.* 2.5 μm thick film was formed by six consecutive deposition/annealing cycles.

DSC Materials synthesis

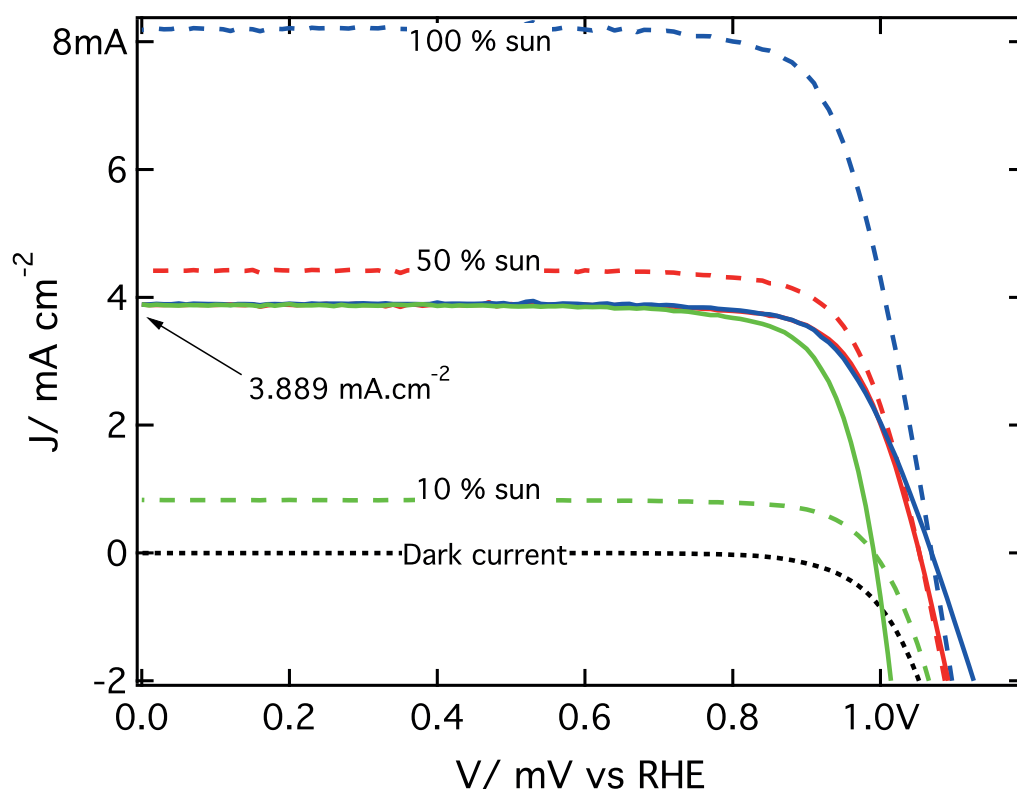
The synthetic details of 3-{6-{4-[bis(2',4'-dihexyloxybiphenyl-4-yl)amino-]phenyl}-4,4-dihexyl-cyclopenta-[2,1-b:3,4-b']dithiophene-2-yl}-2-cyanoacrylic acid (coded Y123) have been described in a previous study. The synthetic details of $[\text{Co}(\text{bpy-pz})_2]^{3+/2+}$ [bpy-pz = 6-(1*H*-pyrazol-1-yl)-2,2'-bipyridine]) have also been described in our previous study. The preparation details of nanoporous poly(3,4-ethylenedioxythiophene) (PEDOT) coated FTO as counter electrode are given elsewhere. In this study, the films were deposited at a DC potential of +1.4 V *vs.* Ag/AgCl for 30 s at room temperature.

DSC Fabrication

The nanocrystalline TiO_2 pastes were prepared using a previously reported procedure. The TiO_2 transparent electrodes composed of ~ 20 nm anatase resulting in ~ 32 nm pore on fluorine doped thin oxide (FTO, 4 mm thickness, 10 ohms/sq, Nippon Sheet Glass, Japan) conducting glass were controlled from 2.5 to 3 μm by the number of screen printing passes. The TiO_2 electrodes were immersed into a 0.1 mM solution of Y123 with 5 mM 3 α ,7 α -dihydroxy-5 β -cholic acid (chenodeoxycholic acid) in 4-*tert*-butanol/acetonitrile mixture (1:1 v/v) and kept for 15 h at room temperature. The applied electrolyte consists of 0.22 M $\text{Co}(\text{L})_n^{2+}$, 0.05 M $\text{Co}(\text{L})_n^{3+}$, 0.01 M LiClO_4 , and 0.3~0.4 M 4-*tert*-butylpyridine in acetonitrile. The dye-adsorbed TiO_2 electrode and PEDOT counter electrode on FTO (TEC 15 ohms/sq, Pilkington) were assembled into a sealed sandwich type cell with a gap of a hot-melt ionomer film, Surlyn (25 μm , Du-Pont). In order to increase light path length, a white paint with tippex was deposited on glass side of counter electrode.

Normalization of *J-V* curves. The DSC was measured under full sun as well as 50 % and 10 % solar illumination. The curve reflecting the best the actual photon flux on the device under illumination through the photoanode was selected in order to approach as close as possible to the full device operation conditions. Photoconductivity, photoresistivity and other mechanism resulting from a variation of

the light intensity and their effects on the shape of the $J-V$ curve were therefore taken into account. The selected $J-V$ curve was then scaled to match its short circuit current to the one obtained by integrating the calculated electron flux in the device as shown in Appendix B.1.



Appendix B.1 : Normalization of the $J-V$ curve of the DSC, case of the WO_3 / DSC tandem device. Dashed lines represent the photocurrent-voltage response of the DSC under 100 % sun (blue), 50 % sun (red) and 10 % sun (green). The dark current is represented with the black dotted line. Plain lines represent the previous curves of which the short circuit current has been normalized to match the J_{sc} calculated from the electro-optical study (cf Figure 4.2). In this case, the curve obtained from the 50 % sun illumination was selected.

Mismatch between in-situ measurements and calculated $J-V$ curves. The small discrepancy observed between the $J-V$ curves obtained from the electro optical study and the in situ measurement can be attributed to the optical losses in the measurement chamber and a mismatch between the light source and the standard solar spectrum. In addition, the in situ measurement of the photoanodes current-voltage curve is done in a two electrodes fashion while the curves obtained from calculation result from three electrodes measurement. The resistance of the electrolyte is therefore visible on the $J-V$ curves of the photoanodes measured in situ

as well as the resistance and overpotential at the counter electrode, in spite of the strict precautions taken in using a large area platinum bundle during two electrodes measurements and for the full device under operation in order to avoid electron flux capping due to surface limited effects. The platinum bundle formed by wrapping up a platinum gauze (woven from 52 wires, 0.1mm diameter) was placed as close as possible to the active area of the photoanode (about three millimeters) in such a way to not interact with the light. Full devices were made by assembling a DSC together with a photoanode spaced by a drop of refractive index matching oil (Immersion Oil 518 F, Zeiss) to avoid extra reflections at the air-glass interfaces. The ensemble was fixed together using epoxy resin in order to plunge the resulting tandem device entirely in the electrolyte. A circular black tape mask presenting an area of 0.196 cm² was applied directly onto the photoanode, and defined the active area of the device.

Appendix C

Supporting information to Chap.6

Materials and Methods.

Preparation of mesoporous thin films:

About 400 mg of dry Fe_2O_3 nanopowder prepared by the thermal decomposition of $\text{Fe}(\text{CO})_5$ (ca. 10 nm dia., provided generously by BASF) was combined using a mortar and pestle with 40 μl of a 10 % solution of acetylacetonone (Acac) in 1-hexanol until all of the powder was incorporated into a paste. Here the hexanol was used to slow solvent evaporation and the Acac was used as a nanoparticle capping surfactant. The nanoparticle paste was then diluted with 1% Acac in 2-propanol by adding 100 μl fractions until 5 ml. This dispersion was sonicated by an ultrasonic tip sonicator (Branson Sonifier 250) in a temperature controlled water-bath (10 °C) at a 20 % duty cycle for 5 min. The solution was allowed to settle and only the supernatant solution containing the colloidal nanoparticles was decanted from the undispersed aggregates. This solution was concentrated by evaporation to 26.4 mg/ml measured by evaporating a known volume of solution and weighing the solids. The nanoparticle solution was combined with a 4.1 wt.% solution of hydroxypropyl cellulose (HPC) in 2-propanol in order to have a 30 wt.% HPC based on solid content and further diluted with 2-propanol (to a final concentration of 9.4 mg/ml based on total solids) to prevent the gelling of the colloid. Titanium isopropoxide was added to the solution four hours prior to the film deposition as a doping source at a concentration of 5 at% with respect to the iron atom content. The final colloid solution containing the porogen and dopant was then coated onto the substrate (F:SnO₂ on aluminoborosilicate, Solaronix) *via* doctor-blading with a 40 μm invisible tape (3M) as a spacer. These films were air-dried for 30 min before the initial heating to remove the organics (2 °C.min⁻¹ to 350 °C, 450 °C and 500 °C, 10 h) and the samples were cooled before encapsulation. The encapsulation was performed after

Ogawa et al. by dipping the substrates in a methanol solution kept at 0 °C and containing water (10.3 M), hexadecyltrimethylammonium chloride (C16TAC, 29 mM) as a structure directing agent, and aqueous ammonia (6.2 M) for hydrolysis. TEOS was added (77 mM) as a Si source and the solution was shook for 1 min before re-immersing in an ice bath until the solution became turbid, indication of the formation of light scattering silica spheres in solution. The samples were then rinsed abundantly with DI water and dried in air. The second heat treatment was done in air in a tube furnace (2 in dia.) at a set point of 800 °C. A thermocouple placed in the tube at the same position of the samples verified the set point temperature within 5 °C. The electrodes were inserted into the preheated furnace in alumina boats and removed after the annealing time (10 min) and allowed to cool on the bench-top. The silica layer was removed with stirring sodium hydroxide, 5M in water at room temperature. The amount of etching time was optimized and was found to depend on the morphological annealing temperature and therefore porosity of the film. The optimized time for the etching of the 350 °C, 450 °C and 500 °C was 3 min, 4 min 30 s and 7 min respectively.

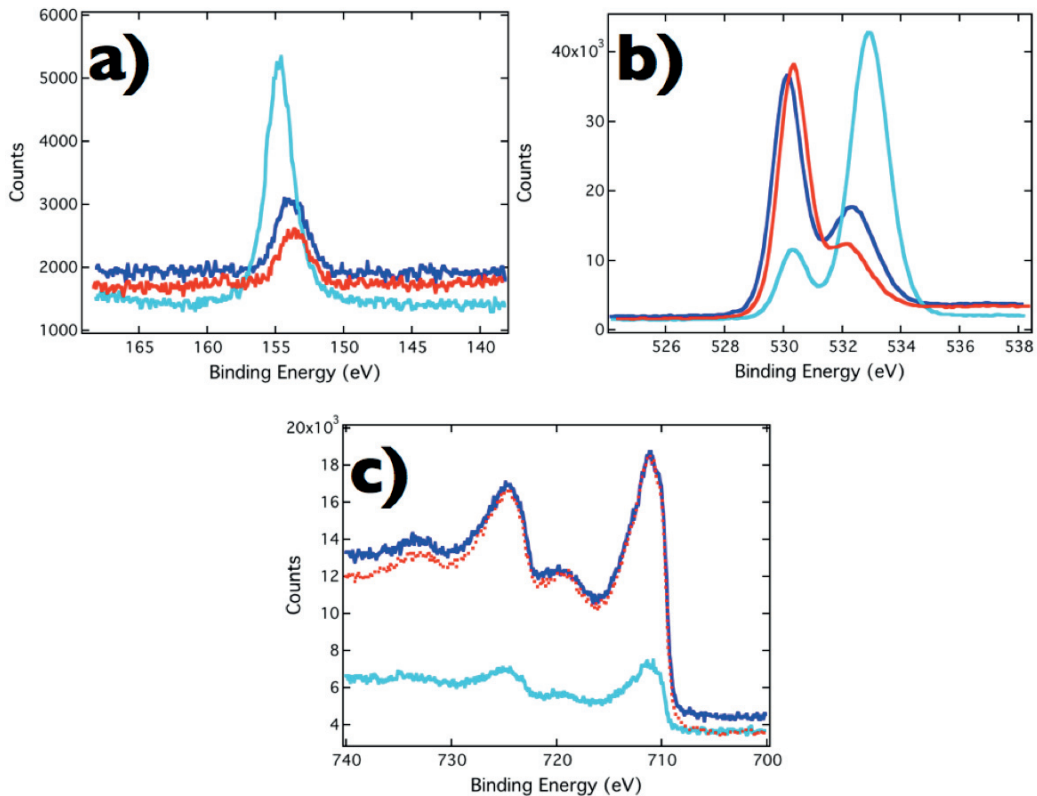
Surface characterization:

X-ray photoelectron spectroscopy was performed on porous hematite films in order to quantitatively measure the elemental composition of the surface. Data were collected by Axis Ultra (Kratos Analytical, Manchester, U.K.) under ultrahigh vacuum condition ($<10^{-8}$ Torr), using a monochromatic Al KR X-ray source (1486.6 eV), in the Surface Analysis Laboratory of CIME at EPFL. The source power was maintained at 150 W (10 mA, 15 kV). The emitted photoelectrons were sampled from a rectangular area of $750 \mu\text{m} \times 350 \mu\text{m}$. Gold (Au 4f_{7/2}) and copper (Cu 2p_{3/2}) lines at 84.0 and 932.6 eV, respectively, were used for calibration. The adventitious carbon 1s peak at 285 eV was used as an internal standard to compensate for any charging effects. Figure S1a shows the silicon atom content on the surface of different samples and exhibits clearly a strong Si 2s peak for the sample infiltrated with confinement scaffold. After scaffold removal, the peak is attenuated to the same level as before silica infiltration. This observation is in good agreement with the results presented in figure S1c displaying the iron atoms content in the same samples. When the confinement scaffold is infiltrated, the Fe 2p peak is attenuated, indicating an ample coverage of

the hematite surface by the silica layer. This is confirmed by the O 1s peak shift from 532.7 eV (attributable to silica) with the presence of the confining scaffold to 530 eV (attributable to hematite) before infiltration and after scaffold removal (Appendix C.2b). Appendix C.1 summarizes the atomic content at the surface of the different samples.

Table C.1 : Surface atomic content (at %) of iron, oxygen, silicon and titanium atoms in control sample, sample infiltrated with confinement scaffold and after confinement scaffold removal.

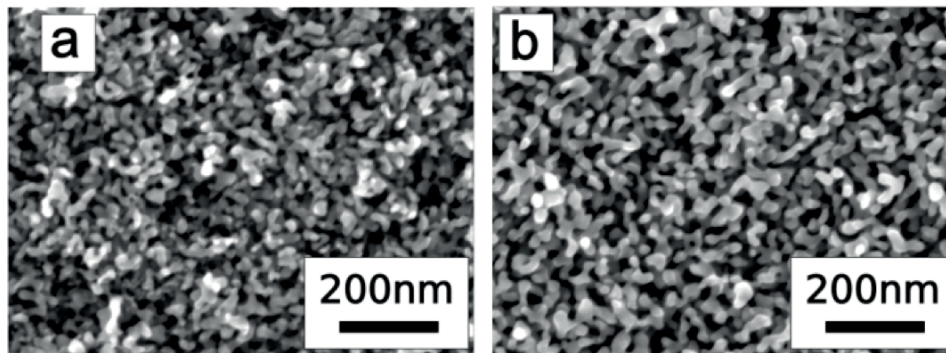
	Surface atomic content (at %)		
	Control sample	After encapsulation	After removal
Fe 2p	25.19	3.78	20.2
O 1s	66.13	71.24	69.9
Si 2s	6.2	24.47	8.05
Ti 2p	2.47	0.5	1.85



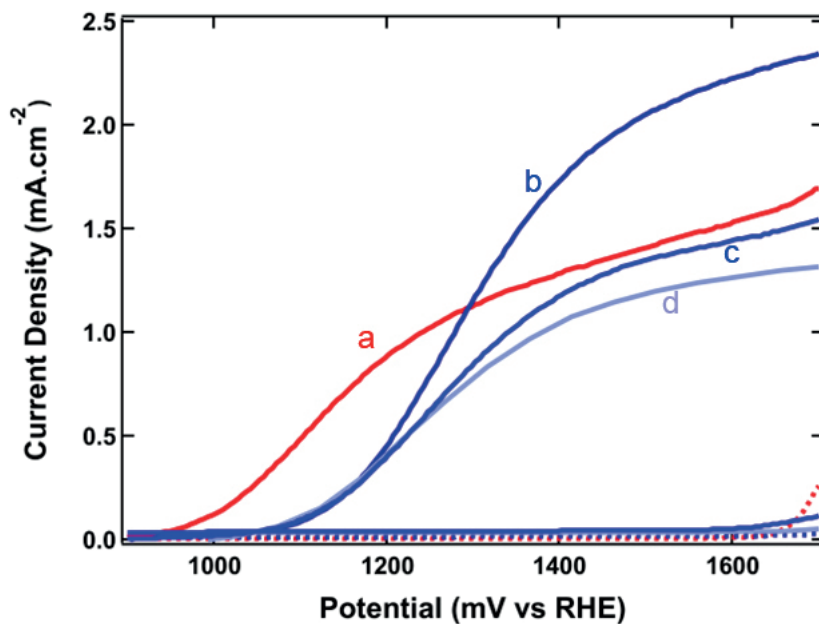
Appendix C.1: XPS plots. a) corresponds to the Si 2s peak. Red curve shows control sample (peak centered at 153.3 eV), light blue shows sample infiltrated with confinement scaffold (peak centered at 154.4 eV) and dark blue shows the same sample after scaffold removal (peak centered at 154.2 eV). b) corresponds to the O 1s peak. Red curve shows control sample (peak centered at 530 eV), light blue shows sample infiltrated with confinement scaffold (peak centered at 532.7 eV) and dark blue shows the same sample after scaffold removal (peak centered at 530 eV). c) corresponds to the Fe 2p peak. Red curve shows control sample (peak centered at 710.6 eV), light blue shows sample infiltrated with confinement scaffold (peak centered at 710.6 eV) and dark blue shows the same sample after scaffold removal (peak centered at 710.7 eV).

Effect of the morphological annealing:

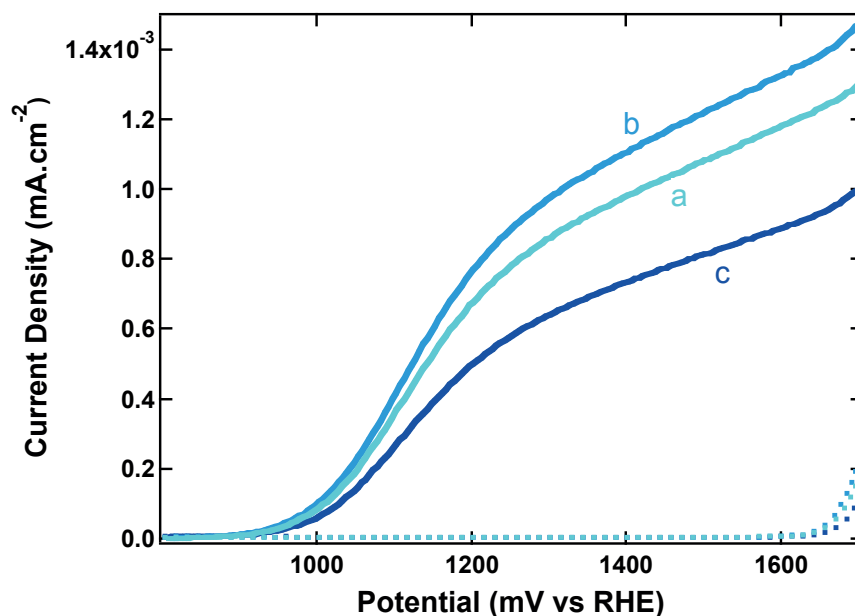
Several different morphological annealing temperatures were tested, with identical infiltration and functional annealing conditions and optimized scaffold removal step. Scanning electron micrographs of the final morphology show a steady increase of the feature size with increasing morphological annealing temperature. Samples treated at 350 °C, 450 °C and 500 °C had a particle size of about 20 nm, 30 nm and 40 nm respectively while control sample – non encapsulated, treated at 800 °C – had a particle size of about 80 – 120 nm. Even though the obtained nanostructure's average particle size was found to be smaller with lower morphological temperature as expected (Figure C2), the over-all photo-activity of these films was not always improved as compared to the control sample (Figure C3). Only the film treated at 500°C showed better plateau photocurrent. The other infiltrated samples exhibited a smaller plateau photocurrent. This result suggests a competition between particle size and electron transport.



App. C2: Scanning electron micrograph of encapsulated electrodes (after the functional annealing and the removal of the SiO₂ scaffold) with morphological annealing performed at 350 °C (a) and 450 °C (b).



App. C3: Electrochemical water oxidation photocurrent (solid lines) and dark current (dotted lines) vs. voltage curves of control (a) and infiltrated (b-d) photo-anodes with different morphological annealing temperatures, 350 °C (d), 450 °C (c) and 500 °C (b), under simulated solar light (AM 1.5G 100 mW.cm⁻², spectrally corrected).



App. C4: Electrochemical water oxidation photocurrent (solid lines) and dark current (dotted lines) vs. voltage curves of uninfiltated samples of different colloid concentration and thus different thickness, under simulated solar light (AM 1.5G 100 mW.cm⁻², spectrally corrected). (a) thinnest film (control solution), (b) medium thickness film (control solution + 50 vol.% isopropanol), (c) thickest film (control solution + 75 vol.% isopropanol)

Appendix D

Supporting information to Chap.8

Three-Dimensional Host–Passivation–Guest Photoanode

Fabrication

A 22 vol % dispersion of 2.2 μm polystyrene microspheres in isopropanol is doctor bladed on a TEC15 FTO-covered glass substrate to reveal a large-area highly light scattering disordered template. It is then heated and infiltrated with 90 nm of Al/ZnO (1:9), SnO₂, or TiO₂ in a highly conformal fashion by atomic layer deposition (ALD) pulses of trimethylaluminum, diethylzinc and water (Al(Me)₃, Zn(Et)₂|H₂O, 114 °C, 1:9), tetrakis(dimethylamino)tin and ozone (Sn(NMe₂)₄|O₃, 200 °C) and tetrakis(dimethylamino)titanium and water (Ti(NMe₂)₄|H₂O, 200 °C) using nitrogen as a carrier gas (Cambridge Nanotech Savannah S100). The infiltrated opal's top surface oxide is removed by RIE (6 min, 1800W, C₄F₈, Ar carrier gas, AMS200) performed before removing the polymer template by annealing (360 °C, 15 min.) The TCO backbone is then conformally coated with 25 nm of dense TiO₂ by ALD in order to reduce interfacial recombination between electrons in the highly conducting TCO backbone and the I₃⁻ oxidized electrolyte (Figure 8.1c). The 3D H-P-G structures were filled with a 17 nm anatase nanoparticle paste through four sequential doctor blading separated by 10 min heating at 120 °C to ensure solvent evaporation and densification of the conformal paste thin film. The electrode is then calcined to burn off the organic materials found in the paste (500 °C, 60 min, 2 °C/min ramp). In order to improve the anatase nanoparticle connectivity and increase the photocurrent, the TiO₂ and SnO₂ H-P-G photoanodes were immersed into a 40 mM aqueous TiCl₄ solution at 70 °C for 30 min and washed with water and ethanol.

3D H-P-G based Dye-Sensitized Solar Cell Fabrication

The 3D host–passivation–guest photoanodes are sintered for 30 min at 500 °C

before dipping in a 0.3 mM Z907 solution (90 vol% 1:1 acetonitrile/tert-butanol, 10 vol% DMF) for 10 min. Following the immersion procedure, the dye-sensitized electrodes are rinsed with acetonitrile and dried in air. The photoanodes are then assembled using a thermally platinized FTO counter electrode (fabricated by spreading out a drop of 5 mM H₂PtCl₆ isopropanol solution on the FTO before treating it at 420 °C for 15 min) using a 25 µm thick hot melt ring (Surlyn, DuPont) and sealed by heating. The cell internal space was filled with a volatile I₃⁻/I⁻ electrolyte (1.0 M DMII, 0.03 M I₂, 0.5 M TBP, 0.05 M LiI, 0.1 M GuNCS), in a 85:15 acetonitrile/valeronitrile mixture through a predrilled hole using a vacuum pump.

Nanowire Synthesis

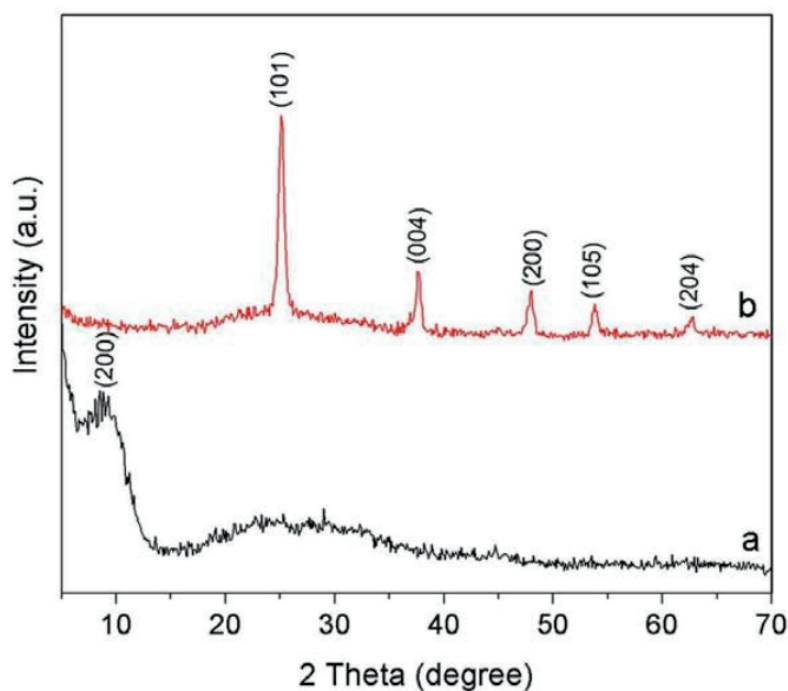
In a typical synthesis, 3.7 g of titanium(IV) oxide nanopowder (99.7% anatase, Aldrich) is mixed with 35 mL of 10 M NaOH (97% Aldrich) solution. The mixture is then transferred into a Teflon-lined stainless steel autoclave (Parr Instrument Company) and heated at 130 °C for 36 h. After this treatment, the autoclave is left to cool to room temperature at a rate of 1 °C min⁻¹. The supernatant is gently decanted from the cake-like half-product that is formed at the bottom of the Teflon linear. Then, 35 mL of 15 M KOH (Fluka) solution is immediately added and the temperature is increased gradually (3 °C min⁻¹) to 200 °C for 24 h. The system is cooled to 150 °C at a rate of 1 °C min⁻¹ and subsequently kept at 150 °C for 12 h. The autoclave is then quenched to room temperature. The white product is then collected, filtered, and washed several times with deionized water and neutralized with the appropriate amount of 0.1 M HCl solution (Merck). It is then washed with hot (80 °C) deionized water in order to remove remaining traces of NaCl and KCl. The white powder is finally dried at 100 °C for 6 h in air. The obtained product is gently ground evacuated at 250 °C for 4 h in vacuum to complete the drying.

Nanowire Suspension

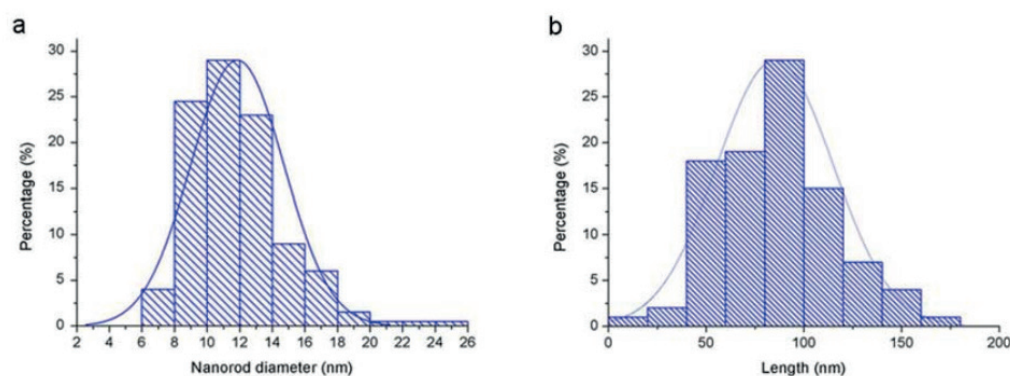
Nanowire powder (2.4 g) is dispersed in 100 mL of 2-propanol (>99.8% Merck), and the mixture is homogenized with an ultrasonic tip (Bandelin Sonopuls, Microtip MS73) 10% amplitude for 30 min.

Titanate Nanowire Decomposition

Once deposited on the FTO glass substrates by doctor blading, the samples are heat treated at 600 °C in air for 2 h. Titanate nanowires crystallize into anatase structure as confirmed by the X-ray diffractograms presented in Appendix D1. The nanowires can be described as a chain-like assembly of TiO₂ nanorods with morphological characteristics presented in Appendix D2.



Appendix D.1 : X-ray diffraction pattern obtained from. a, doctor bladed film composed of titanate nanowires before the calcination. b, interconnected anatase nanorods network after the calcination process. No second phase is detected.



Appendix D.2 : Diameter and length distribution of nanorod building units measured by analyzing a large number of TEM images. Average nanorods diameter and average nanorod length was calculated to be 11.9 nm (st. deviation 2.8 nm) and 85 nm (st. deviation: 32 nm) respectively.

Nanowire based Solid-State Dye-Sensitized Solar Cell Fabrication

Complete DSC devices were prepared using 2.5 μm doctor bladed thin films on FTO glass (TEK15, 15 Ω/\square) covered with a 100 nm compact layer of TiO_2 deposited by spray pyrolysis to avoid recombination losses with the hole transport material. After calcination in air at 600 $^\circ\text{C}$ for 2 h, interconnectivity within the 3D network of nanowires was improved by treating the photoanodes in aqueous acidic TiCl_4 (40 mM, 70 $^\circ\text{C}$, 30 min) or atomic layer deposition (ALD) of titanium tetraisopropoxide (<1 nm, 200 $^\circ\text{C}$). The photoanodes are then dipped overnight in a 1×10^{-4} M acetonitrile solution of C218 high extinction coefficient organic dye. The thin film is then infiltrated with a solution of spiro-MeOTAD hole transport material (Merck GmbH, 180 mg/mL), tert-butyl pyridine (1:26 mL mg $^{-1}$ tbp/spiro-MeOTAD), lithium bis(trifluoromethylsulfonyl)imide salt (Li-TFSI, 170 mg mL $^{-1}$ acetonitrile solution, 1:12 mL mg $^{-1}$ of Li-TFSI solution/spiro-MeOTAD) in chlorobenzene. To do so, each nanowire-based thin film is first covered with 50–70 μL of the spiro-MeOTAD solution before spin coating and left for 40 s before spin coating at 1200 rpm for 45 s in order to maximize pore filling. After spin coating, the counter electrode was applied by thermal evaporation of 100 nm of gold. J–V measurements of the cell were carried out under standardized AM1.5 illumination of 100 mW.cm $^{-2}$ (active area 0.18–0.19 cm 2 , spectral mismatch 2%).

Acknowledgements

There is a tremendous amount of people that have participated to my growth, enlarged my horizons and inspired me in the past years that I would like to thank.

Prof. M. Graetzel, thank you for allowing me to work with so much freedom in your lab and to be exposed to so many talented people attracted here by your worldwide reputation. It has been an honor to be part of your group and represent it outside of Switzerland. I will remember those years as the climax of my scientific enlightenment.

Prof. K. Sivula - ghetto chemist, cowboy scientist - your inspiring dedication to your work, your relentless efforts to push me, your hopes (sometimes a bit winded) to see me improve have directly led to the accomplishment of this thesis. Thank you Kevin for being a friend before being my boss. I cannot find words to express my gratitude for your constant support and attention. I owe you a lot!

I would have probably not survived without the help of Dr. Nicolas Tetreault, my partner in crime. Nic, on top of being like a big brother in the academic world, dragging me everywhere from Paris to Toronto, showing me that lab work can be just like a game, you have been and still are a loyal friend. Your straight-line tap in the back has been helping me to move forward. Thank you!

I was lucky enough to become friend with most members of the hydrogen group. First, Florian, thanks for having cleared the way on the complex and time consuming ground of the European Commission project's administration. But before that, I am grateful for all the time we have spent together as a tandem. Maurin, thanks for doing everything to facilitate the working condition for the entire team. I want to also mention your special efforts to deal with our differences in opinions and methods. We both learn out of this. I am sure we will keep track of each other together with Davi-dog, Tak-dog and Adriana.

Being a Phd student includes also a teaching duty. Mine has been a lot of fun thanks to Dr. Pierre Infelta under who's supervision we prepared the thermodynamics exercises together with Arianna (sorry for laughing so hard and teasing you a bit).

Many co-authors in the DSC group have been essential to the realization of the research projects I have been involved in: Jun-Ho, Peter C-Y, Daibin, Thomas, Zakeer but also coworkers: Paul, Pascal, Manuel and Robin. Outside of EPFL, successful collaborations have been initiated with research groups (Prof J. Augustynski at University of Warsaw in Poland and Prof M. McGehee at Stanford University in California) that have even sometimes hosted me (Prof. G. Ozin at University of Toronto in Canada and Prof. Leskela at University of Helsinki in Finland).

Nothing would be possible without the support from the technical staff: the magasin (Jacques and Marie) the electronic workshop (Gaby, Sujito, Harald, Gregoire) and associated (PAP) the mechanical workshop (Gil, André, Yves in particular), the team in the Material Science dept. (CIME), and the administrative staff at EPFL (Mme Gourdoux, U. Gonthier, Anne Lene Odegaard), at the energy center (Prof. H.B Püttgen, Massimiliano Capezzali, Dagmara) and for the European commission (Prof. G-J. Kroes, M. Van Der Haar).

My decisions to start a thesis is the result of people pushing me forward and helping me to acquire a vision. Dr. Kim Chi Huynh and my sister Jacinthe are the main ones. I would also like to thank Dr. F. Lenzmann and Dr. A. Laviano who basically put my foot on the ladder.

The daily life at the university includes numerous discussion and stories around lunches, coffee breaks, drinks, beach and ski sessions and trips. The main actors of this wonderful and necessary equilibrium between work and leisure have been in addition to those mentioned before Sophie W. (and Späzli), Nathalie B., Phil (Big Old' Beemer) and also Leo, Jelissa, Andrea, Ludmilla, Jan, Hauke, Etienne, Takeru, Joel, Hugues and many others. The persons sharing my life at home have been puffs of fresh air: Angèle, Nathalie S., Laurence nowadays but also Julien, Cuong, Elise, Sophie I., Ahlem, Fabienne, Christian, Anne Sophie, Lou'Jo and Max.

Last, I would like to express all my gratitude to my parents. Their diversity, independent mindset, freedom of thought and open mind offer broadener perspectives to whoever is in contact with them. Their unconditional love and care to their children has been leading my sisters and me for 36 years and keep on going. This make them my very first professors.

Curriculum Vitae

Jérémie Minh-Chau Brillet

Ecole Polytechnique Fédérale de Lausanne (EPFL)

Station 6, CH-1015 Lausanne, Switzerland

Jeremie.brillet@epfl.ch

Office Phone: +41 21 693-5178

Single
Born Aug. 11th, 1983
French (permis B)

Languages
Fluent: English, French
Basic: German, Mandarin

EDUCATION

- 2012** **Ph.D. in Material Science, Physical Chemistry**
EPFL, Laboratory of Photonics and Interfaces **Lausanne, Switzerland**
Thesis title: Solar energy stored as hydrogen: controlling inexpensive oxide-based nanostructures for efficient water splitting, under the co-supervision of Prof. Michael Graetzel and Prof. Kevin Sivula. Designed clever heteronanostructures for Dye-Sensitized-Solar-Cell/Hematite-photoanode tandem cell for solar water splitting into H₂.
Funding: European Commission's Marie Curie research training network.
Collaborations: Prof. McGehee (Stanford, USA), Prof. Ozin (University of Toronto, Ca), Prof. Leskela (University of Helsinki, Fi), Prof. Augustynski (University of Warsaw, Pl)
Grad. courses: Electronic Microscopy, Impedance spectroscopy, Introduction to nanomaterials, Entrepreneurial opportunity identification (Management of Technology Dept.), Management of Innovation and Technology Transfer (Technology Transfer and Industrial Relations Dept.)
Teaching: Thermodynamics (2nd year B.Sc), Fundamentals in Chemistry (1st year B.Sc)
- 2008** **M.Sc. Engineering, Material Science and Nanotechnology**
National Institute for Applied Sciences **Rennes, France**
Topics: Micro-opto electronics, clean room device processing, optronic technologies (TOP III-V), quantum physics, thermodynamics of materials, signal processing, wave propagation, biochips, management and communication
- 2008** **M.Sc. Physics and Interfaces**
Rennes I University **Rennes, France**
Topics: Radiation/matter interaction, symmetry and electronic properties, nanostructures, integrated optics and nanocaracterisation
- 2006** **Project Management Program**
LMU, College of Business Administration **Los Angeles, USA**
Topics: Risk Management, Quality Management, Planning, Performance Measurement, Negotiation, Control, Mission definition.
- 2002** **Baccalauréat (eq: A Level) in Science with distinction**
Institut Libre **Marcq en Baroeul, France**

MANAGEMENT & PROJECTS

- 2007** *Technology transfer*
Energy Centre of the Netherlands **Peten, Netherlands**
Perfected the anodic growth of Titania Nanotubes (based on publications of Prof. A.Grimmes, University of Pennsylvania, and Prof. P. Schmuki, University of Nuremberg-Erlangen). Transferred the technology from Energy Center of the Netherlands (ECN) to Ecole Polytechnique Fédérale de Lausanne.
- 2006** **Assistant to the CEO**
NANOWorld USA, Nanotechnology Center **Los Angeles, USA**
Researched and developed a global map and clustering of the nanotechnology industries: from government, university and private funding programs to final markets.
Designed and created a curriculum to educate non-nanotech engineers and executives in nanotechnology. This program was launched in October 2006 to top executives, senior engineers, material supply managers and innovation managers at Raytheon, Northrop Grumman and Toyota.
- 2006** **Project Leader**
National Institute for Applied Sciences, Nanotechnology Dept. **Rennes, France**
Coordination of a 5 persons team on the design of a control and acquisition system for a Scanning Tunnelling Microscope. Design and creation of a digital acquisition system for an accelerometer meant for airbag triggering.
- 2003-2006** *General Director*
Rock'n Solex Music Festival **Rennes, France**
Coordinated a team of over 50 volunteers to organize Public and private fund raising, programming of the festival, management of the technical staff, security assessment (15.000 visitors in 3 days), bilateral partnership, public relations and media of the festival. Operating budget: 350.000 euros.
- 2004-2005** **Member of the Board of Directors**
AEIR **Rennes, France**
Project leader for the reshuffle of the association's legal and operational framework to allow effective management of more than 30 major events, 5000 members and operating budget of 600 000 euros.

MUSIC

- *Transverse Flute*: End of study diploma at Conservatoire National de Musique (Nantes, Fr)
- *Musical Theory*: End of study diploma at Ecole de Musique (La Madeleine, Fr)
- *Trombone*: Student at School for Jazz and Contemporary Music - EJMA (Lausanne, CH)
- *Human Crux*: Groove/jazz band. Over 60 concerts across France.
- Self-educated in tenor saxophone, guitar, piano, bass and drums.

PEER REVIEWED PUBLICATIONS / PATENT

1. Brillet Jeremie, Yum Jun-ho, Cornuz Maurin, Hisatomi Takashi, Solarska Renata, Augustynski Jan, Graetzel Michael, and Sivula Kevin: Unassisted water-splitting using a low-cost dual-absorber tandem cell: a new benchmark for economical solar hydrogen production. *Nature Photonics*, **accepted**
2. Brillet Jeremie, Graetzel Michael, and Sivula Kevin: Decoupling Feature Size and Functionality in Solution-Processed, Porous Hematite Electrodes for Solar Water Splitting. *Nano Letters*, **2010** 10 (10), pp 4155–4160
3. Brillet, Jeremie; Cornuz, Maurin; Le Formal, Florian; Yum, Jun-Ho; Graetzel, Michael; Sivula, Kevin: Examining architectures of photoanode-photovoltaic tandem cells for solar water splitting: *Journal of Materials Research*, **2010** 25 (1), pp 17-24
4. Alvaro Valdes, Jeremie Brillet, Michael Gratzel et al. Solar hydrogen production with semiconductor metal oxides: new directions in experiment and theory *Phys. Chem. Chem. Phys.*, **2012**, 14, 49–70.
5. Sivula Kevin; Brillet Jeremie and Graetzel Michael. Controlling photo-activity of solution-processed hematite electrodes for solar water splitting. 2010 Solar Hydrogen and Nanotechnology V *Proceedings of SPIE* 7770
6. Peter Chen, J r mie Brillet, Hari Bala, Peng Wang, Shaik M. Zakeeruddin and Michael Gr tzel: Efficient Solid-state dye-sensitized solar cells using TiO₂ nanotube arrays on FTO glass *Journal of Material Chemistry*, **2009**, 19, 5325
7. Daibin Kuang, J r mie Brillet, Peter Chen, Masakazu Takata, Satoshi Uchida, Hidetoshi Miura, Kohichi Sumioka, Shaik. M. Zakeeruddin and Michael Graetzel. Application of Highly Ordered TiO₂ Nanotube Arrays in Flexible Dye-Sensitized Solar Cells, *ACS Nano*, **2008**, 2 (6), pp 1113–1116
8. Takashi Hisatomi , J r mie Brillet, Maurin Cornuz , Florian Le Formal , Nicolas T treault , Kevin Sivula and Michael Gr tzel. A Ga₂O₃ underlayer as an isomorphic template for ultrathin hematite films toward efficient photoelectrochemical water splitting. *Faraday Discuss.*, **2012**, 155, 223–232
9. Ding I-Kang, Tetreault Nicolas, Brillet Jeremie, Hardin Brian E., Smith Eva H., Rosenthal Samuel J., Sauvage Frederic, Graetzel Michael, and McGehee Michael: Pore-Filling of Spiro-OMeTAD in Solid-State Dye Sensitized Solar Cells: Quantification, Mechanism, and Consequences for Device Performance. *Advanced Functional Materials*, **2009** 19 (15), pp 2431-2436
10. Sivula Kevin; Le Formal Florian; Brillet Jeremie and Graetzel Michael: New nanostructures enhance solar water splitting with hematite *SPIE newsroom* **2010**
11. Takashi Hisatomi, Florian Le Formal, Maurin Cornuz, J r mie Brillet, Nicolas T treault, Kevin Sivula and Michael Gr tzel. Cathodic shift in onset potential of solar oxygen evolution on hematite by 13-group oxide overlayers. *Energy Environ. Sci.*, **2011**, 4, 2512-2515
12. Nicolas Tetreault, Endre Horvath, Thomas Moehl, Jeremie Brillet, Rita Smajda, Stephane Bungener, Ning Cai, Peng Wang, Shaik M. Zakeeruddin, Laszlo Forro, Arnaud Magrez, and Michael Graetzel. High- Efficiency Solid-State Dye- Sensitized Solar Cells: Fast Charge Extraction through Self-Assembled 3D Fibrous Network of Crystalline TiO₂ Nanowires. 2010, 4, 12, 7644–7650
13. Nicolas Tetreault, Eric Arsenault, Leo-Philipp Heiniger, Navid Soheilnia, Jeremie Brillet, Thomas Moehl, Shaik Zakeeruddin, Geoffrey A. Ozin, and Michael Graetzel. Solar hydrogen production with semiconductor metal oxides: new directions in experiment and theory, *Phys. Chem. Chem. Phys.*, **2012**, 14, 49–70
14. Nicolas Tetreault, Jeremie Brillet, Geoffrey A. Ozin, and Michael Graetzel. Electrode e.g. photoanode, for electrochemical device e.g. regenerative dye sensitized solar cell, has three-dimensional porous conductive matrix provided on conductive substrate, where coating partially or totally covers surface of matrix. **Patent Number:** WO2011125024-A1, **2010**

CONFERENCES / PRESENTATIONS

1. *Material Research Society Spring Meeting*, apr. 2012,
San Francisco, California (Oral presentation)
2. *European Commission Research Training Network Hydrogen Conference*, nov. 2010
Noordwijkerhout, Netherlands (Oral presentation)
3. *Material Research Society Spring Meeting*, Apr. 2010,
San Francisco, California (Poster presentation)
4. *European Commission Research Training Network Hydrogen Conference*, oct. 2010
Warsaw, Poland (Oral presentation)
5. *EMPA Workshop on transparent conducting electrodes for photovoltaics*, jan. 2010
Bern, Switzerland (Poster presentation)
6. *Intl. Conference on the Industrialization of the Dye Solar Cell (3rd DSC-IC)*, apr. 2009
Nara, Japan (Poster presentation)
7. *European Commission Research Training Network Hydrogen Conference*, sept. 2008
Reykjavik, Iceland (Oral presentation)
8. *European Science Foundation, Nanotechnology for Sustainable Energy*, june 2008
Obergurgl, Austria (Poster presentation)
9. *Intl. Conference on the Industrialization of the Dye Solar Cell (2nd DSC-IC)*, sept. 2007
St Gallen, Switzerland

REFERENCES

Prof. Dr. Michael GRAETZEL,

Director of the Laboratory for Photonics and Interfaces

Station 6, CH-1015 Lausanne,
Switzerland

michael.graetzel@epfl.ch

+41 (0) 21 693 3112

Dr. Jacky EVEN,

Director of the Material Science Department at the National Institute of Applied Sciences

20, av. De Buttes de Couësmes,
35043 Rennes, France

jacky.even@insa-rennes.fr

+33 (0) 2 23 23 82 95

Prof. Dr. Kevin SIVULA

Director of the Laboratory for Molecular Engineering of Optoelectronic Materials

Station 6, CH-1015 Lausanne,
Switzerland

kevin.sivula@epfl.ch

+41 (0) 21 693 7979

Dr. Anthony F. LAVIANO,

Chairman and Founder of NANOWorld

16651 Linda Terrace, Pacific Palisades,
CA 90272, USA

a.f.laviano@nanoworldusa.com

+1 (310) 459-8569